Evolution of Glaciar Pío XI, a calving glacier in the Southern Patagonia Icefield, under the influence of non-climatic forcing

(南パタゴニア氷原 Pío XI 氷河における
気候以外の要素に影響を受けた末端位置・表面標高・流動変化)

Shuntaro Hata

Ph.D. Dissertation

Graduate School of Environmental Science,
Division of Earth System Science,
Course in Cryosphere Science,
Hokkaido University

August 2022

Abstract

This thesis studies changes of calving glacier under a infuluence of non-climatic forcings. To investigate the long-/short term changes of Glaciar Pío XI, I measured ice-front position, surface elevation, and ice velocity during a period of 2000–2021 by utilizing satellite remote sensing techniques. The focus of the study was relationships between galcier variation and sediment deposition infront of the glacier terminus and lake level drop event, which both were identified by this study.

Most of the ice-fronts showed advancing trends over the study period. The greatest advance (1,400 m from 2000 to 2018) was observed at the southern terminus. The northern terminus and some of the subsidiary ice-fronts advanced by several hundred meters during the same period. Glacier-surface elevation increased at a rate increasing from 1.14 ± 0.03 m a^{-1} in 2000–2007 to 2.69 ± 0.04 m a^{-1} in 2007–2017/18. If we assume this elevation change is totally due to ice thickness change, the mass gain is equivalent to 4% of the mass loss in the SPI from 2000 to 2015/16. Our data demonstrated that Glaciar Pío XI is one of the most rapidly thickening glaciers in the world. Satellite images indicated sediment deposition and formation of a mound in front of the southern terminus, the mound covered ~80% of the width of the ice-front in October 2018.

Satellite data showed rapid drainage of the lake from April to July 2020, resulting in decrease in the lake area by 14.5 ± 0.02 km^2 and drop in the water level by 18.3 ± 1.2 m. Water volume released from the lake was 3.7 ± 0.2 km^3 (3.7 ± 0.2 Gt), which is one of the greatest among ever reported glacial lake outburst events. Satellite images and DEMs indicated that the outburst was triggered by the collapse of a bump near the lake outlet and subsequent change in the flow path of the outlet stream. The event affected the gravity field, which was observable by the GRACE mascon solution. After the drainage event, characteristics changes are observed at the northern terminus of Glaciar Pío XI. First, the terminus showed rapid retreat (−300 m) and thinning after the drainage event. Glacier velocity of the northern terminus dropped by 60% after the drainage event within 2weeks

since the onset, subsequent slow-down was resulted in 92% reduction in the velocity than the velocity before the drainage event. Further, the seasonal change in velocity of the terminus observed before the event was not confirmed form the timeseries of the velocity. Furthermore, the spatial distribution of glacier indicated changes in the primary flow direction from towards the northern terminus to towards the southern terminus.

This study revelaed i) recent changes in ice-front position, surface elevaiton, and ice speed of Glaciar Pío XI, ii) sediment deposition in front of a glacier terminus have strong influece to the variation of the glacier, and iii) change in lake level have a strong influence to changes in ice-front position, surface elevation, and ice velocity. Thus, results of this study present a case study which variation of a calving glacier is strongly affected non-climatic forcing, and emphasize that non-climatic forcings shoud be considered for the future projection of calving glaicer.

Table of contents

List of figures

List of tables

Chapter 1
General introduction

1.1 Calving glaciers

As a consequence of warming climate, glaciers and ice sheets are losing ice mass. The loss of ice is contributing to the recent global sea level rise. Global total ice volume change of mountain glaciers is estimated to be $158 \pm 41 \times 10^3$ km^3, which is equivalent to 0.32 ± 0.08 m sea level and only 0.1% of ice mass on the Earth (Farinotti et al., 2019). The mountain glaciers account for only 0.5% because of the large fraction of the Greenland and the Antarctic ice sheets. The masses of these two ice sheets are 7.42 ± 0.05 m s.l.e. (sea level equivalent) (11.3%, Morlighem et al., 2017) and 57.9 ± 0.9 m s.l.e. (88.2%, Morlighem et al., 2020), respectively. Despite the relatively small ice mass, recent contribution of mountain glaciers to sea level rise is large. Mass loss of glaciers accounts for 27 ± 22 mm of global mean sea level rise in 1961–2016, which account for 25–30% of the observed sea level change (Zemp et al., 2019, Figure 1.1). Recently, the global glacier volume change was observed by satellite (Hugonnet et al., 2021). This observation showed that the contribution was 21 ± 3% of sea level rise observed from 1993 to 2017, which is larger than that of the Greenland and the Antarctic ice sheets, respectively.

Glacier mass loss is nonuniformly distributed over the globe (Figure 1.1). The largest mass loss was observed in Alaska (-73 ± 17 Gt yr^{-1}), whereas the most rapid mass loss rate was observed in Southern Andes (-1.18 ± 0.38 m w.e. yr^{-1}) during a period of 1961–2016, respectively (Zemp et al., 2019). In these regions where rapid mass loss is reported, large fractions of glaciers are terminating into the ocean or lakes. These glaciers terminating in water is called calving glacier. Indeed, calving glaciers in Alaska and Southern Andes occupy 33% and 58% of the total glacier area, respectively (RGI Consortium, 2017).

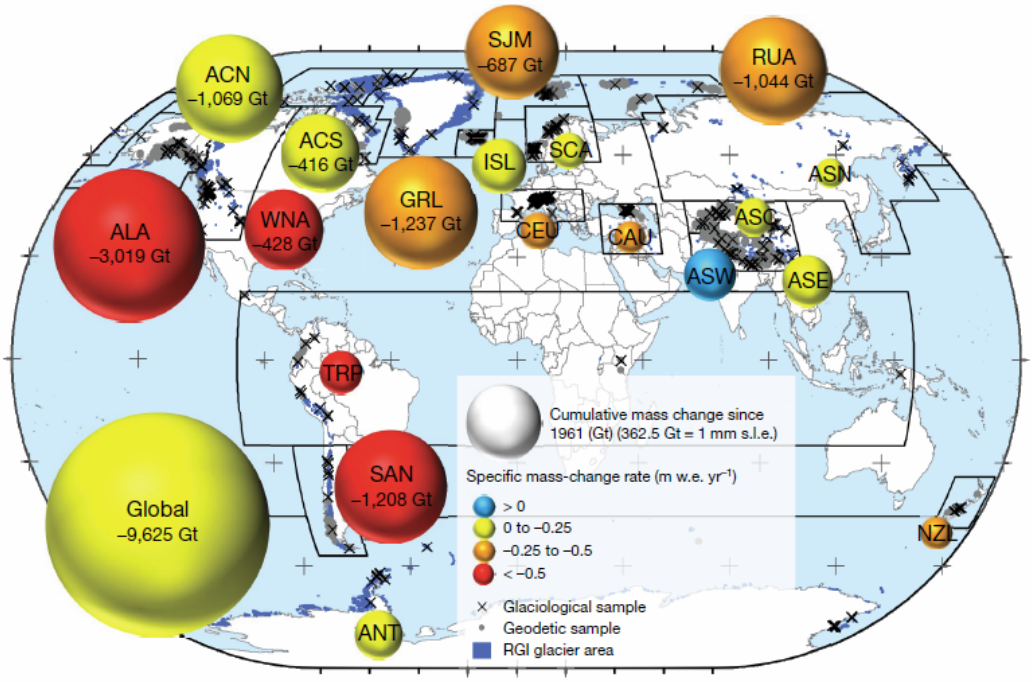

Figure 1.1. Regional glacier mass loss from 1961–2016 (Zemp et al., 2019). Size and color of each sphere represents the change in volume and its specific rate, respectively.

1.2. Evolution of calving glaciers

The mass change of glaciers terminating on land is dominated by the processes on glacier surface, integral of specific accumulation rate and ablation rate determines glacier mass change. On the other hand, calving glaciers lose ice at the glacier terminus by calving and subaqueous melting. These processes are collectively called as frontal ablation. Frontal ablation is a unique process occurring only at calving glaciers. The mass change of a calving glacier $\frac{dM}{dt}$ can be described as

$$\frac{dM}{dt} = C - A + \dot{B}_e + \dot{B}_b - A_f \tag{1.1}$$

where C, A, $\dot{B}_e$, B_b, A_f are accumulation, surface ablation, englacial mass balance, basal mass balance, and frontal ablation, respectively (Cuffey and Paterson, 2010; Figure 1.2). In general, englacial and subglacial mass balance are negligible. Here, frontal ablation can be expressed as

$$A_f = A_t \left(u_m - \frac{dL}{dt} \right) \tag{1.2}$$

where A_t, u_m and $\frac{dL}{dt}$ are cross-sectional area of the terminus, mean glacier velocity at the terminus and mean change rate of glacier length, respectively (Cuffey and Paterson, 2010; McNabb et al., 2015; Minowa et al., 2017; Dryak and Enderlin, 2020). In general, the ice flow velocity of terminus region of calving glaciers is larger than that of land-terminating glaciers due to the effect of proglacial water. Moreover, the glacier velocity shows large variations in seasonal to decadal temporal scales (e.g., McFadden et al., 2011; How et al., 2017; Joughin et al., 2018; King et al., 2018). Therefore, evolution of calving glaciers is affected by not only climatic conditions but also the conditions of the ocean or lake, and glacier flow regime.

Recent years, challenging observations were performed to quantify frontal ablation. Calving flux was estimated at Himalayan glaciers by combination of unmanned aerial vehicle photography obtained in the field and high-/medium-resolution satellite

images (Watson et al., 2020). Combination of measurement of surface wave generated by calving and time-lapse photography was used to quantify calving at Glaciar Perito Moreno in Patagonia (Minowa et al., 2018, 2019a). Seismic, hydro-acoustic, time-lapse photography, and lidar data were utilized to estimate calving volume at Kronebreen in Svalbard (Köhler et al., 2019). Frontal ablation of an ocean-terminating glacier was measured by repeated multi-beam sonar surveys (Fried et al., 2015; Sutherland et al., 2019). Nevertheless, field observation at terminus of calving glaciers is still challenging. Because glacier velocity and length change can be measured by using satellite images, frontal ablation could be obtained as a residual term. Note that the calculated frontal ablation cannot be separate to calving and subaqueous melting.

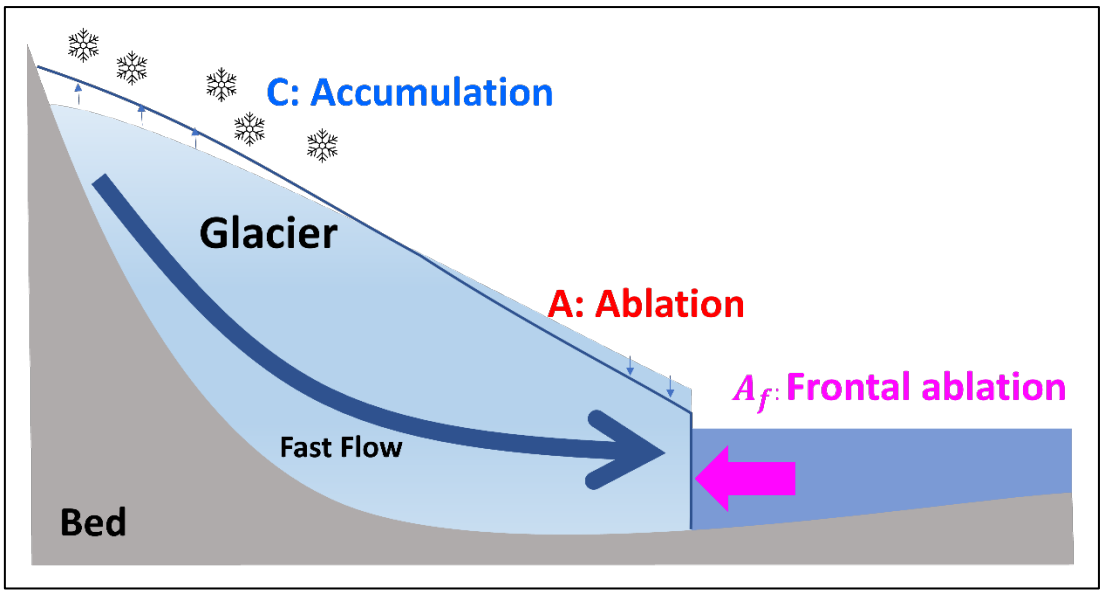

Figure 1.2. Schematic illustration of controlling factor of mass change at a calving glacier.

1.3. Complex variations of calving glaciers

The evolution of a calving glacier is complex because processes affecting the mass balance and flow regime are largely affected by non-climatic factors as well as climate. Rapid retreat of a calving glacier is not explained only by increase in surface melt due to rising of air temperature, but often influenced by the change in the ice dynamics. Thinning, thinning induced steepening, mélange opening, near-floating condition, and the combinations of these factors may induce glacier acceleration, which lead longitudinal stretching and subsequent thinning. This mechanism is called as “dynamic thinning”, which is regarded as a significant process deriving subsequent rapid retreat of the glacier (e.g., Thomas et al., 2003). Retreat of Columbia Glacier in Alaska initiated in early 1980s and continued until recently. This approximately 30-year-long retreat by ~20 km resulted in a 140 Gt of ice loss (e.g., Meier and Post, 1987; McNabb and Hock, 2014; Enderlin et al., 2018, Figure 1.3). During the long retreat history, terminus position was stable when the ice-front was located at constriction (McNabb and Hock, 2014; Enderlin et al., 2018), which implies topographic settings have important role for glacier ice-front position. Although glacier retreat is a general trend in Alaska, one third of the calving glaciers in the region advanced in 1948–2012 (McNabb and Hock, 2014). For example, Taku Glacier in Alaska had advanced by 7 km since 1890 (Nolan et al., 1995; Motyka and Echelmeyer, 2003; Kruiger et al., 2006). From previous studies on the advance of Taku Glacier, sediment deposition in front of the glacier terminus has been regarded as the most important process for the glacier stabilization (Motyka and Béget, 1996; Kruiger et al., 2006; Truffer ett al., 2009). Since the formation of the sediment deposition in front of the glacier, details of proglacial sedimentation (e.g., deformation, transportation, location of outwash channel) are observed by field survey (Kruiger et al., 2006; Zechmann et al., 2020). Nevertheless, detailed observation during the period of sediment mound formation is lacking in Taku Glacier.

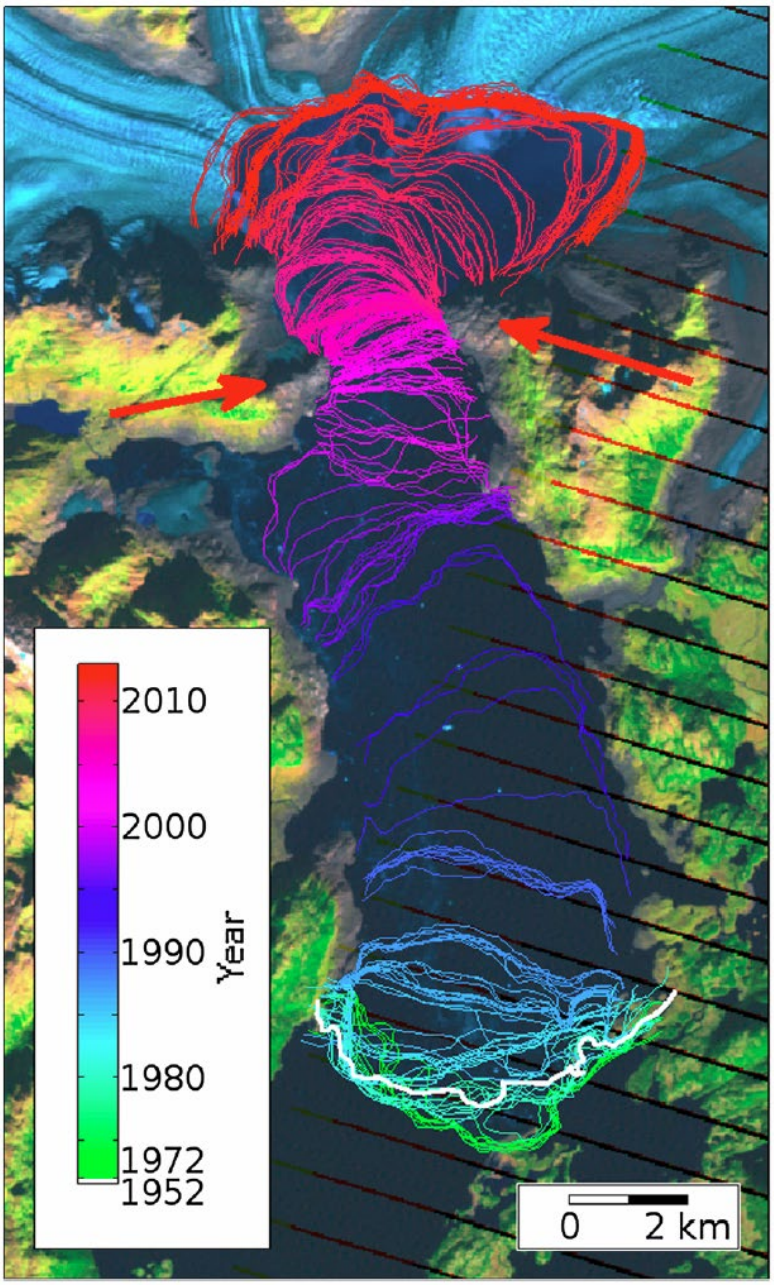

Figure 1.3. Ice-front position change of Columbia Glacier since 1952 (McNabb and Hock, 2014). Each curve represents the ice-front position of the glacier and the color represents the observed time.

Tidewater glacier cycle is proposed to explain the cyclic behavior with rapid retreat and slow advance, based on the observation of the evolution of Alaskan tidewater glaciers (e.g., Post, 1975; Amundson, 2016, Figure 1.4). Brinkerhoff et al. (2017) performed numerical modelling to investigate the cyclic evolution of an ocean terminating glacier by taking into account glacier flow, sediment erosion and transport and an interaction between sediment deposition and ice speed. Their results emphasized the significance of the basal topography for rapid retreat and sediment transport for stabilizing ice-front. Therefore, the cyclic behavior of calving glaciers is thought to be independent from the climate conditions.

Ocean terminating glaciers are affected by changes in ocean conditions as well. Among ocean-terminating outlet glaciers of Greenland Ice Sheet, glaciers terminating in a deep fjord showed larger retreat than glaciers in shallow fjords, suggesting the effect from oceanic heat contained in deeper water in the fjords (Wood et al., 2018; 2021). Furthermore, buoyant plume of subglacial discharge, entrains warm deep ocean water, and provide heat for melting to the glacier front. Such scheme of underwater melting causes melt undercutting of the glacier front (Rignot et al., 2015; Fried et al., 2015). The ice cliff is destabilized and thus calving is induced (Slater et al., 2017; Vallot et al., 2018). Jakobshavn Isbræ, one of the largest outlet glaciers of the Greenland ice sheet, had showed a 20-year-long retreat, thinning, and speed up in the recent two decades (Motyka et al., 2011; Joughin et al., 2008). However, the glacier terminus showed advance, thickening, and slow down since 2016. These changes were attributed to a cooling of the fjord water (Khazendar et al., 2019). The ocean effect is not limited to thermal condition. Tide modulates glacier motion, i.e., glacier speed acceleration was observed near the front during low tide periods (Podrasky et al., 2014; Sugiyama et al., 2015; Podolskiy et al., 2016). Furthermore, fast crevasse opening was observed at low tide period, suggesting leading calving (van Dongen et al., 2019).

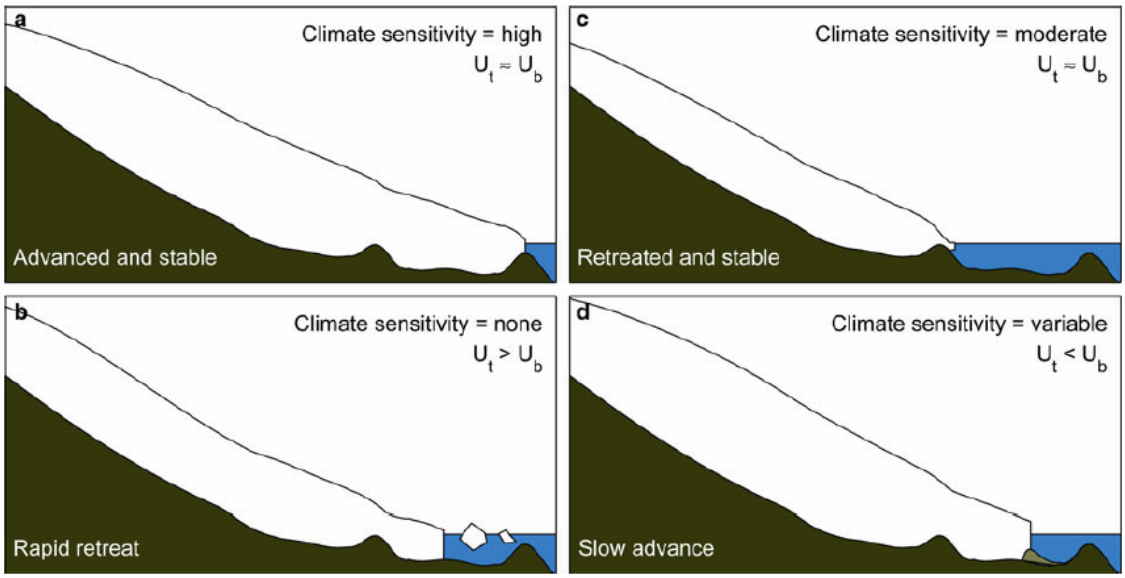

Figure 1.4. Schematic illustration showing tidewater glacier cycle (Amundson, 2016). Each panel represents a tidewater glacier in (a) stable phase after advancing, (b) stable phase after rapid retreated, (c) rapid retreating phase with large calving flux, and (d) slow advancing phase with sediment deposition, respectively. U_s and U_t are balance velocity and velocity at the terminus, respectively.

1.4. Advance of Glaciar Pío XI

Glaciar Pío XI situated in the Southern Patagonia Icefield is another example of advancing calving glacier. This glacier is well known its long-lasting advancing trend since 1945 (Figure 1.5). Glaciar Pío XI advanced by more than 10 km between 1945 and 1962 (Rivera, 1992). During this period, the glacier terminus reached the western frank of Eyre Fjord and bifurcated into two ice tongues, one flowing south into Eyre Fjord and the other to the north into Lago Greve. Both termini showed advancing trends until 1998, except for a retreat of the southern terminus from 1981 to 1985 (Rivera et al., 1997a). Thereafter, the southern and northern termini showed relatively short episodes of retreat during 1998–2000 and 1998–2005, respectively (Sakakibara and Sugiyama, 2014; Wilson et al., 2016). Several mechanisms have been proposed for the advance of Glaciar Pío XI in the 20th century.

i. Response to an increased snow fall (Rivera et al., 1997a)
ii. Shoal formed by sediment deposition in front of the glacier provided stability to the ice-front and reduced frontal ablation (Warren et al., 1997)
iii. Result of glacier surge activities (Rivera et al., 1997b)

No consensus has been reached so far. Most likely multiple mechanisms are involved in the 20th century advance of Glaciar Pío XI.

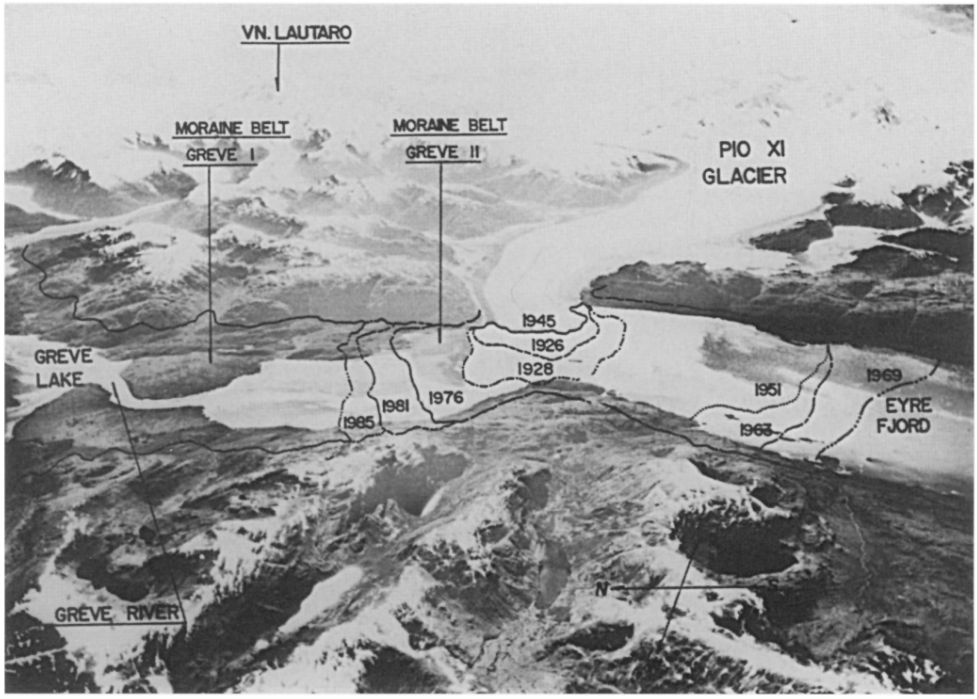

Figure 1.5. Oblique aerial photograph taken in 1945 (Rivera et al., 1997a).

After short periods of retreat in 1998–2000 and 1998–2005, the southern and northern termini began to advance in 2000 and 2006, respectively (Sakakibara and Sugiyama, 2014; Wilson et al., 2016; Rivera, 2018). Wilson et al. (2016) performed detailed investigation on the flow speed variations of Glaciar Pío XI together with analyses of the ice-front position and changes in ice thickness. After a period of large acceleration up to 2000, the ice speed of the glacier progressively decreased in the 21st century. The authors of the study classified Glaciar Pío XI as a surge-type glacier and interpreted the recent advancing trend as the response to the fast ice-flow condition lasted until 2000. Glacier surge causes mass transport from the accumulation area to the terminus regions, which often results in ice thickening near the glacier front while thinning in the upper reaches. However, recent studies based on satellite and field surveys have shown a thickening trend over the entirety of Glaciar Pío XI (Foresta et al., 2018; Malz et al., 2018; Abdel Jaber et al., 2019; Minowa et al., 2019b). To better understand of the recent advance, further analysis is required particularly for the surface elevation change of the glacier.

1.5. Glacial lakes and GLOF

As a consequence of glacier retreat under warming climate, the number, area, and volume of glacial lakes have increased in recent decades (Shugar et al., 2020, Figure 1.6). In particular, rapid increase has been observed in Patagonia (Wilson et al., 2018), Alaska (Field et al., 2021), Himalaya (Zhang et al., 2015), and Greenland (Mallalieu et al., 2021). Glacial lakes affect ice dynamics, frontal ablation, and hence the evolution of glaciers terminating in the lakes (Truffer and Motyka, 2016; Tsutaki et al., 2019; Sugiyama et al., 2019; Carrivick et al., 2020). Because of the influences of lakes, freshwater calving glaciers currently experience more rapid retreat and greater mass-loss than glaciers terminating on land (King et al., 2019). In Patagonia, freshwater calving glaciers are rapidly retreating and thinning (Sakakibara and Sugiyama, 2014; Dussaillant et al., 2018; Malz et al., 2018; Abdel Jaber et al., 2019; Minowa et al., 2021), which causes rapid mass loss of the Southern and Northern Patagonia Icefields (Zemp et al., 2019). As a result of the glacier retreat, glacial lakes in the regions are expanding at the greatest rate in the world (Shugar et al., 2020). Glacial lakes are forming in front of retreating glaciers all over the world, thus, the importance of the study on the influence of glacial lakes to lake-terminating glaciers is increasing. However, most of the studies on calving glaciers have been performed at ocean-terminating calving glacier so far, studies as a target of lake-terminating calving glaciers are not enough to be performed.

Glaciers affect lake environments via sedimentation and water circulation (Sugiyama et al., 2016, 2021), which play critical roles in the ecosystems of the lakes (Carrivick et al., 2013). Freshwater calving is important for the ecosystem also via nutrient-rich meltwater discharge controls the biochemical condition of the lake (Sommaruga, 2015; Tubertu et al., 2020). Further, glacial lake outburst flood (GLOF) has a strong impact on physical and biological environments downstream (Meerhoff et al. 2019). For example, large-scale GLOFs during the deglaciation of past ice sheets affected ocean current and hence regional climate by discharging a large amount of freshwater

into the ocean (Glasser et al., 2016). Monitoring glacial lakes is thus important for understanding future changes of freshwater calving glaciers and the surrounding environment.

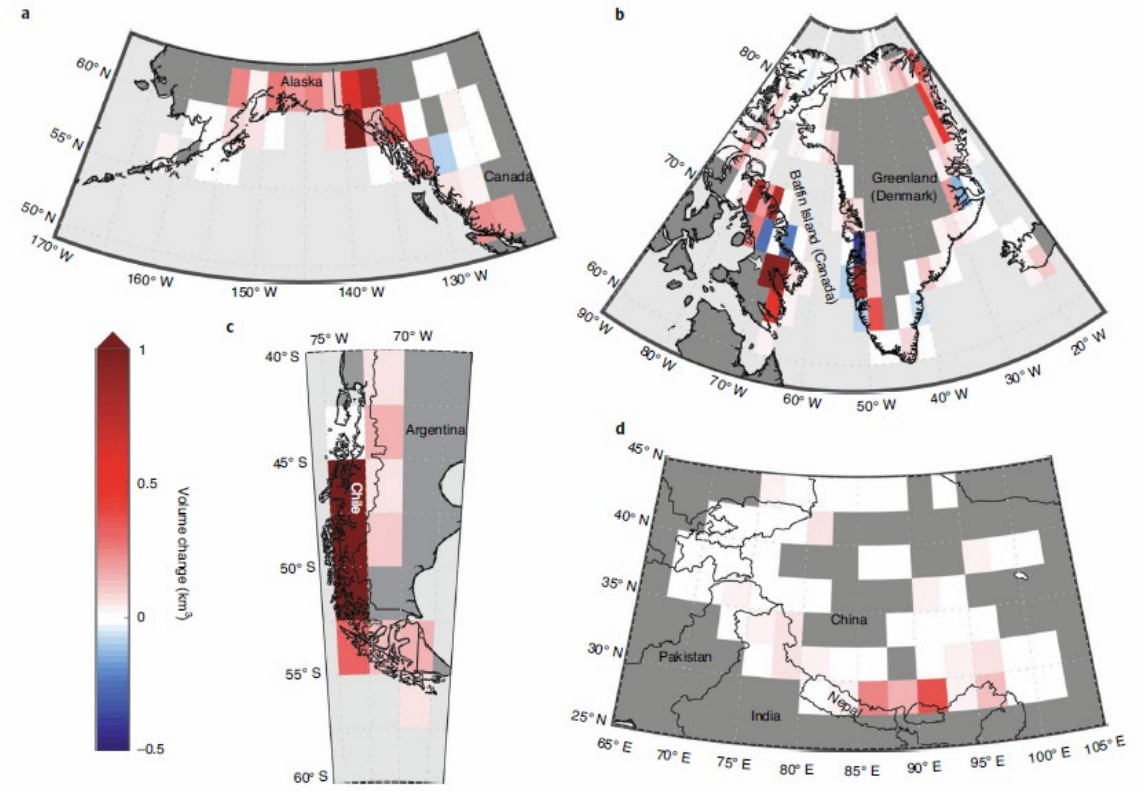

Figure 1.6. Regional volume change of glacial lake in 1990–2018 (Shugar et al., 2020). Spatial distribution of volume change of glacial lakes within each 2.5°-grid in (a) Alaska, (b) Greenland, (c) Patagonia, and (d) High Mountain Asia.

GLOF occurs when a moraine-, glacier-, or bedrock-dam is breached. Tsunami and seiche waves generated by e.g., calving, landslide, or rockfall trigger outburst by initiating lakewater overflow and subsequent erosion of the dam (Neupene et al., 2019; Hubbard et al., 2005). Seepage of lakewater through a moraine dam and uplift of an ice dam due to flotation are other mechanisms that trigger lake outburst (Westby et al., 2014; Sugiyama et al., 2008). GLOF also occurs when a moraine dam spontaneously collapses after deglaciation, a process so called “self-destruction” of a dam (Emmer and Cochachin,

2013). Sudden release of a large amount of water has the potential to cause serious damage to communities and infrastructure downstream (Veh et al., 2020). Several thousand deaths due to GLOFs have been reported during the last hundred years (Carrivick and Tweed, 2016). The actual number of fatalities is most likely greater because the inventory of lake outburst is incomplete (Emmer et al., 2022). Under the influence of formation and expansion of glacial lakes (Shugar et al., 2020; Wilson et al., 2018; Field et al., 2021; Zhang et al., 2015; Mallalieu et al., 2021), the frequency of GLOFs possibly increases in the 21st century (Harrison et al., 2018). Therefore, further understanding of outburst mechanism and long-term monitoring of glacial lakes are required to manage hazards in mountainous regions.

The sudden drop in the lake level should have impacts on the glaciers terminating in the lake. Previous studies on ice marginal lakes reported significant impacts of outburst floods on glacier dynamics (Sugiyama et al., 2008; Bigelow et al., 2020). Nevertheless, observation of outburst of a proglacial lake is sparse, thus its impact on the calving front is poorly understood. Considering the tidal influence on the ice speed of marine-terminating glaciers (e.g., Podolskiy et al., 2016), speed change of a lake-terminating glacier is expected after a GLOF. Further, the drop in the lake level should affect the frequency and magnitude of calving, as well as underwater ice front melting. Therefore, studying glaciers after GLOFs is a unique opportunity to investigate the dynamics and frontal ablation of freshwater calving glaciers. Despite the importance of the impact to downstream and around the lake environment, studies on large-scale GLOFs and its influence on glacier dynamics are scarce because large-scale GLOFs occur infrequently.

1.6. Objectives of the thesis

In this thesis, I investigate the complex behavior of calving glacier, based on the observation of recent changes of Glaciar Pío XI, an advancing calving glacier in Patagonia. The objective of this study is to quantify long-term and short-term evolution of Glaciar Pío XI affected by non-climatic forcings. Observed changes of Glaciar Pío XI are analyzed together with characteristic environmental changes observed near the termini, i.e., sediment deposition and a GLOF. In order to achieve these objectives, this study investigates

i) recent changes in the ice-front position and surface elevation of Glaciar Pío XI
ii) details of the drainage event of Lago Greve in 2020, and changes in glacier evolution affected by the drainage event.

In Part 1, changes in ice-front position and surface elevation of ablation area of Glaciar Pío XI were quantified by analyzing satellite images and DEMs, from 2000–2018. The results are discussed with visual inspections of satellite image indicating the emergence of sedimentary mound in front of the southern terminus. Based on the results, mechanism of the recent advance of Glaciar Pío XI is discussed.

In Part 2, satellite data analyses were performed at Lago Greve and the northern terminus of Glaciar Pío XI. Timing of the onset and magnitude of an abrupt drainage event of Lago Greve was determined by observing changes in area, water level, and volume of the lake. Changes in ice-front position, surface elevation, and glacier velocity were quantified by analyzing satellite images and DEMs, from 2016–2021, to investigate the influence of the drop of lake level.

By using these results, I investigated the role of non-climatic forcing in the long-/short-term evolution of calving glacier.

Chapter 2
Study site

2.1. The Southern Patagonia Icefield

The Southern Patagonia Icefield (SPI) (Figure 2.1) is a large ice mass located along the border between Chile and Argentina, covering an area of 12231 km^2 (Meier et al., 2018) and being the second largest ice mass of the Southern Hemisphere. The total ice volume of the SPI was estimated to be 3632 ± 675 km^3 (Millan et al., 2019), which is about 10 mm sea level equivalent. In the SPI, weather conditions show contrasts between the western side and the eastern side because of the westerly wind. The Andes mountain range and the westerly winds cause the western-eastern gradient in precipitation; heavy precipitation in the western side (>10 m w.e. a^{-1}) and a dryer condition in the eastern side (<1 m w.e. a^{-1}) (Lenaerts et al., 2014). Several ice cores have been drilled from the SPI, from which net accumulations were reconstructed. An Ice core drilled in the accumulation area of Glaciar Tyndall was analyzed for snow accumulation, which suggested net accumulation of 17.8 m w.e. a^{-1} in 1997/98–1998/99 and >11.0 m w.e. a^{-1} in 1998/99–1999/2000 (Shiraiwa et al., 2002). Another ice core drilled in the accumulation area of Glaciar Pío XI indicated net accumulation of 5.8 m w.e. a^{-1} as a mean over 2001–2005 t (Schwikowski et al., 2013). These mounts of accumulation enable the outlet glaciers reach to the ocean or lakes at lower elevation.

In the SPI, 83% of the major outlet glaciers terminate in water (Davies and Glasser, 2012), mostly in fjords on the western side of the icefield and in lakes on the eastern side. Most of these glaciers are currently retreating and thinning (Aniya et al., 1997; Rignot et al., 2003; Sakakibara and Sugiyama, 2014; Foresta et al., 2018; Malz et al., 2018; Abdel Jaber et al., 2019; Braun et al., 2019; Dussaillant et al., 2019). Retreat and thinning of calving glaciers dominate recent mass loss of the icefield, which, among

mountain glaciers in the world, is the second largest contributor to sea level rise after Alaskan glaciers (IPCC, 2019). On the other hands, the glacialized area in Patagonia is relatively small than Alaska, which makes the Patagonian glaciers to the most rapid mass loss rate in the world since 1960s (Zemp et al., 2019).

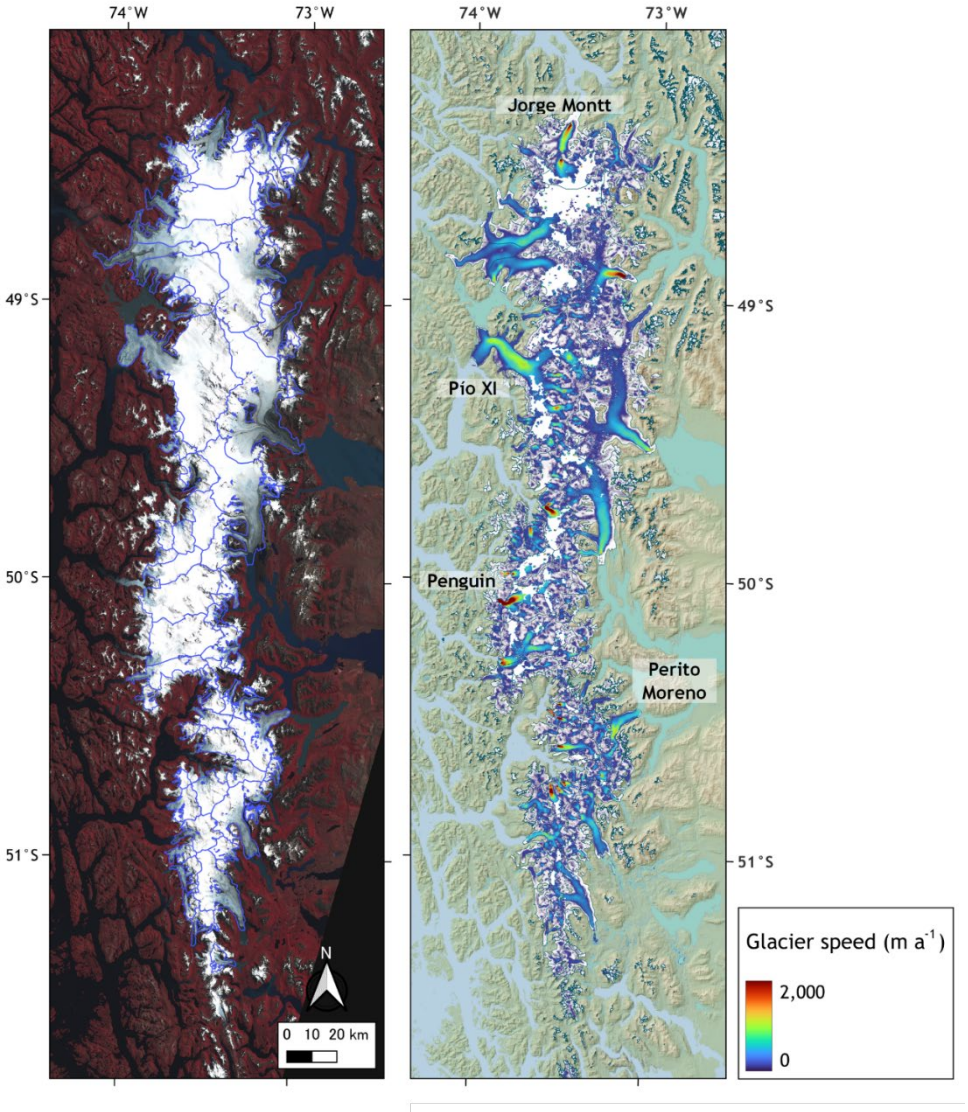

Figure 2.1. Overview of the SPI. (left) The image was taken on 20 January 2022 by Sentinel-2 MSI. Blue curves represent glacier boundary in 2000-2003 (RGI Consortium, 2017). (right) Annual mean glacier surface speed in 2019 by RETREAT project (Friedl et al., 2021).

Most of the calving glaciers in the SPI have been retreating and thinning since 1980s (Sakakibara and Sugiyama, 2014; Malz et al., 2018; Foresta et al., 2018). Some of the glaciers show extraordinarily rapid retreat. For example, Glaciar Jorge Montt retreated ~15 km from 1975–2018, under the influence of dynamic thinning near the terminus (Bown et al., 2019). These speed-ups accelerate ice discharge of the SPI, which is consisted rapid flowing calving glaciers. For example, velocity of Glaciar Penguin showed 12000 m a^{-1}, which make it one of the most rapid glaciers in the world (Millan et al., 2022). On the other hands, not all glaciers show rapid retreat. Glaciar Pío XI had advanced > 10 km since 1945 (e.g., Wilson et al., 2016), Glaciar Perito Moreno had been kept stable ice-front position since 1920 (e.g., Minowa et al., 2015)

Field campaign on the western side of the SPI is difficult. Complex fjord systems are distributed in the western side of the SPI (Figure 2.1). Puerto Eden (49.1°S, 74.2°W), the only town located on the western side of the SPI and the last waypoint to western side of the SPI, is separated, even as one-line distances, ~150 km to Caleta Tortel and >300 km to Puerto Natales, the next towns respectively. To carry out field observation on the western side of the SPI, long way moving on cruise are needed. Otherwise, chartering helicopter or crossing the SPI from eastern side are needed. As well as logistically difficulties, harsh climate makes the field campaign there difficult. Therefore, field campaign on the western side of the SPI is not much performed. On the other hands, much more field campaigns on the eastern side of the SPI had been performed so far because of logistically easiness and relatively calm climate conditions.

Due to the difficulties of access to glaciers, significant measurement data are limited especially in the western side of the SPI. Although precipitation was measured at Puerto Eden in 1997–2011 with interruption in 2006–2007, other factors (i.e., air temperature and wind speed) were not measured. Although Dirección General de Aguas (DGA) installed several weather stations on/around the SPI and other glacialized areas in Chile recent years, public data are only limited datasets yet. In addition, measurement of

surface mass balance on the western side is not reported so far. Millan et al. (2019) reported spatial distribution of ice thickness over the SPI estimated by using 3-D inversion technique from airborne gravimetry with constraint of ice thickness measurement by using radar on aircraft/helicopter, and fjord/lake bathymetry. However, the data coverage was not complete over the SPI, and the lacking is concentrated on the ablation area of the western side of the SPI (Millan et al., 2019).

2.2. Glaciar Pío XI

Glaciar Pío XI (49.2°S, 73.6°W) is the largest glacier in South America located on the western side of the SPI (Figure 2.2). The glacier is 70 km long and covers an area of 1255 km^2 in 2018. The lowermost part of the glacier bifurcates into two ice tongues, the southern terminus terminating in Eyre Fjord and the northern terminus in Lago Greve. The depths of Eyre Fjord and Lago Greve were reported to be 30–50 m and ~150 m, respectively (Warren and Rivera, 1994; Warren et al., 1997). According to a multi-beam sonar survey in 2003–2008, the depth of Eyre Fjord near the ice-front was ~25 m (Dowdeswell and Vásquez, 2013). In the upper reaches of the bifurcating area, four outlet glaciers protrude from the main trunk and terminate in lakes (Sub1–4 in Figure 2.3), and marginal ice flows into lakes at three locations (Sub5–7 in Figure 2.3). These subsidiary icefronts were included in our analysis.

Glaciar Pío XI has a large accumulation area ratio (AAR = 0.81) (de Angelis, 2014). This means that a relatively large amount of accumulation is counterbalanced by frontal ablation as well as rapid melting in the ablation area. Mass balance modeling for the period from 1975 to 2011 showed a mean surface mass balance of +3.45 m w.e. and equilibrium line altitude (ELA) at 1055 m a.s.l. (Schaefer et al., 2015). The ice thickness is greater than 1300 m in the accumulation area, which is the second thickest ice in the SPI (Millan et al., 2019). No ice thickness measurement data is available in the ablation area.

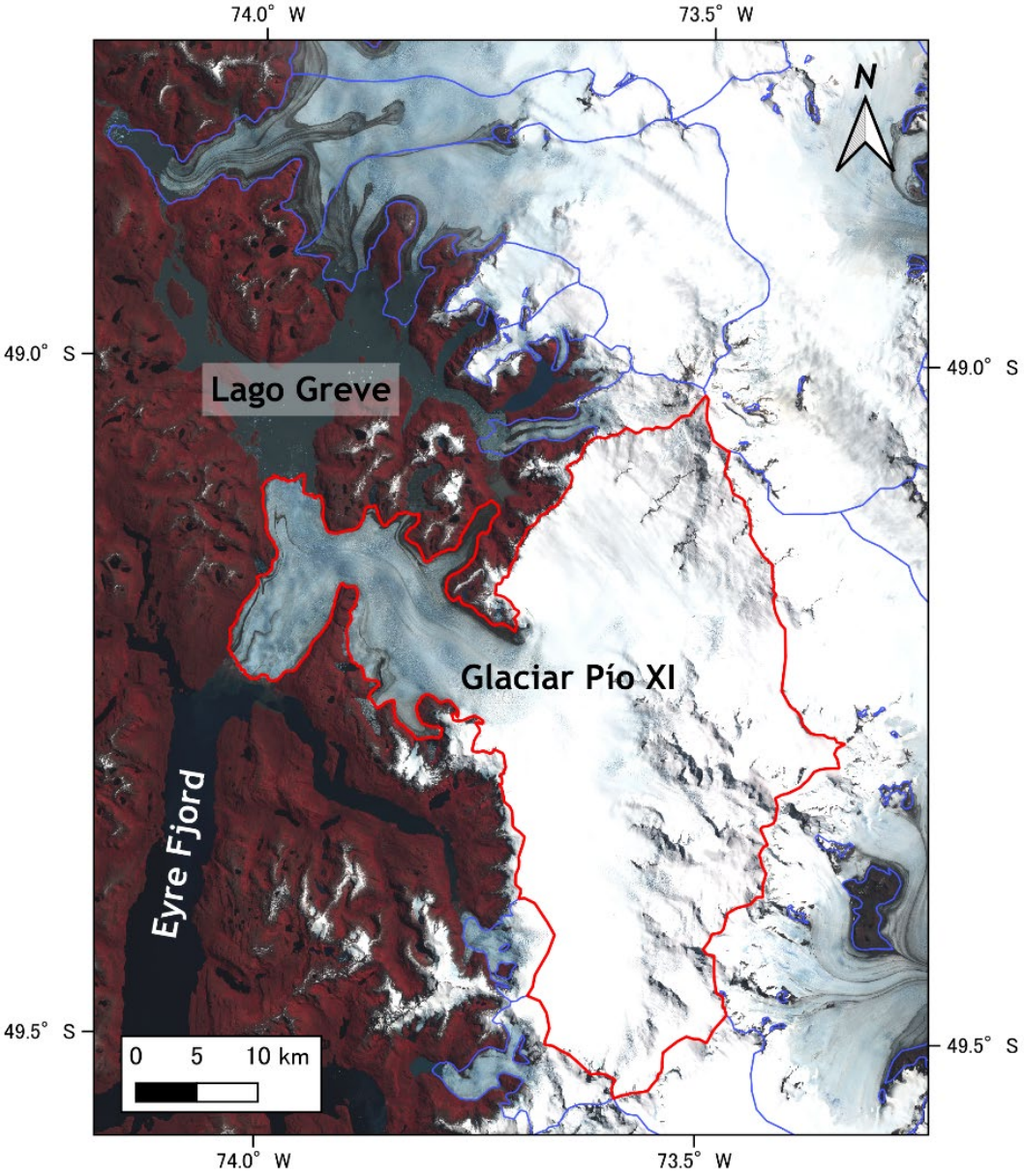

Figure 2.2. Satellite image showing Glaciar Pío XI. The image is false-color image of Sentinel-2 acquired on 20 January 2022, same day as Figure 2.1. Blue lines indicate glacier boundary by RGI 6.0 (RGI Consortium, 2017).

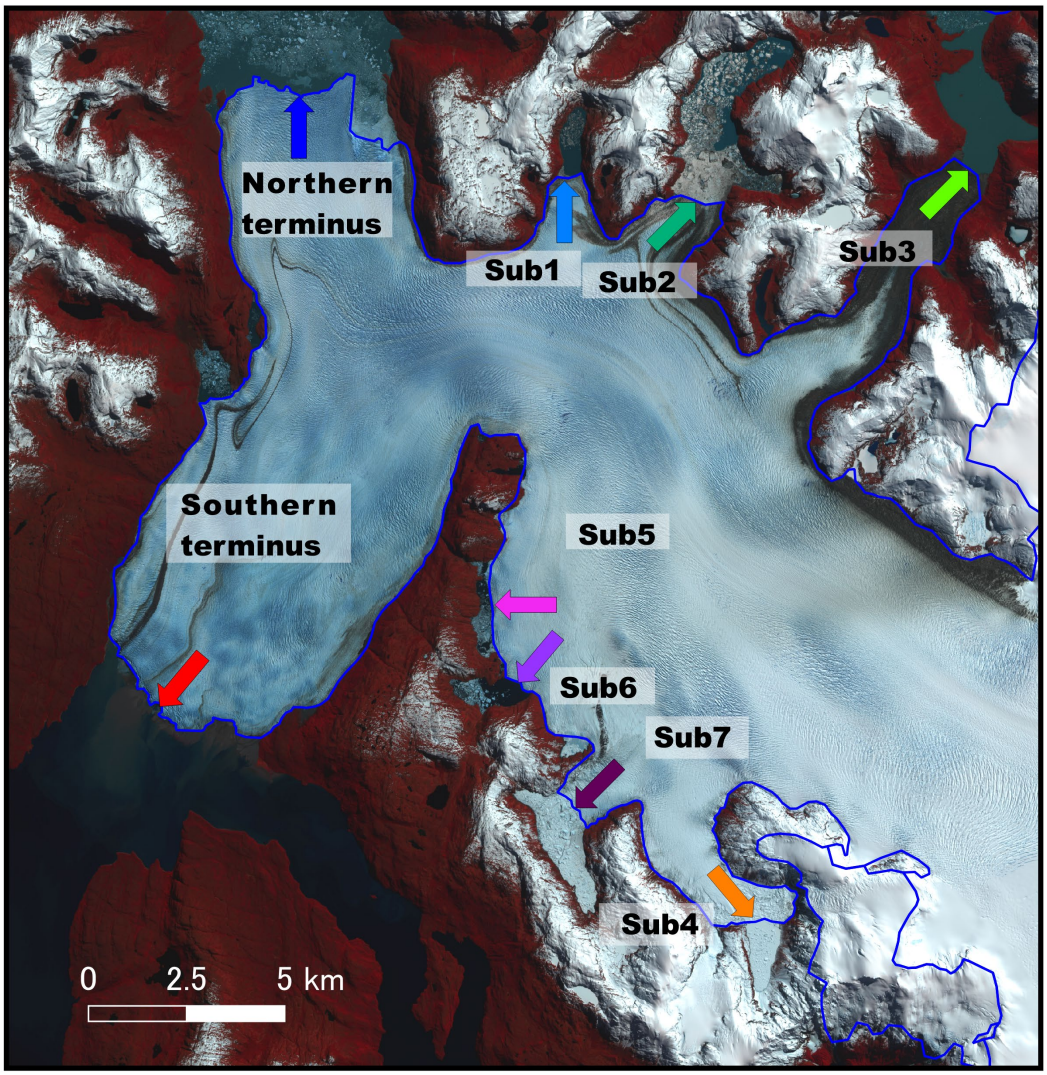

Figure 2.3. Satellite image showing ablation area of Glaciar Pío XI. The image is false-color image of Sentinel-2 acquired on 18 October 2018. Blue lines are glacier boundaries after RGI 6.0 inventory (RGI Consortium, 2017), except for the outline of Glaciar Pío XI traced on the background image.

2.3. Lago Greve

Lago Greve (49.0°S, 73.9°W) is a glacier-fed lake situated on the western side of the SPI (Figure 2.4). In November 2020, the lake covered an area of 187.9 km^2, making it the fourth largest proglacial lake in the world. Although no lake-depth measurement is available, the depth was estimated to be ≤150 m near the ice-front of the northern terminus of Glaciar Pío XI based on the lakebed geometry observed before the formation of the lake. The lakewater drains through a gorge at the northwestern margin of the lake, where an outlet stream falls off to a marginal lake of Glaciar Occidental over steep terrain with an elevation difference of ~130 m (Figure 2.4). From the lake outlet, water flows through fjords for a distance of ~130 km before entering into the Pacific Ocean.

The lake is fed by a number of outlet glaciers of the SPI, including Glaciar Pío XI, the largest glacier in Patagonia (Figure 2.4). Between 1945–1962, Glaciar Pío XI advanced and blocked Río Greve, a stream from an outwash plain feeding into Eyre Fjord (Rivera, 1992; Rivera et al., 1997a, b). The blocking resulted in the formation of Lago Greve as an ice-dammed lake (Rivera, 1992; Rivera et al., 1997a, b, 1999; Warren et al., 1997). After the formation of Lago Greve, between 1945–1962, rapid lake drainage has never been reported. In recent decades, the lake is fed by seven glaciers, the northern glacier front and one of the subsidiary outlet glaciers of Glaciar Pío XI, Glaciar Lautaro, and two outlet glaciers from each of Glaciar Greve and Glaciar HPS-8 (Figure 2.4).

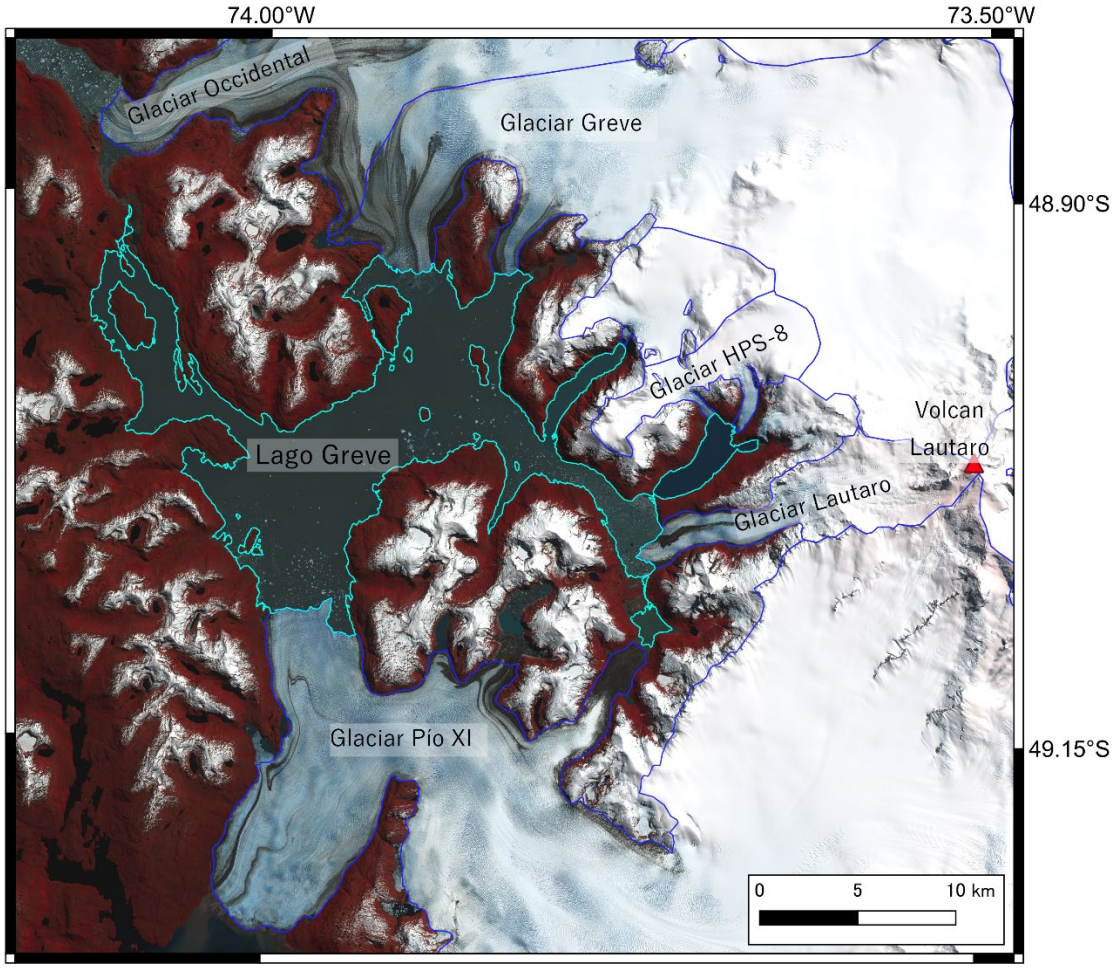

Figure 2.3. Satellite image showing Lago Greve. Cyan curve represents the shoreline on 1st November 2020, delineated in this study. The name of outlet glaciers from the SPI flowing into Lago Greve are also shown.

Chapter 3
Methods & data

3.1. Glacier measurements

3.1.1. Ice-front position

Changes in the ice-front positions of Glaciar Pio XI were measured by using optical satellite images acquired on 2 April 2000 to 23 December 2021.

Ice-fronts were manually delineated on the images using QGIS geographic information system software. The mean displacement of the ice-front was calculated by dividing the change in the surface area by the width of the glacier (Figure 2) (Moon and Joughin, 2008). The uncertainty in the ice-front position was estimated by repeating the measurement for all ice-fronts/margins on cloud-free images obtained by each sensor. Standard deviations of ten repeated measurements for each sensor were 3–7 m.

I used images of Landsat 5 Thematic Mapper (TM), Landsat 7 Enhanced Thematic Mapper Plus (ETM+), Landsat 8 Operational Land Imager (OLI), Terra Advanced Spaceborne Thermal Emission and Reflection Radiometer (ASTER), Sentinel-2 Multispectral Imager (MSI), PlanetScope Dove, and RapidEye (Table 3.1). In total, 135 images were used for this purpose. I used level-1 band 8 (panchromatic) images of Landsat 7 ETM+ and Landsat 8 OLI, level-1 band 3 (near-infrared) images of Terra ASTER, band 4 (near-infrared) images of PlanetScope of RapidEye. I used false color images converted from bands 4, 3, 2 of Landsat 5 TM and 8, 4, 3 of Sentinel-2 MSI.

Table 3.1. Satellite images used in this study

	Spatial resolution	Number of images for Chapter 4	Number of images for Chapter 5
Landsat 5 ETM+	30 m	11	-
Landsat 7 ETM+	15 m	9	2
Landsat 8 OLI	15 m	11	11
Terra ASTER	15 m	6	2
Sentinel-2 MSI	10 m	12	22
PlanetScope Dove	3 m	-	72
RapidEye REIS	5 m	-	1

3.1.2. Surface elevation change

3.1.2.1. DEMs used in the study

Changes in the glacier surface elevation were measured by differencing digital elevation models (DEMs).

A DEM in February 2000 was obtained by the Shuttle Radar Topography Mission (SRTM) and distributed by U. S. Geological Survey (USGS) (EROS Center, 2017). We also used ASTER-VA DEMs in February 2017, October 2018, and March 2021 distributed by the Japanese National Institute of Advanced Industrial Science and Technology (AIST) and the Geological Survey of Japan and these DEMs are available through the AIST website (https:// gbank.gsj.jp/madas/map/index.html). Uncertainties in the vertical coordinates of the SRTM and ASTER DEMs were reported as ±7m (Rignot et al., 2003) and ±29.5 m (Bolch et al., 2011), respectively.

In addition to these freely available DEMs, I produced two DEMs from stereo-pair images. Two DEMs on 15 March 2007 and on 15/16 August 2019 were constructed by processing stereo-pair satellite images obtained by Panchromatic Remote-sensing Instruments for Stereo Mapping (PRISM) mounted on the Japanese Advanced Land Observing Satellite (ALOS) and Satellite Pour l'Observation de la Terre (SPOT-6/7), respectively.

For ALOS-DEM construction, manual DEM construction was performed. Nadir- and forward-looking images with a processing level of 1B2 (geometrically corrected data) of ALOS/PRIMS images were used for this purpose. Rational polynomial coefficient (RPC) files distributed by the Remote Sensing Technology Center of Japan (RESTEC) were utilized for geolocation of the images. Photogrammetric analysis was performed using a photogrammetry software mounted on the ERDAS IMAGINE 2018 (Intergraph Co., Ltd.) workstation. The glacier and surrounding land surface elevation were surveyed based on a stereoscopic image generated by a three-dimensional monitor (PX 2210MW, PLANAR Co., Ltd.). We generated a triangulated irregular network of surface elevation in the stereoscopic space, which was subsequently processed to a 30-m gridded DEM by linear interpolation. The generated DEM covers the lower part of the glacier (20% of the total glacier area), excluding the snow-covered accumulation area where surface features required for the survey were unavailable. For this reason, the upper boundary of the area analyzed in this study is given by the snow line on the ALOS PRISM images acquisition date (15 March 2007).

For SPOT-DEM construction, an automated DEM construction method was performed. Basic Level 1B (radiometrically and sensor-corrected) SPOT-6/7 panchromatic stereo images with a resolution of 1.5 m were used for this purpose. Photogrammetry software Ames Stereo Pipeline (ASP) version 2.7.0 was employed to process the images for a 5-m resolution DEM. ASP constructs disparity map by applying image matching from stereo-pair images and corresponding RPC files. A point cloud was constructed by applying triangulation to the disparity, thereafter, point cloud was rasterized to construct a DEM.

ASTER images used to derive the DEMs are partially covered by clouds, thus we manually removed cloud-covered areas from the ASTER DEMs. After this procedure, the ASTER DEMs cover 188 km^2 of the glacier area, while the SRTM and ALOS DEMs cover 234 km^2. Mean elevation change was computed excluding areas without data.

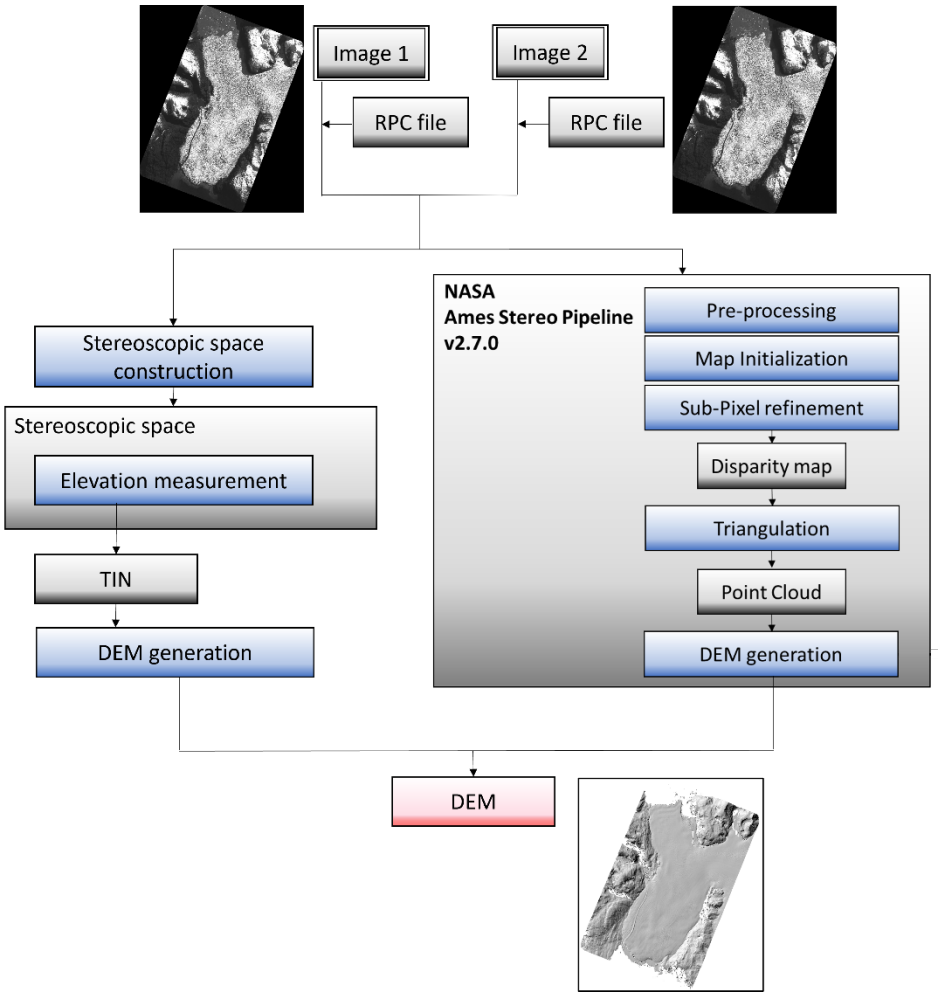

Figure 3.1. Workflow of the DEM construction.

3.1.2.2. Correction of DEMs

We followed the method proposed by Nuth and Kääb (2011) to remove three types of biases from the ASTER DEMs; horizontal shift, elevation dependent bias, and biases specific to the along/cross satellite track. The SRTM DEM was used as a reference in the procedure. Thereafter, vertical biases of the ASTER and ALOS DEMs were corrected for the SRTM DEM by differing the DEMs out of the glacier, where elevation change is assumed to be negligible. This analysis was performed in off-ice areas covering 159 km^2 within 8 km from the glacier, excluding steep terrains with a slope greater than 30°. After

the corrections, standard deviation (σ_{ref}) of the elevation change within the off-ice areas were 15.0 m from 2000 SRTM DEM to 2007 ALOS DEM, 30.3 m from 2007 ALOS DEM to 2017/18 ASTER DEM, and 29.6 m from 2000 SRTM DEM to 2017/18 ASTER DEM. To evaluate the accuracy, we compared ALOS DEM on 15 March 2007 with elevation surveyed by airborne laser altimetry on 28 July 28 2007 (Wilson et al., 2016). Along the centerline connecting the northern and southern termini (Figure 3b in Wilson et al., 2016), ALOS DEM shows 8.2 m lower elevation on average. This is consistent with a seasonal variation expected near the front of this glacier. Within the four-month period from late summer to midwinter, surface elevation substantially increases because of vertical straining and snow deposition. The standard deviations provide measures of accuracy for elevation change evaluated at each DEM grid point. Accuracy improves after averaging the elevation changes over a large area.

3.1.2.3. Uncertainty of elevation change measurement

The uncertainty in the aerial mean was estimated from standard error (*SE*) defined as

$$SE = \frac{\sigma_{\text{ref}}}{\sqrt{n_{\text{eff}}}} \tag{3.1}$$

where n_{eff} is the number of independent measurements within the area of concern. To compute n_{eff}, I followed the method described in Bolch et al. (2011) as

$$n_{\text{eff}} = \frac{n_{total} \cdot PS}{d} \tag{3.2}$$

where n_{total} is the number of total grid samples within the area of concern in the DEM, which spatial resolution as PS. I used the decorrelation length d to 600 m, similar to previous studies based on ASTER and SRTM DEMs (Bolch et al., 2011; Gardelle et al., 2013). Our photogrammetric analysis using ALOS images was performed with a higher spatial density. Further, elevation measurement by photogrammetry is generally more accurate on a glacier surface than on off-glacier terrain because the ice surface is relatively flat and covered with clear surface features. Thus, the estimate above gives a relatively conservative measure for the error range of our analysis.

Table 3.2. DEMs used in the study.

DEM	Spatial resolution	Period	Glacier elevation	Lake level
SRTM	30 m	2000-02-11–22	✓	✓
ALOS/PRISM	30 m	2007-03-15	✓	-
ASTER	30 m	2017-02-26	✓	-
ASTER	30 m	2018-10-29	✓	-
SPOT-6/7	5 m	2019-08-15 2019-08-16	✓	-
WorldView-2	5 m	2020-07-21	-	✓
ASTER	30 m	2021-03-02	✓	-

3.1.3. Glacier velocity

Glacier flow velocity was measured by applying a feature tracking technique to optical satellite images obtained by Landsat 8 and Sentinel-2. Displacements between first image to the next image were estimated by applying image-matching method (e.g., cross-correlation, orientation correlation) in a feature tracking technique workflow. Therefore, the velocity was calculated as the mean velocity between the date of first and the next images. To obtain glacier velocity, I used the ImGRAFT (Image GeoRectification and Feature Tracking) (Messerli and Grinsted, 2015), which is a feature tracking toolbox available on and written in MATLAB. Displacement measurement was performed with a 21 × 21 pixels target window and 61 × 61 pixels search window. The pixels of less than threshold of signal to noise ratio (SNR<5) was removed as noise. Spatial distributions of velocity were generated with spatial resolution as 120 m. I assumed velocity of bedrock region is negligible, the mean velocity on bedrock region neighboring glaciers was taken as the uncertainty of the measurement.

In addition to obtain velocity from satellite images, I used freely available glacier flow velocity products, ITS_LIVE (Gardner et al., 2018, 2019) and RETREAT (Friedl et al., 2021). The ITS_LIVE project provides year mean glacier surface velocity product calculated by applying a feature tracking method to images of Landsat 4–8, the period covers from 1985 to present, and the spatial resolution is 240 m. The RETREAT product provides image-pair, monthly mean, and yearly mean velocity field, which was calculated by applying offset tracking method to Sentinel-1 backscatter intensity images. The period covers from 2014 to present, and the spatial resolution is 200 m. I utilized yearly-mean ITS_LIVE products for the period of 2000–2018. I also utilized monthly-mean and image-pair velocity products of the RETREAT project for the period of 2016–2020.

3.2. Lake measurements

3.2.1. Lake area

The area of Lago Greve was measured from 28 September 2016 to 1 November 2020, by using 19 satellite images acquired by Sentinel-2 MSI and Landsat 8 OLI. The lake margin was manually delineated on false-color composite images on the QGIS geographic information system software. False-color images were converted from near-infrared, green and red band images (bands 8, 4, 3 of Sentinel-2 MSI, and 5, 4, 3 of Landsat 8 OLI). We utilized normalized differential water index (NDWI) to distinguish water and land in regions covered by shades. NDWI is commonly used to detect water bodies in satellite images. The index is defined as

$$NDWI = \frac{R_{\mathrm{G}} - R_{\mathrm{NIR}}}{R_{\mathrm{G}} + R_{\mathrm{NIR}}} \tag{3.3}$$

where R_{G} and R_{NIR} are the reflectance of green and near-infrared bands at the top of the atmosphere (e.g., McFeeters, 2013). To evaluate the contributions of glacier retreat and advance to the lake area, changes in the glacier areas near the front were also measured by the images. To constrain the onset of the drainage event, I also used backscatter images of synthetic aperture radar (SAR) obtained by Sentinel-1 satellites.

I utilize NDWI index to distinguish sediment from water in satellite images. I determined a threshold as NDWI < 0.3 by visual inspection of the sedimentary delta observed on the image on 2 April 2000. This threshold is within a range reported in previous studies (e.g., McFeeters, 2013).

3.2.1.1. Uncertainty of area measurement

A lot of studies measured areas of glacier and glacial lakes by using optical satellite data, they evaluated the measurement uncertainty. One of the most widely used method is

"buffer method" proposed by Paul et al. (2017). Hanshaw and Bookhagen (2014) proposed an idea for evaluation of uncertainty of glacial lake area that error range is equally distributed from the measurement line (Figure 3.2), which is a similar method to "buffer method". This method is suitable for pixel-based threshold area measurement. In addition, this method is reasonable when the number of targets is large because of the simplicity. However, to retrieve the maximum/minimum area calculated by these methods, all the nodes have to be shifted full range of error range to outside/inside from the manually delineated outline. Thus, uncertainty range of these methods can be interpreted maximum error, i.e. the conservative value for the error between the measured value and true value (Figure 3.2). Thus, these error estimations are suitable for pixel-based automatic classification.

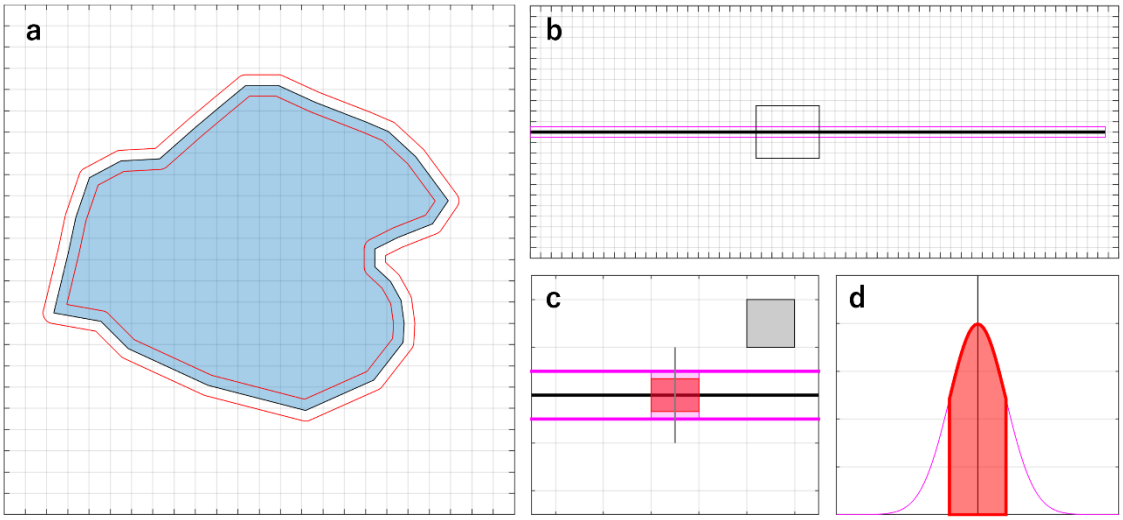

Figure 3.2. Schematic figure of widely used error assessment methods. (a) Light blue area with black curve denotes an example polygon. Red curves indicates "buffer polygon" which is generated between certain distance from the original polygon to be uniform. In this case, the buffer distance is set to be a half of one grid size. (b–d) Conceptual frame work of a uncertainty evaluation method for polygon area proposed by Hanshaw and Bookhagen (2014). (b) Black and magenta lines indicate the perimeter length of a original polygon in (a) and rectangle with height as oen grid size. (c) Close up view of box in (b). Gray box represents a unit area. (d) Schmeatic illustration of cross section of the vertical line in (c). Red area in (c, d) indicates the uncertainty area of 68.72% (1σ) to one grid length of the perimeter.

Here, I propose a method to evaluate uncertainty along the polygon created by manual delineation (Figure 3.3). Uncertainty in the lake area was estimated by assuming that the individual measurement along the lake margin has an error up to the image resolution. Lake area computation was repeated enough times by randomly shifting the nodes of the lake polygon within the range of the resolution. The number of repeated trials should be determined as appropriate according to the situation. Standard deviation of the repeated computation was then estimated as the uncertainty of the manual delineation. This method could provide appropriately uncertainty. Care should be taken about this method provides uncertainty of the measurement, not the error between the measured value and true value.

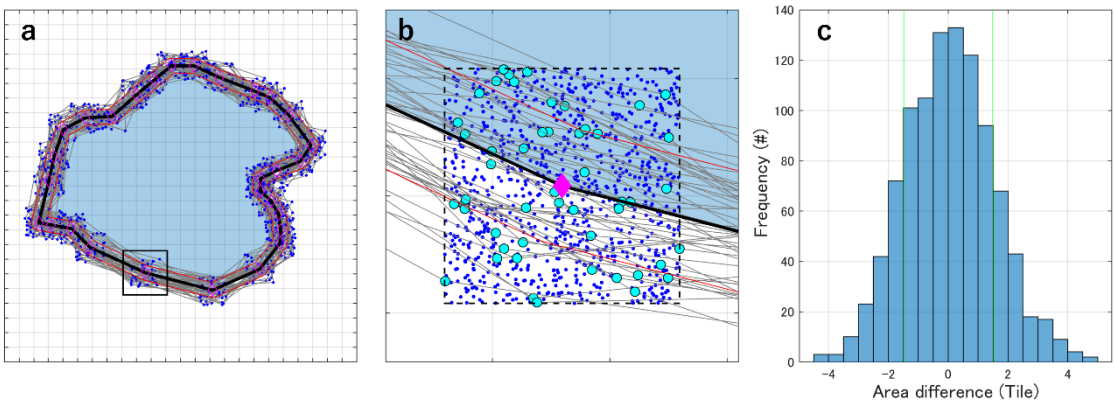

Figure 3.3. Schematic figure of our method of uncertainty assessment. (a) Light blue area with black curve denotes a polygon same as Figure 3.2a. Red curves indicate "buffer polygons" with distance of half of one grid tile. Magenta diamond and blue dots indicate node of original polygon and after random shifting, respectively. Black box indicates the region of (b). (b) Enlarged view of one node of the original polygon. Dashed box indicates the area where random points generated. Note that selected shifted polygons are shown with cyan node for visibility. (c) Histogram showing the difference in area between original and random shifting polygons. Green lines indicate one standard deviation.

Uncertainty in the area of Lago Greve was estimated by assuming that the individual measurement along the lake margin has an error up to the image resolution. Lake area computation was repeated 1000 times by randomly shifting the nodes of the lake polygon within the range of the resolution. Standard deviation of the repeated computation was ±0.02 km^2 for both of the MSI and OLI images (Figure 3.4).

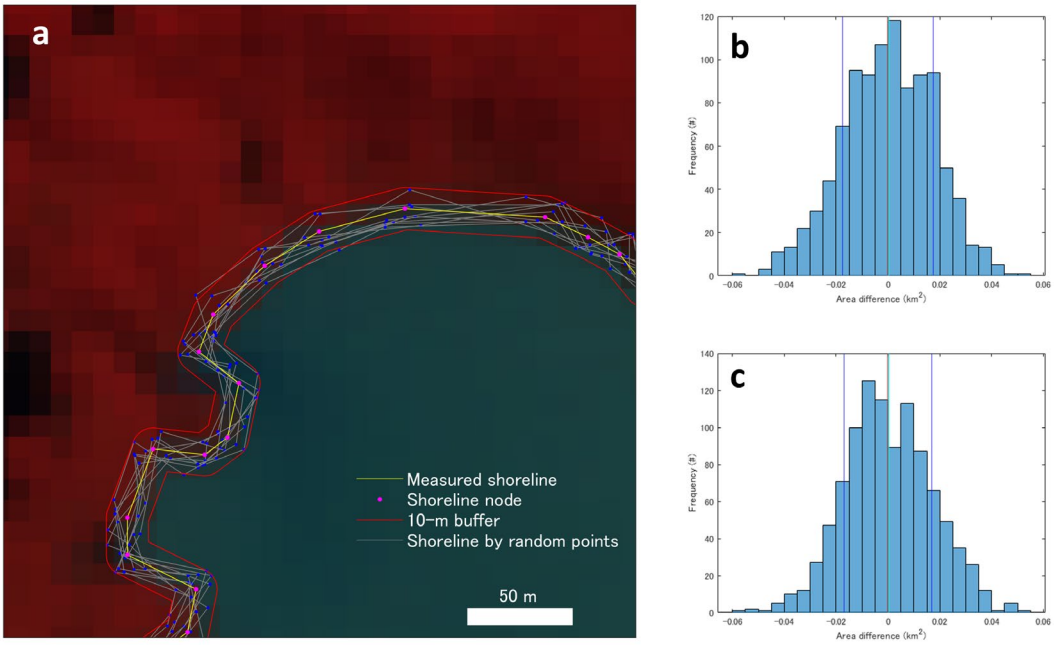

Figure 3.4. Uncertainty in the lake area measurement. (a) Example of uncertainty evaluation of proposed method, applied to Lago Greve. (b, c) Histogram showing are difference between measured lake area by manually and by random shifting for (b) Landsat 8 OLI and (c) Sentinel-2 MSI. Red, green, and blue lines indicate mean, median and standard deviations of the difference.

3.2.2. Lake water level

Water surface elevation of Lago Greve was measured from 28 September 2016 to 1 November 2020 with intervals of five days to six months based on satellite laser altimetry and DEMs.

Data from Advanced Topographic Laser Altimeter System (ATLAS) mounted on Ice, Cloud, and Land Elevation Satellite-2 (ICESat-2) was analyzed during a period from November 2018 to July 2020. In this study, we used ICESat-2/ATLAS L3A Inland Water Surface Height products (ATL13), which provide lake- and river-surface heights above the Earth Gravitational Model 2008 mean sea level (Jasinski et al., 2019). I used the ATL13 point data obtained within the lake area. Data acquired on the same day were averaged and the standard deviations were taken as a measure of uncertainty.

From September 2016 to November 2020, the lake level was also measured by reading elevation along the lake margin from DEMs. I used a DEM derived from Shuttle Radar Topography Mission (SRTM-DEM) on February 2000, which is distributed by U.S. Geological Survey (USGS). Spatial resolution and uncertainty in the vertical coordinates of the SRTM-DEM were 30 and ±7 m, respectively (Rignot et al., 2003). To obtain the elevation of the lake shore emerged after the onset of the drainage (April–November 2020), I generated a 5-m resolution DEM (WV-DEM) by applying a photogrammetric technique to a stereo pair WorldView-2 satellite images acquired on 21 July 2020 (©2020 DigitalGlobe Inc., a Maxar company). Basic Level 1B (radiometrically and sensor-corrected) WorldView-2 panchromatic stereo images with a resolution of 0.55 m were used for this purpose. I processed the photogrammetric workflow by using ASP version 2.7.0 described as the section above (Section 3.1.2). The DEM covers an area of 25 km^2. Vertical coordinates of the WV-DEM were corrected for the SRTM-DEM. The 5-m-resolution WV-DEM was resampled at grid points with a resolution of 30 m. The WV-DEM and SRTM-DEM were compared over a relatively flat terrain with a slope less than 15 degrees (Figure 3.5). The mean difference in the vertical coordinates (5.4 m) was

corrected and the standard deviation between the two DEMs (±5.6 m) was taken as a measure of the uncertainty of WV-DEM (Figure 3.5).

Vertical offsets of the DEMs against the altimetry data were corrected by comparing lake-surface elevation from the DEMs with those obtained by altimetry within seven days. The mean difference from the altimetry data (+2.5 m for SRTM-DEM and −1.4 m for WV-DEM) was used for the correction of DEM derived lake level. Data during the drainage period was excluded from the offset evaluation because water level change in seven days was too large.

The SRTM-DEM was used for the period before the drainage event (from September 2016 to April 2020), whereas the WV-DEM was used for that after the event (from April to November 2020). The DEMs were used also for investigation of the terrain near the outlet of the lake.

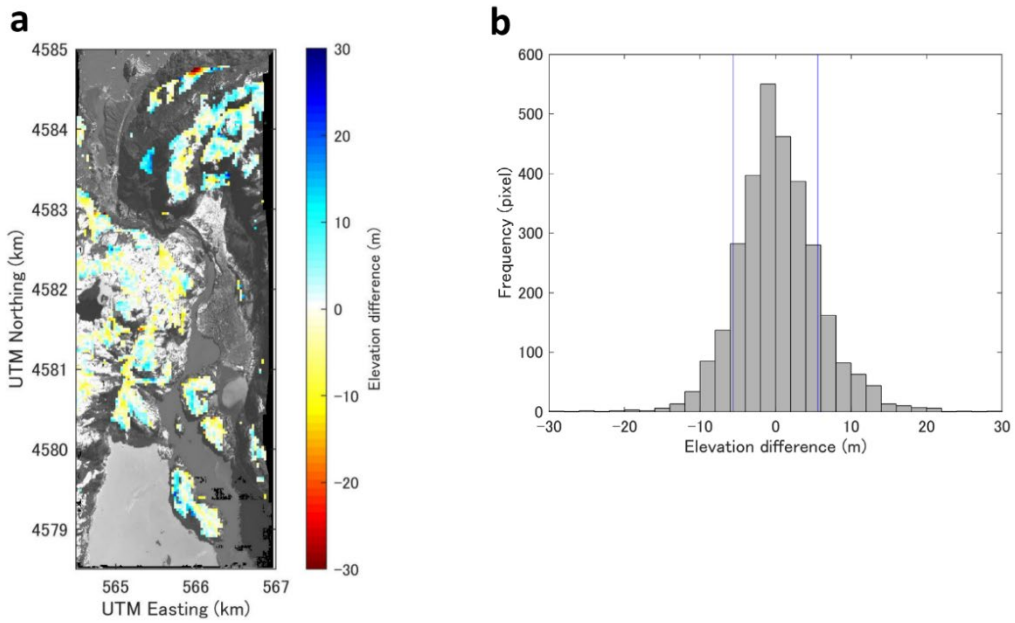

Figure 3.5. Uncertainty of the WV-DEM. (a) Map and (b) histogram showing the elevation difference between SRTM-DEM and WV-DEM over the region of the outlet of Lago Greve. Blue lines in b indicate the range of the standard deviation. Background image of (a) is WorldView-2 on 21 July 2020 (©2020 DigitalGlobe Inc., a Maxar company).

3.2.3. GRACE mascon solution

To investigate the effect to the gravity distribution by the drainage event of Lago Greve, monthly mass concentration (mascon) data were analyzed in the study region, using mascon solutions distributed by the Center for Space Research (CSR), the University of Texas at Austin (Save et al., 2016). These mascon solutions were derived by the Gravity Recovery and Climate Experiment (GRACE) and GRACE Follow-On (GRACE-FO) satellite gravimetry systems. Geodesic grids were located on the earth surface with intervals of ~120 km. Note that the CSR mascon product is provided as a 0.5° grid data set, which was generated by resampling original mascon solution. Changes in the mass from April 2002 to December 2019 were averaged over regions within 200, 300, 400 km from the center of the lake considering the resolution of the GRACE measurement of 200–400 km (Sasgen et al., 2019). The mascon time-series was modelled with a function composed of linear, seasonal, and decadal variation terms.

$$M(t) = \sum_{i=1}^{3} \left(k_{2i-1} \sin \frac{2\pi}{T_i} t + k_{2i} \cos \frac{2\pi}{T_i} t \right) + k_7 t + k_8 \tag{3.4}$$

There, M is the time-variable mass, t is the time since 16 April 2002, $T_{i=1}$ indicate periods of annual, semiannual and decadal cycles, and k_{1-8} are coefficients estimated by the least-squares method. I also compared the spatial distribution of mascon in March and August 2020. To eliminate seasonal variations, the data sets were corrected for mean difference between March and August observed from 2002–2019.

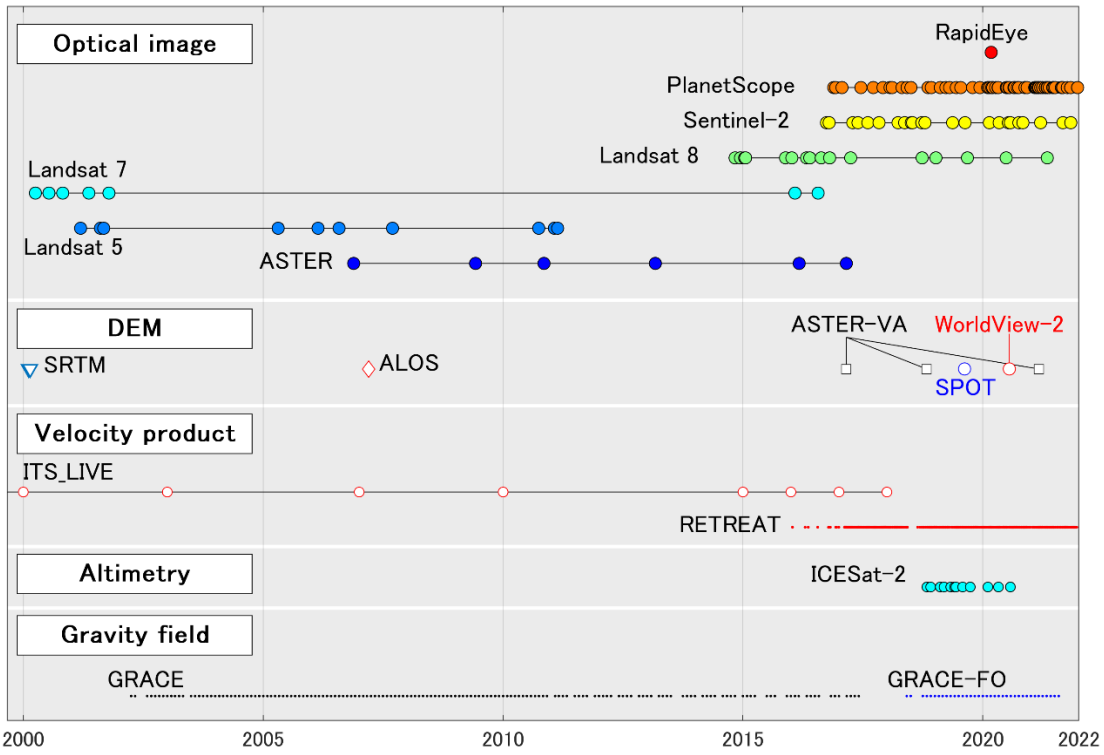

Figure 3.6. Summary of the satellite data used in the study.

Chapter 4
Results part 1:
Variation of Glaciar Pio XI since 2000

The contents in this chapter were published on *Frontiers in Earth Science*.

Hata, S., and S. Sugiyama, (2021).

Changes in the Ice-Front Position and Surface Elevation of Glaciar Pío XI, from 2000–2018. *Frontiers in Earth Science*, **8**:576044, doi:10.3389.2020.576044.

In order to investigate the recent unique change of Glaciar Pío XI, I measured the changes in ice-front position and surface elevation from a period of 2000–2018. The procedures were described in Chapter 3. In addition to the glacier variation, sediment deposition at Eyre Fjord in front of the Southern terminus is also observed by optical satellite imagery.

4.1. Ice-front position

From April 2000 to October 2018, the southern and northern termini, four outlet glacier tongues and three locations of the ice margins of Glaciar Pío XI showed advancing trends (Figure 4.1). The southern terminus advanced by 1400 m and its surface area increased by 6.6 km^2 (Figures 4.1a and 4.2). The terminus progressively advanced from 2000 to 2016 with a mean rate of 86 m a^{-1}. A retreat of 150 m was observed between April 2016 and August 2017, but the glacier advanced again by 160 m from August 2017 to October 2018. After a 300 m retreat in 2000–2005, the northern terminus advanced by 1160 m in 2005–2018 (Figures 4.1b and 4.2). The mean displacement rates during the two periods were −51 and 92 m a^{-1}, respectively. The advance in the latter period was interrupted by short (<1 year) and small (< 250 m) retreat episodes in 2010, 2015, 2016 and 2018. The total advance during the study period was 860 m, and the surface area increased by 3.9 km^2.

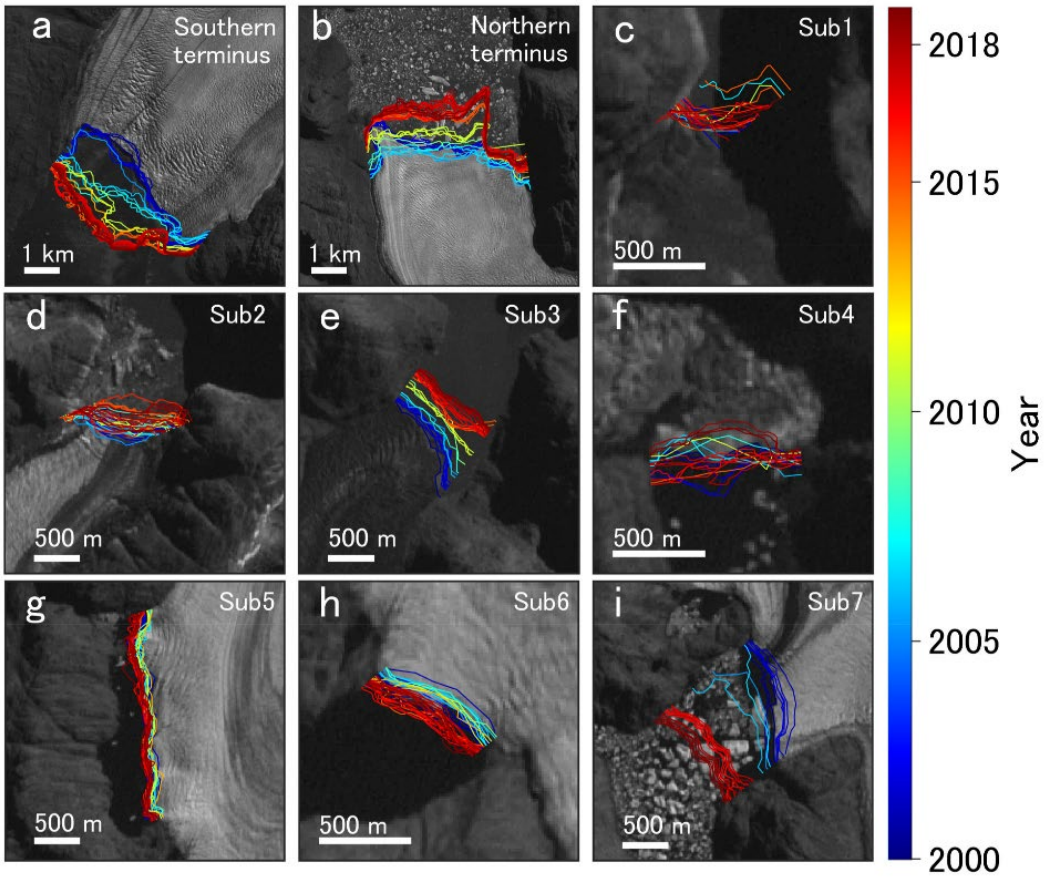

Figure 4.1. Ice-front position change of Glaciar Pío XI. The background images were taken from Landsat 7 ETM+ band 8 acquired on 2 April 2000.

Four of the outlet glacier tongues (Sub1–4) and three locations of the ice margins (Sub5–7) showed generally advancing trends during the study period (Figures 4.1c–i, 4.2). Each ice-front showed substantially different short-term variations and total displacement. The frontal variations of these subsidiary icefronts are categorized into three types. Sub3 and Sub7 have experienced a relatively large advance (> 500 m) over the study period with mean displacement rates of 30 and 54 m a^{-1}, respectively. Front positions of Sub5 and Sub6 have been relatively stable, i.e. fluctuations over the study period were within ±120 m. The rest of the ice-fronts (Sub1, Sub2 and Sub4) showed larger short-term variations, but total displacement over the study period was small (<100 m). For example, Sub1 rapidly advanced by 300 m from February to November 2006, which was followed by a relatively stable period from 2006 to 2014 and a sudden retreat of 350 m from

November 2014 to January 2015 (Figure 4.2). Sub1 and Sub2 showed similar short-term frontal variations, e.g., rapid retreat of Sub1 in 2015 corresponded to similar retreat of Sub2 in 2016.

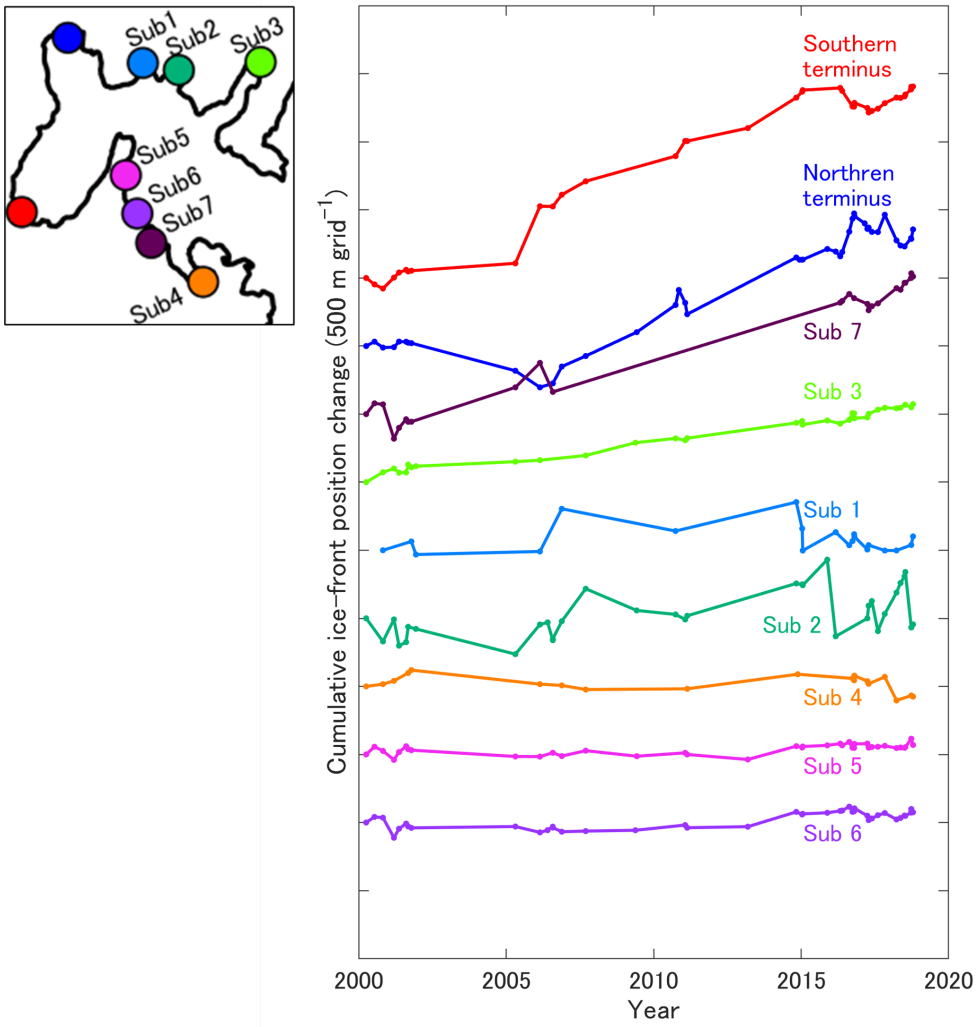

Figure 4.2. Ice-front position change of Glaciar Pío XI. Cumulative displacement of the ice-front positions since April 2000.

4.2. Surface elevation change

The glacier surface showed significantly large uplift during the study period (Figure 4.3). Surface elevation increased by 37.3 ± 0.4 m (2.09 ± 0.02 m a^{-1}) as a mean over the study area from February 2000 to February 2017/October 2018 (Figure 4.3a). From 2000 to 2007 (Period 1), mean elevation change over the area covered by the 2017/18 ASTER DEM was 8.1 ± 0.2 m (1.14 ± 0.03 m a^{-1}) (Figure 4.3b), which was equivalent to an ice volume increase of 1.90 ± 0.04 km^3 (0.26 ± 0.01 km^3 a^{-1}). Greater elevation change (29.2 ± 0.4 m and 2.69 ± 0.04 m a^{-1}) and volume change (6.85 ± 0.10 km^3 and 0.62 ± 0.01 km^3 a−1) were observed in the following period 2007–2017/18 (Period 2) (Figure 4.3c), which indicated a 135 ± 10% increase in rate change from the previous period.

Spatial patterns of the elevation change are significantly different in Period 1 and Period 2 (Figures 4.3b–d), which were analyzed along the central profiles taken by Wilson et al. (2016) (Figure 4.4). During Period 1, an extraordinary large elevation change (> 15 m a^{-1}) was localized near the front of the southern terminus (Figures 4.3b, 4.4c and 4.4d). Along the profile, mean elevation change within 12 km from the icefront of the southern terminus was 32.2 ± 0.4 m, whereas mean elevation change was only −1.2 ± 0.2 m in the upper reaches (12–30 km from the southern front) (Figures 4.4a and c). Elevation change during Period 2 was more uniformly distributed over the study area (Figures 4.3c, 4.4a and 4.4c), i.e., elevation increased by 36.3 ± 0.8 m in the lower 12 km and 24.7 ± 0.5 m in the upper reaches (Figure 4.4a). Accordingly, elevation change accelerated from Period 1 to Period 2, except for the regions near the southern terminus and one of the outlet ice tongues located in the southern portion of the main trunk (Sub4) (Figure 4.3d). The change in the spatial pattern is also clear along the profile connecting the southern and the northern termini (Figures 4.4b and d). During Period 1, elevation change was small near the front of the northern terminus in contrast to the south. Elevation change during Period 2 was more uniformly distributed across the two termini, showing a clear increase (from 0.40 ± 0.09 to 3.78 ± 0.14 m a^{-1}) near the northern terminus compared to Period 1 (Figures 4.4c and d).

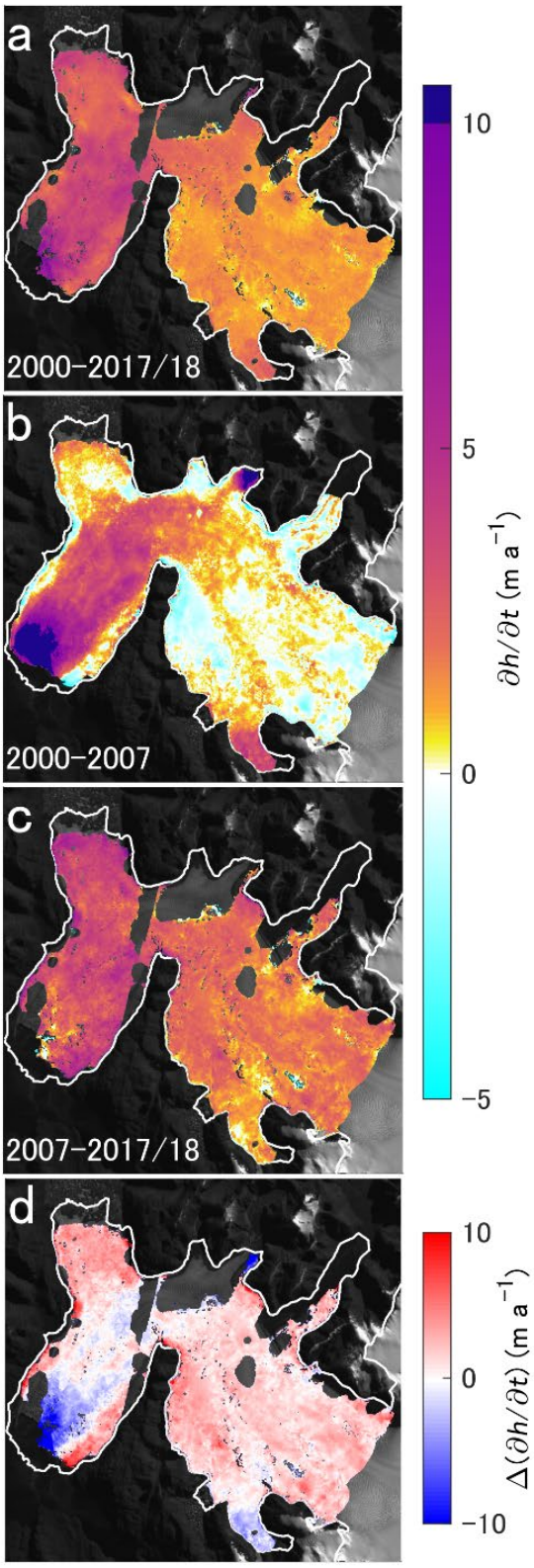

Figure 4.3. Spatial distribution of elevation change rate

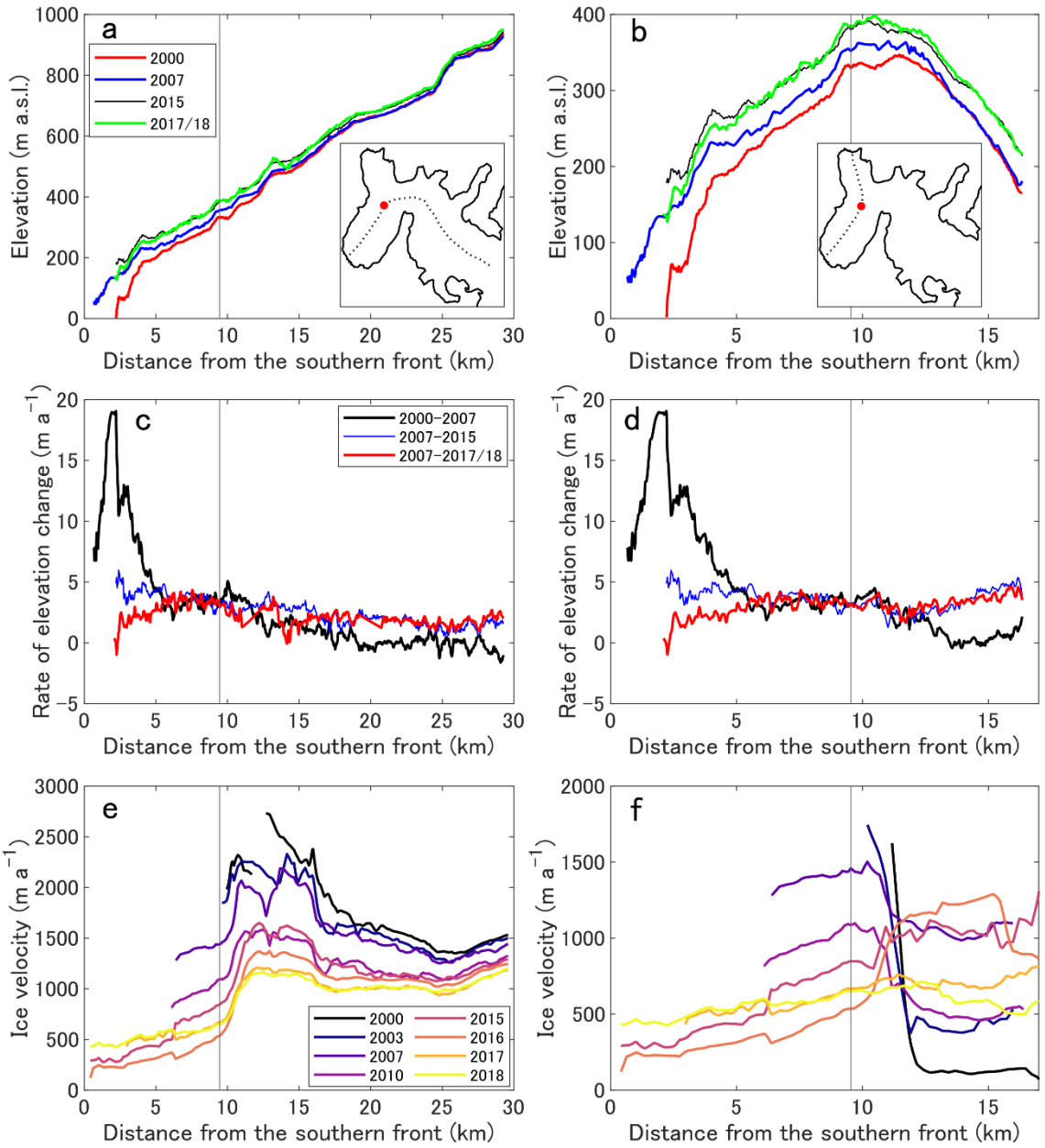

Figure 4.4. Glacier surface elevation, surface elevation change, and glacier velocity along two profiles.

4.3. Glacier velocity

Ice speed along the centerline showed a clear decelerating trend from 2000 to 2018 (Figure 4.4e). Speed near the branch point (red dot in Figure 4.4a) was about 2 km a^{-1} in 2000, which decreased to ~1 km a^{-1} in 2010 and thereafter progressively decelerated (Figures 4.4e,f). This observation is consistent with previous studies based on different data sources (Muto and Furuya, 2013; Sakakibara and Sugiyama, 2014; Mouginot and Rignot, 2015; Wilson et al., 2016; Abdel Jaber et al., 2019). Moreover, the spatial distribution of the glacier velocity shows progressively decrease in 2000–2018 (Figure 4.5).

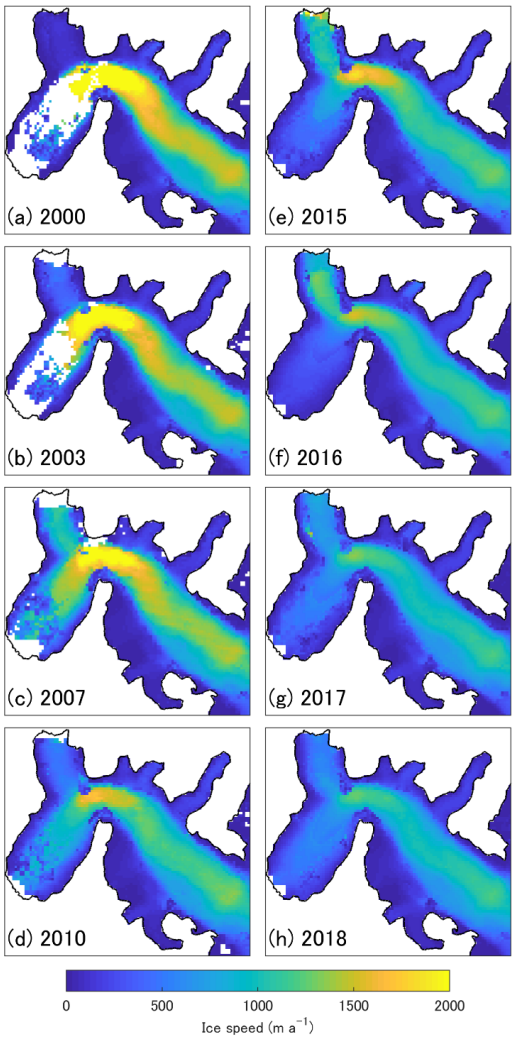

Figure 4.5. Spatial distribution of annual mean glacier flow velocity.

4.4. Ice volume change

Our analysis showed substantial thickening over the ablation area of Glaciar Pío XI during the study period. The rate of elevation change for the period 2000–2017/18 (2.09 ± 0.04 m a^{-1}) is consistent with previous studies of the ablation area of the glacier, based on SRTM and ASTER DEMs (2.4 m a^{-1} in 2000–2012) (Willis et al., 2012), and on SRTM and TanDEM-X DEMs (3.5 m a^{-1} in 2000–2012) (Abdel Jaber, 2016). The rate of ice mass increase during the study period was 0.48 ± 0.03 Gt a^{-1}, which corresponds to 4% of the total mass loss from the SPI from 2000 to 2015/16 (Malz et al., 2018). The rate increased by 135 ± 10% from Period 1 to Period 2. Accelerated thickening is consistent with a recent study, which reported elevation changes over the entire glacier surface as 0.42 m a^{-1} in 2000–2012 and 1.01 m a^{-1} in 2012–2016 (Abdel Jaber et al., 2019). The reported rates over the entire glacier are significantly smaller than our result, indicating pronounced thickening in the ablation area. This is consistent with the data reported by Abdel Jaber et al. (2019), which show clear thickening in the ablation area in contrast to small change in the accumulation area.

Thickening of Glaciar Pío XI is unique in Patagonia, but some glaciers in other regions show thickening trends as well. Taku Glacier in Alaska thickened by ~50 m in the terminus area between 1994 and 2003 (Motyka et al., 2006). Repeated radar surveys showed that surface elevation change accounted for less than a half of the thickness change, indicating rapid excavation of basal sediments. This study suggests that a similar process is occurring underneath Glaciar Pío XI and mass gain is greater than that computed from the surface elevation change. Subglacial excavation near the terminus of Glaciar Pío XI is likely, because rapid sediment deposition was observed in front of the glacier as described in the next subsection. Harvard Glacier, a tidewater glacier in Alaska, showed surface uplift in 1950/57–2001/04 at a rate of 0.058 m a^{-1} (Arendt et al., 2006). Some of the basins of Vestfonna in Svalbard showed thickening between 1990 and 2005, resulting in a mean elevation change of 0.05 m a^{-1} (Nuth et al., 2010). Thickening in the

Kunlun region, High Mountain Asia, was estimated as 0.21 m a^{-1} for the period between 2000 and 2016 (Brun et al., 2017). In a comparison with the data reported in other glaciers, the elevation change obtained in our study demonstrates that Glaciar Pío XI is one of the most rapidly thickening glaciers in the world.

4.5. Sediment deposition in front of the glacier

A close investigation of the satellite images revealed the emergence of sedimentary mound above ocean surface near the ice-front of the southern terminus since 2011 (Figure 4.6). Between April 2000 and September 2010, sediment deposition was observed at the glacier front only near the eastern margin (Figures 4.6). Turbid water was draining and spreading into the fjord from a sedimentary delta formed at the side of the glacier. After the first observation in 2011, the area of sedimentary mound exposed above water gradually expanded in the fjord (Figure 4.6). In October 2018, a band of sediment deposition extended along the glacier front, covering nearly 80% of the frontal margin (Figure 4.6). The glacier front advanced by 1,400 m from 2000 to 2018, thus the deposition was likely due to excavation of fjord sediment and/or sediment transport by subglacial meltwater discharge.

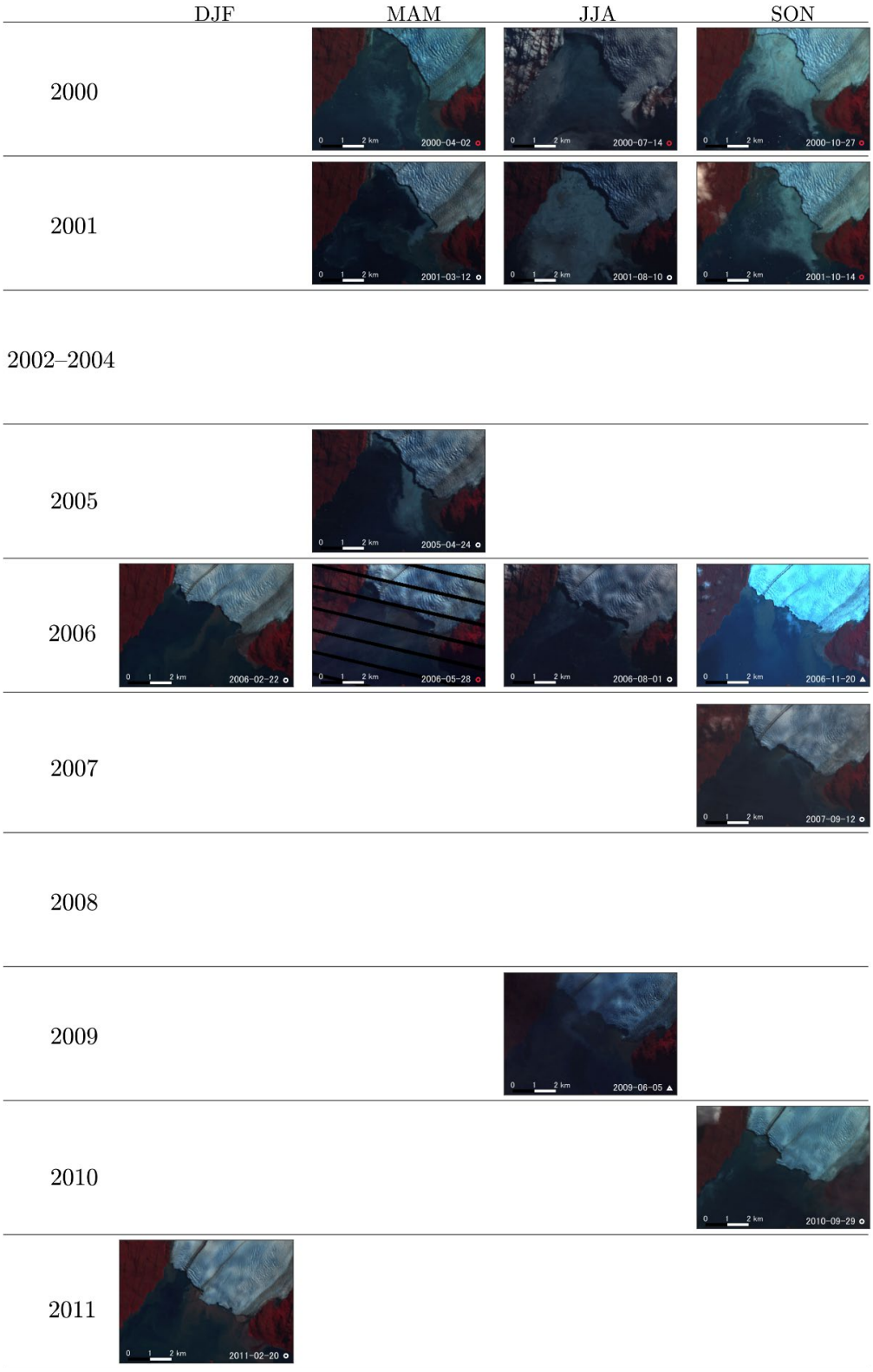

Figure 4.6. Satellite images showing the southern terminus in 2000–2020.

Figure 4.6. (Continued).

4.6. Summary

In this chapter, recent changes in the ice-front positions and surface elevation of Glaciar Pio XI, the largest glacier in the SPI. Most of the ice-fronts showed advancing trends over the study period. The greatest advance (1,400 m from 2000 to 2018) was observed at the southern terminus. The northern terminus and some of the subsidiary ice-fronts advanced by several hundred meters during the same period. Glacier-surface elevation increased at a rate increasing from 1.14 ± 0.03 m a^{-1} in 2000–2007 to 2.69 ± 0.04 m a^{-1} in 2007–2017/18. If we assume this elevation change is totally due to ice thickness change, the mass gain is equivalent to 4% of the mass loss in the SPI from 2000 to 2015/16. Our data demonstrated that Glaciar Pío XI is one of the most rapidly thickening glaciers in the world. Satellite images indicated sediment deposition and formation of a mound in front of the southern terminus, the mound covered ~80% of the width of the ice-front in October 2018.

Chapter 5

Results Part 2:

Changes in glacier variation after the lake drainage

A part of the contents in this chapter is under review of *Communications Earth & Environment*.

Hata, S., S. Sugiyama, and K. Heki,

Abrupt drainage of Lago Greve, a large proglacial lake in Chilean Patagonia, observed by satellite in 2020, in revision.

5.1. Background

The shoreline retreat was observed along the entire of margin of the lake by satellite images. Lake floor emergence was observed along the entire shoreline of Lago Greve in 2020 (Figure 5.1), suggesting the abrupt lake level drop there. In order to investigate the effect to glacier evolution from the lake level change, satellite observations were performed at Lago Greve and the northern terminus of Glaciar Pío XI, flowing into the lake.

Further, Lago Greve is fourth largest glacial lake by area, released water volume is expected to be massive. Therefore, large mass change of this event could be captured by GRACE satellite. However, no mass change from GLOFs is captured by GRACE so far because of the mass change of GLOFs are relatively small to be captured by GRACE. Here I investigate whether the mass change along the GLOF from Lago Greve is captured by GRACE.

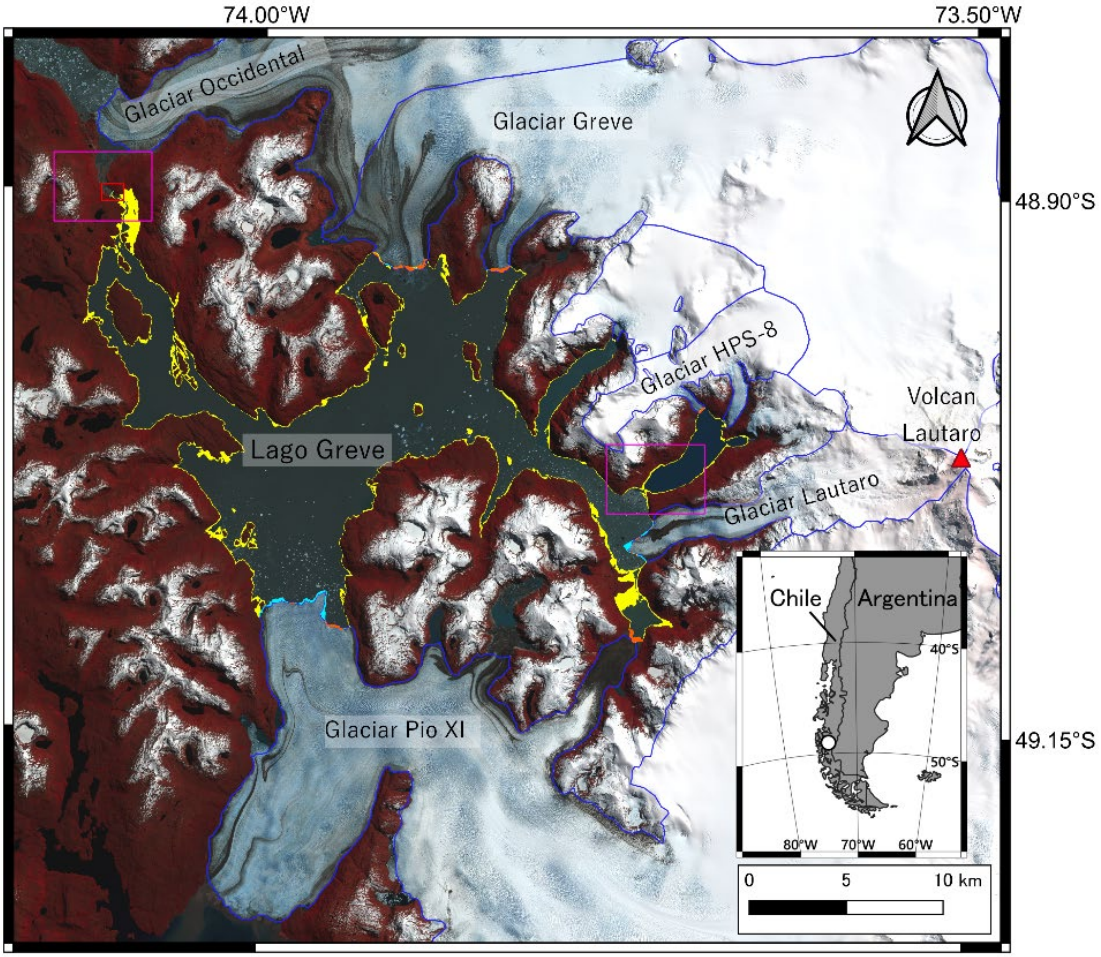

Figure 5.1. Area change of Lago Greve in 2020. Regions where the lake are decreased in 2020 are represented in yellow. Cyan and orange show the regions where the lake increased and decreased by retreat and advance of outlet glaciers, respectively.

5.2. Drainage event of Lago Greve

5.2.1. Rapid drainage event

The surface area of Lago Greve gradually enlarged from 2016 to 8 April 2020, resulting in areal increase of 3.1 ± 0.02 km^2 (Figure 5.2a). This change was mostly due to the retreat of glaciers terminating in the lake (2.5 ± 0.1 km^2). Sudden retreat of the shoreline was observed from the images on 8 April and 5 May 2020, which was followed by further retreat and lake area reduction of 14.5 ± 0.02 km^2 from 8 April to 29 July 2020. Water surface dropped by 12.3 ± 2.7 m from 8 to 29 April and by 18.3 ± 1.2 m from 8 April to 29 July, whereas change before the event was insignificant (±1.2 m) (Figure 5.2b). According to the SAR images, the onset of the drainage was between 9 and 19 April 2020 (Figure 5.3). After the drainage event, from 29 July to 1st November 2020, the lake area and water level were stable within the uncertainty ranges (Figures 5.2). The lake area on 1st November 2020 was 187.9 ± 0.02 km^2, indicating a 7.2% reduction since 8 April 2020. Water volume released from 8 April to 29 July 2020 was 3.7 ± 0.2 km^3 (3.7 ± 0.2 Gt), according to the changes in the lake area and water level. This is equivalent to 31 ± 8% of annual ice mass loss from the SPI observed in 2000–2015/16 (Malz et al., 2018) and 0.01 mm of sea level rise.

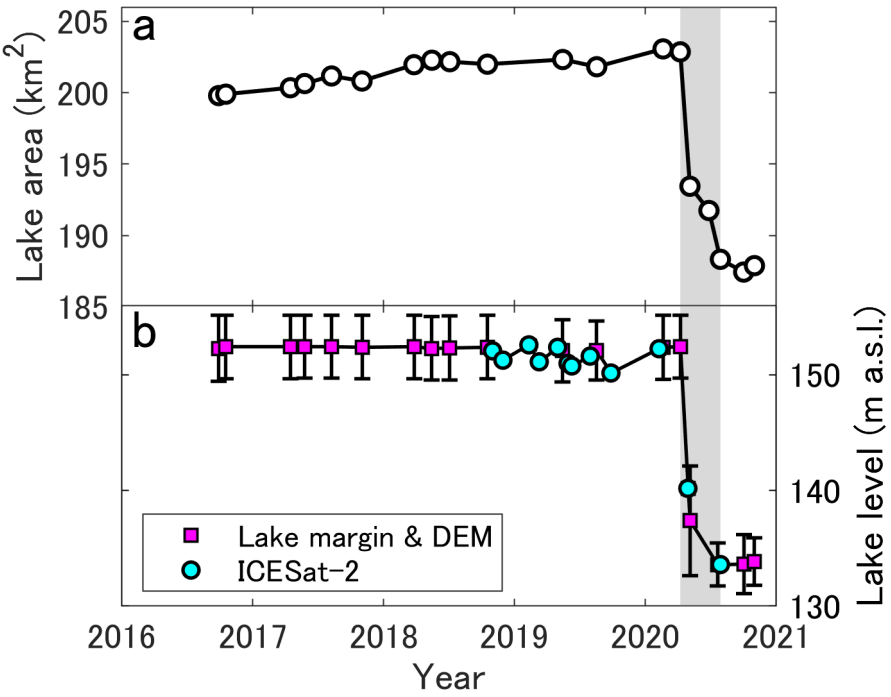

Figure 5.2. Changes in area and water level of Lago Greve in 2016–2021.

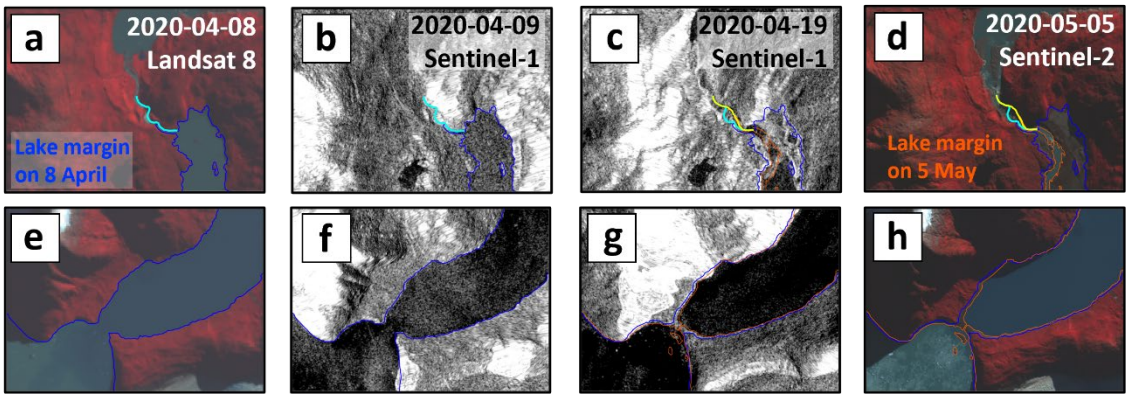

Figure 5.3. Satellite images showing initiation of the drainage event.

The magnitude of the lake outburst, in terms of the discharge volume, is among the largest reported for glacial lakes in Patagonia and other regions. Glaciar Perito Moreno in the SPI has repeatedly blocked a channel connecting Brazo Rico to Canal de los Témpanos (Stuefer et al., 2007; Lenzano et al., 2018; Pasquini and Deptris, 2011). Rupture of the ice dam caused the drainage of lakewater from Brazo Rico to Canal de los Témpanos. During the largest event occurred in 1954–1956 (Heinsheimer, 1958; Stuefer et al., 2007; Lenzano et al., 2018; Pasquini and Deptris, 2011), the lake level dropped by 26 m and 5.2 km^3 of water drained (Heinsheimer, 1958). Large GLOFs were reported also in the Northern Patagonia Icefield (NPI) (e.g., Dusssaillant et al., 2010; Aniya et al., 2020). The largest event in the NPI since the 20th century occurred in 2008 at Cachet Lake, a proglacial lake of Glaciar Colonia. The water volume drained during the event was estimated as 0.2 km^3 (Dusssaillant et al., 2010).

Outbursts of subglacial lakes in Iceland (jökulhlaup) are another example of large-scale glacial lake drainage. Outbursts from Grímsvötn, a subglacial lake beneath Vatonajökull, were estimated to be 4.5 and 0.6–1.2 km^3 for events occurring in the 1930s and 1980s, respectively (Gudmondsson et al., 1995). An ice-dammed lake formed by advance of Hubbard Glacier, Alaska, released 5.4 km^3 of water when the ice dam collapsed in 1986 (Mayo, 1989). In east Greenland, a glacier-dammed lake Catalina caused four outburst events between 1966 and 2016 (Grinsted et al., 2017). The outbursts were triggered by floatation of the ice dam, which lead to rapid water discharge of 2.6–3.4 Gt. The water volume drained from Lago Greve is comparable to those reported for the previously observed large GLOF events.

5.2.2. Change in the topography at outlet of the lake

Satellite images showed that the channel leading lakewater to the lake outlet shifted its flowline after the event. Before the event in February 2013, the northward water stream was deflected to west by a ~100 m long bedrock bump covered with vegetation at the top of the waterfall (Figures 5.4a and c). After the event (21 July 2020), the bump disappeared and the stream shifted northeastward by several hundred meters for a region extending 250 and 300 m up- and down-stream from the outlet, respectively (Figures 5.4b and d). Vegetation disappeared from the region bounded by the stream flowlines before and after the event, implying that the northern bank of the stream was eroded over the course of the flowline migration.

Comparison of the DEMs in February 2000 and July 2020 indicates significant change in the land surface elevation on the northern bank of the outlet stream (Figures 5.4e and f). Elevation dropped by more than 30 m in the region between the lake and the waterfall (highlighted in red in Figure 5.4a). Mean elevation change was −24.7 ± 5.6 m along the flowline of the stream before the event (Z–X' in Figure 5.4e) (Figure 5.4g) and −33.7 ± 5.6 m along the flowline after the event (Z'–X') (Figure 5.4h). Change in the topography near the waterfall was clearly observed by comparing the cross sections across the flowlines (Figure 5.4i). Before the event, the stream was running along the depression situated relatively south in the valley (Z in Figure 5.4i). Because the surface elevation on the northern bank of the stream dropped by ~20–30 m, the depression shifted to north by ~100 m and deepened by ~20 m (Z' in Figure 5.4i), which is approximately equal to the change in the lake surface elevation after the lake drainage.

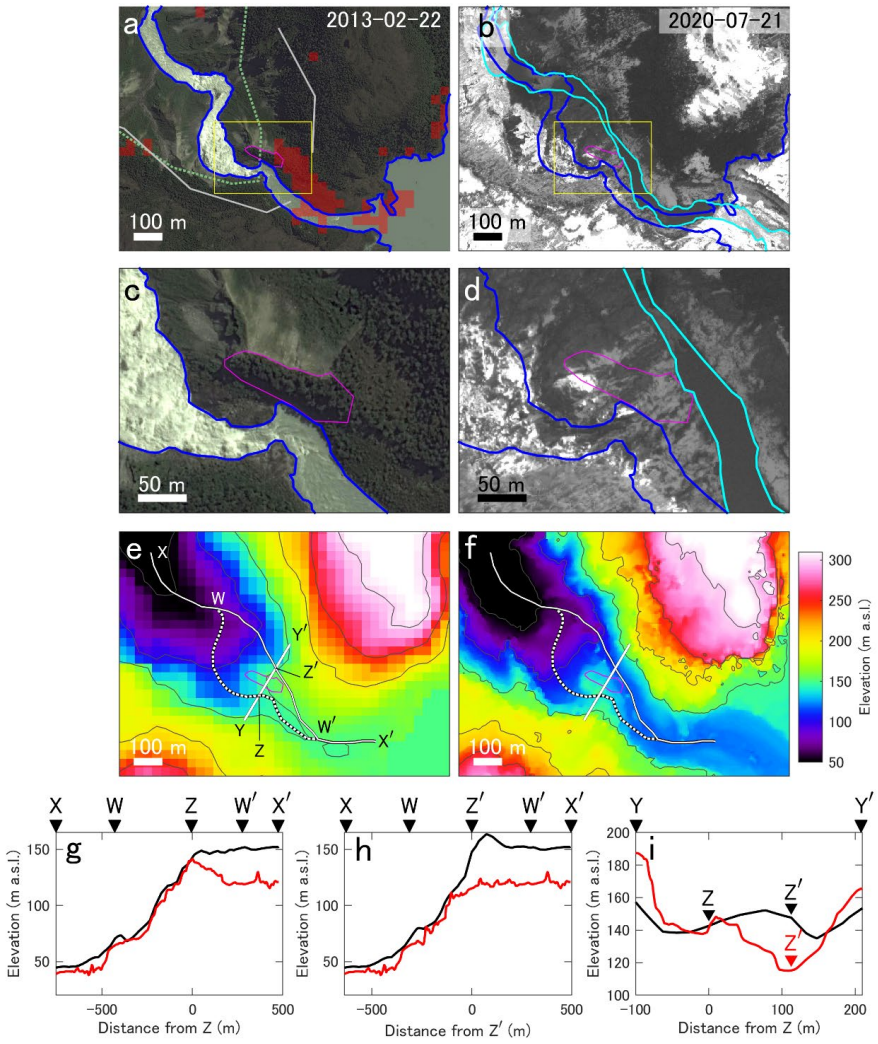

Figure 5.4. Surface elevation changes in the lake outlet region. Satellite images acquired (a) before (Google Earth on February 22, 2013) and (b) after the outburst event (World View-2 ©Maxar on July 21, 2021). Magenta curve in (a) indicates the location of the bump described in the text. Blue and cyan curves in (b) indicate side margins of the outlet stream before and after the event. Green dotted and gray solid lines in (a) indicate the frontal position of Glaciar Occidental during the Little Ice Age (Meier et al., 2018) and its moraine position (Davies et al., 2022), respectively. Regions highlighted in red in (a) are where surface elevation decreased by >30 m between 11–22 February 2000 and 21 July 2020. Yellow boxes in (a) and (b) show the regions enlarged in (c) and (d), respectively. Surface elevation near the outlet of Lago Greve based on (e) SRTM-DEM (February 2000) and (f) WV-DEM (21 July 2020). Dashed and solid curves indicate the flowlines of the stream before and after the event, respectively. (g) Surface elevation along the stream (g) before (X-Z-X' in e) and (h) after the event (X- Z'-X'), and (i) across the outlet region (Y-Y').

5.2.3. Gravity field

Total masses of mascons of land tiles averaged within 200, 300, and 400 km from the lake showed similar temporal patterns (Figure 5.5a). Seasonal variations, clear in the signal as winter positive and summer negative changes, can be attributed to snow accumulation and snow/ice melting. The negative trend over the entire period indicates the mass loss of the glaciers in the region (Chen et al., 2009; Li te al., 2019). The GRACE data deviate from the fitting curve significantly after 2020 (Figures 5.5b–d). Root mean square errors (RMSEs) from January 2020 to August 2021 (0.26–0.54 m w.e.) are substantially greater than those for the 2002–2019 period ($4.6–7.1\times10^{-2}$ m w.e.). The model underestimates the mass loss in this region, implying additional mass loss event there. The RMSEs after July 2020 can be minimized by assuming an additional mass reduction event which took place linearly from April to July 2020 (red curves in Figures 5.5b–d). The regression of the data suggested additional mass losses of -0.29 ± 0.03, -0.23 ± 0.02, and -0.17 ± 0.02 m w.e. for the regions within 200, 300, and 400 km, respectively.

Mascon tiles showing negative mass changes from March to August 2020 lie mostly within ~200 km from Lago Greve (Figure 5.5e). There the average seasonal changes from March to August in 2002–2019 are already removed from the results. The mass loss regions do not coincide with the Patagonia Icefields (regions within blue curves in Figure 5.5e) but are localized near the lake. Therefore, the observed mass loss signals are most likely due to the observed discharge of lakewater from Lago Greve in 2020.

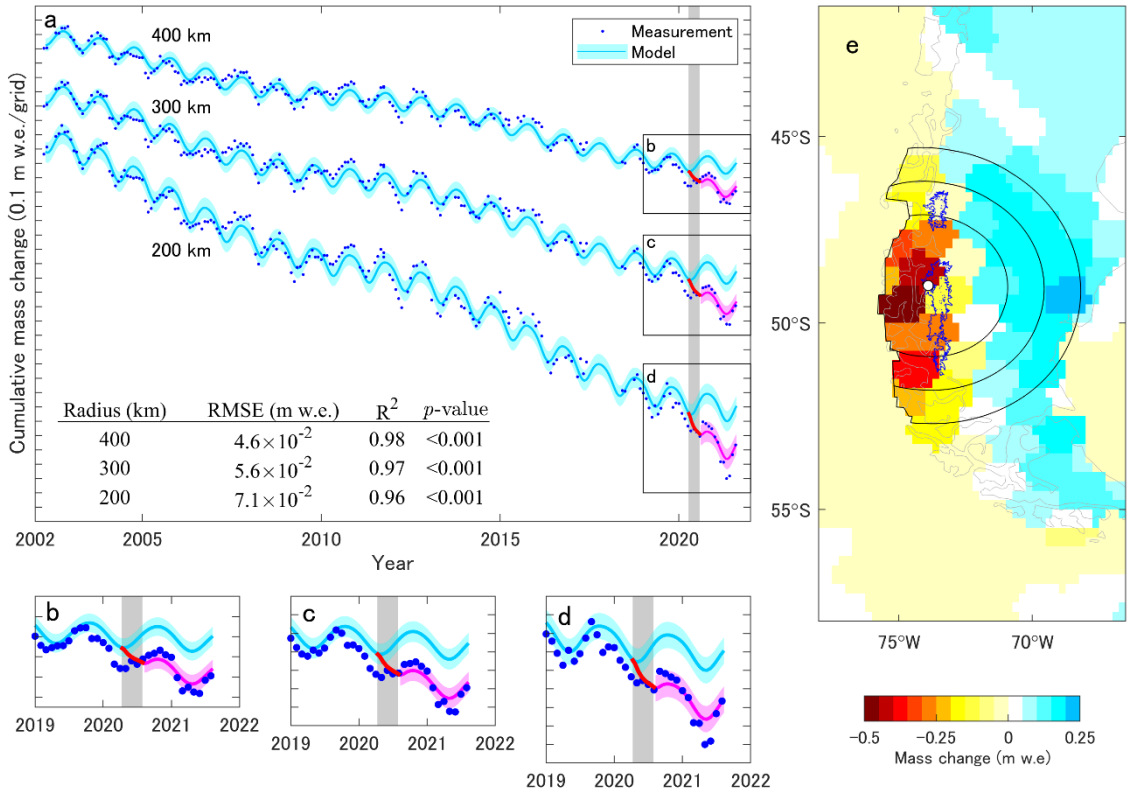

Figure 5.5. Mass changes over the study region. (a) Mass changes in the GRACE mascon solution summed over areas within 200, 300, and 400 km from the lake. Cyan curves are the best-fit time series assuming Equation 2. RMSEs of the model are shown by the shading around the curves. Red and magenta curves are results of the regression assuming an additional mass loss event that occurred at a constant rate from 8 April to 29 July 2020 (gray shaded band). RMSEs, correlation coefficients, p-values of the fitting are also shown. (b–d) shows the close-up view of the parts after 2019. (e) Distribution of mass changes from March to August 2020. Regions within blue curves indicate the Patagonia Icefields. The white dot indicates the location of Lago Greve. Solid curves indicate the regions within 200, 300, 400 km from the lake.

5.3. Changes in glacier variation after the drainage event

5.3.1. Ice-front position

From 2016 to 2018, the northern front of Glaciar Pío XI was relatively stable (Figure 5.6). The change in this period showed clear seasonal variation, summer retreat and winter advance. After the drainage event of Lago Greve, in April 2020, the seasonal change was not identified at this ice-front (Figures 5.6 and 5.7). The ice-front position retreated by 180 m in the period between December 2019 and August 2021. Thereafter, the ice-front showed advance of 150 m between August–December 2021 (Figure 5.7).

The shape of the ice-front changed before and after the drainage event. The ice-front was characterized by a horn-like shape located at ~1 km from the eastern side wall. This characteristic ice-front geometry was observed for the first time after reaching the relatively stable position in 2010. As the surrounding ice recedes, and the characteristic geometry of ice-front changed after April 2020, the shape disappeared in December 2021 (Figure 5.6).

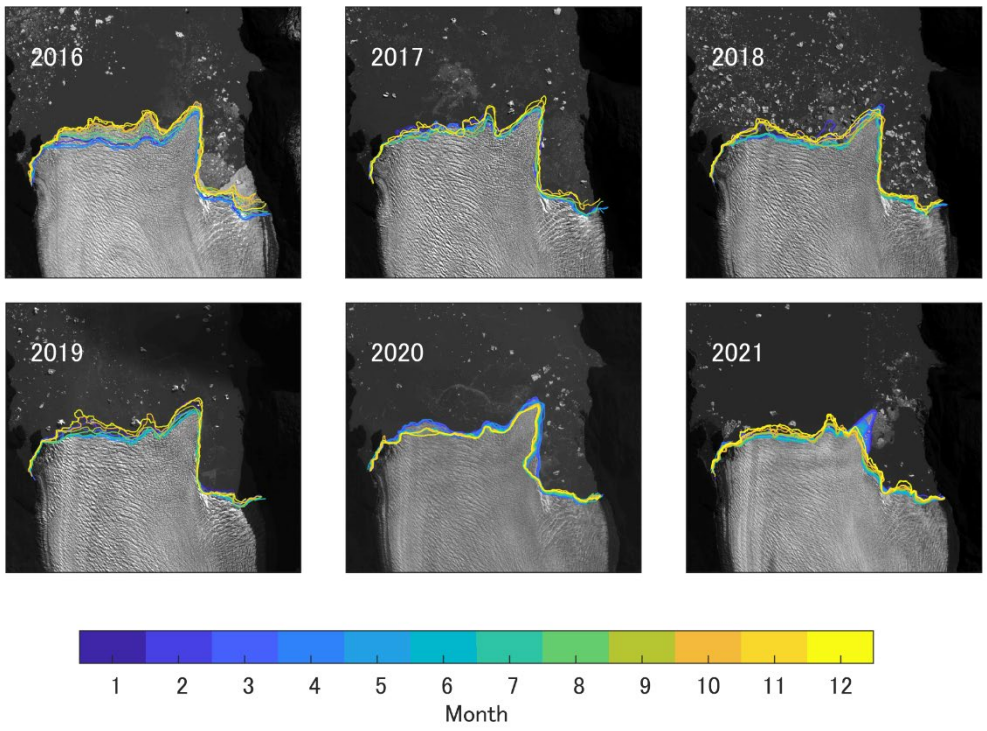

Figure 5.6. Ice-front position changes of the northern terminus of Glaciar Pío XI.

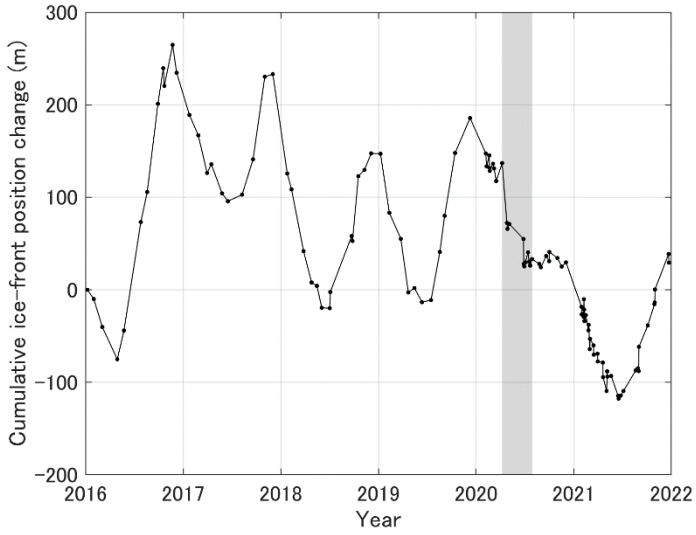

Figure 5.7. Cumulative ice-front position change of the northern terminus of Glaciar Pío XI. The reference position is on the January 2016.

5.3.2. Glacier flow velocity

The velocity of the northern terminus of Glaciar Pío XI showed seasonal oscillations in 2016–2019. A time series of data of 2017–2019 showed velocity increases in between end-winter and spring (June–September). Peak velocities were observed in July–November in 2016–2019. The mean velocities of the northern terminus were 796–967 m a^{-1} in 2016–2019 with a total mean during the entire period of 857 m a^{-1}. The amplitude of the seasonal velocity oscillation was large, as represented by the difference between the fastest and slowest velocity in 2019 was 2170 ± 60 m a^{-1} (Figure 5.8).

After the drainage event, the velocity of the northern terminus of Glaciar Pío XI drastically decreased. During the period between 28 March and 9 April 2020, just before the initiation of the drainage event, the velocity was 553 ± 71 m a^{-1}. After the drainage, the velocity in the period between 19 April and 1st May was 222 ± 72 m a^{-1}, indicating decrease in velocity by 60% in a month (Figure 5.9). The deceleration continued in several months, thereafter, the velocity reached minimum value of 46 ± 61 m a^{-1} in a period during 26 July and 7 August 2020. The mean velocity in 2020 after the event was 205 ± 115 m a^{-1}, which was 76% smaller than the mean velocity in 2016–2019. The mean velocity in January–July was 314 ± 64 m a^{-1} and glacier velocity had kept <500 m a^{-1} until July 2021. Thereafter, the glacier showed speed up until December 2021, the velocity reached 1250 m a^{-1}. Thus, the velocity showed an increasing trend in 2021, indicating that the seasonal oscillation observed in 2016–2019.

Spatial distribution of the glacier velocity indicates the primary flow path changed as “switching” before and after the drainage event of Lago Greve (Figure 5.10). Before the drainage event, in 2016–2019, the glacier flowed from upper part to the northern terminus through the branch with seasonal changes (Figure 5.10a–c). By March 2020, a month before the onset the drainage event, the flow direction was similar as in 2016–2019 (Figure 5.10d), and the velocity of the northern terminus in March 2020 was 583 ± 75 ma^{-1}. After the onset of the drainage event, gradual speed up was observed in

the southern terminus and abrupt speed down was observed in the northern terminus (Figure 5.10e–f).

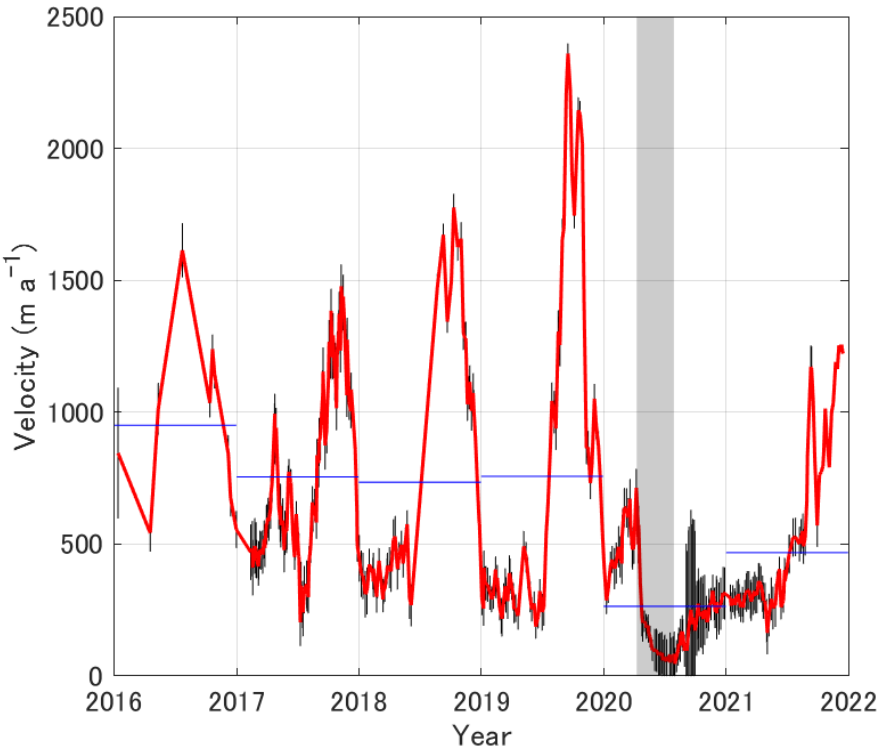

Figure 5.8. Velocity change of the northern terminus of Glaciar Pio XI in 2016–2021. Red and blue lines indicate velocity image pair velocity and annual mean values, respectively.

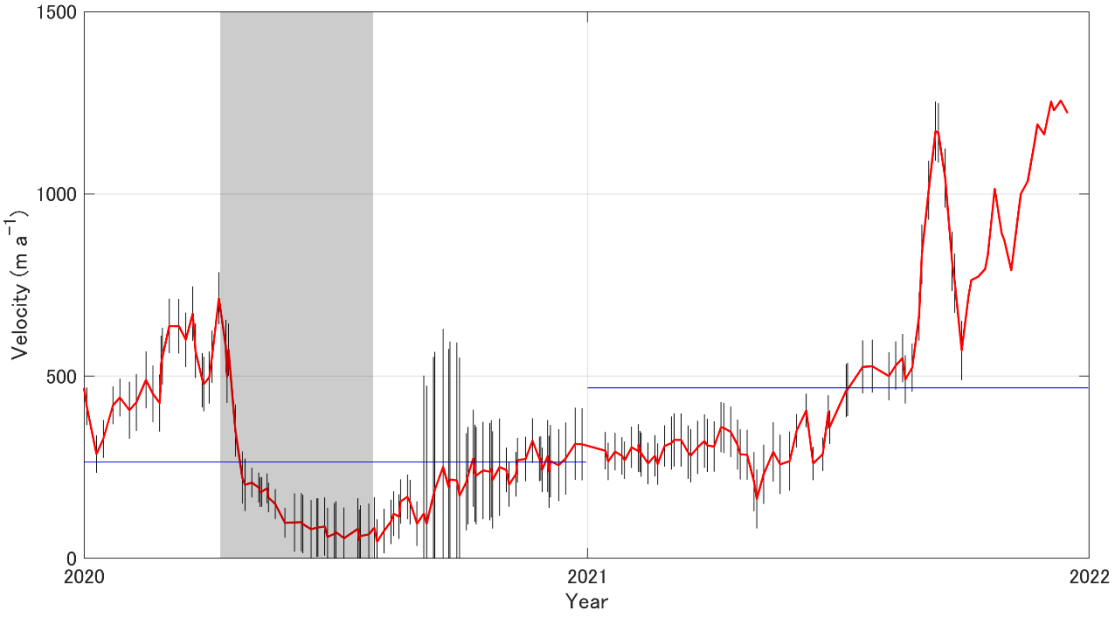

Figure 5.9. Velocity change of the northern terminus of Glaciar Pio XI in 2020–2021.

The series of change resulted in the primary flow path switching. Flow path switching is also observed by the time series of glacier velocity (Figure 5.11). Before the onset of the drainage event, changes in velocity of the northern terminus, southern terminus, and at the bifurcation area showed a similar oscillation. The largest velocity among the three points was observed at the bifurcation area throughout the study period, and velocity the northern terminus was larger than that of the southern terminus (Figure 5.11). After the drainage event, although velocity of the northern terminus dropped, the southern terminus and the bifurcating area did not show such abrupt change. Seasonal velocity variations of the northern terminus disappeared after the lake drainage. Although velocity of the southern terminus was still small than that at the bifurcation area, the velocity change of the southern terminus was similar to that of the bifurcating area, which is similar situation of observed before the drainage event.

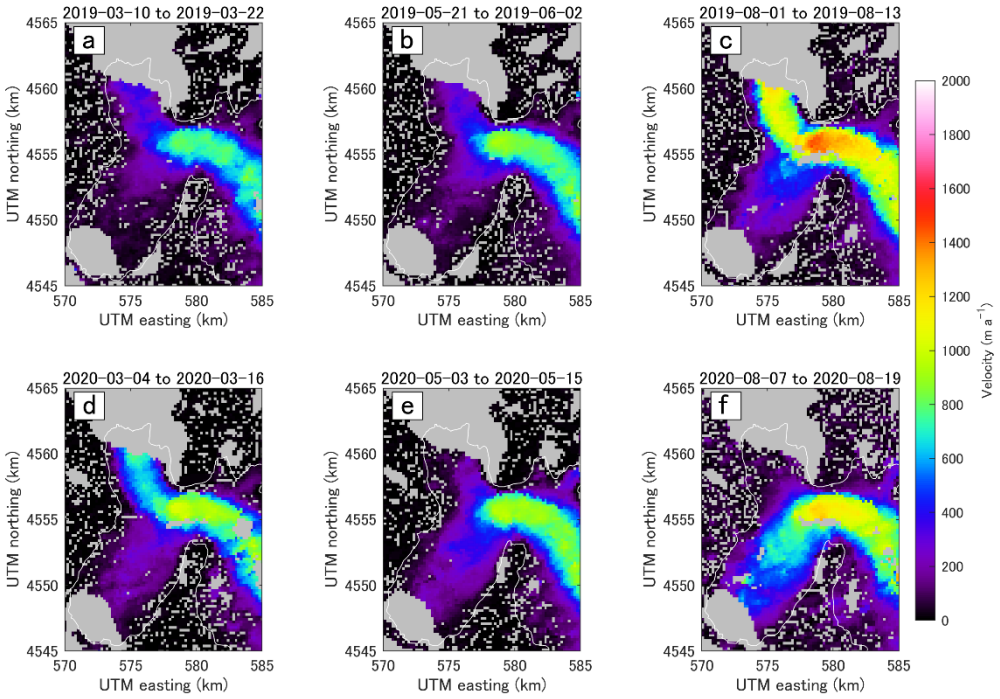

Figure 5.10. Changes in spatial distribution of glacier velocity.

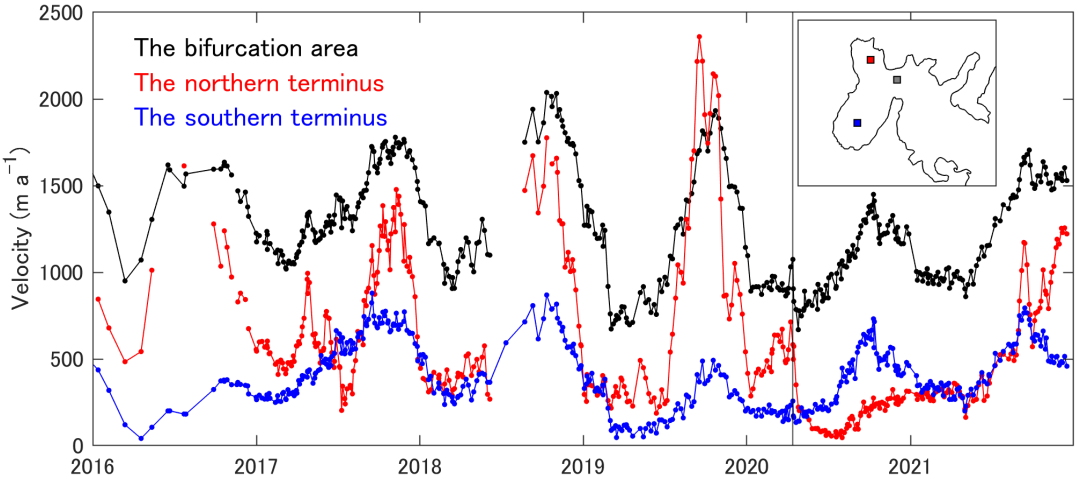

Figure 5.11. Timeseries of glacier velocity from the selected point. Locations of sampling points of the bifurcation area, the Northern and the Southern termini are shown in inset. Vertical line indicates 9 April 2020, the onset of the drainage period.

5.3.3. Surface elevation change

Surface elevation of terminus region of Glaciar Pío XI showed thinning during the period between August 2019 and March 2021 (Figure 5.12). Surface elevation was lowered by 4.7 ± 0.2 m and the surface elevation change rate was −3.0 ± 0.1 m a^{-1} as a mean over the study area. However, the spatial pattern of the surface elevation change was not uniform over the terminus region. The most rapid thinning was observed near the northern terminus (area (1) in Figure 5.12), where the elevation change was −16.3 ± 0.4 m and the rate was −10.6 ± 0.3 m a^{-1}. On the other hands, at a region near the southern terminus (area (2) in Figure 5.12), the thinning was relatively small at −4.9 ± 0.2 m and the rate was −3.2 ± 0.2 m a^{-1}. In addition to the changes near the glacier fronts, the main trunk of the glacier (area (3) in Figure 5.12) showed surface uplift by 9.1 ± 0.5 m (+5.9 ± 0.3 m a^{-1}).

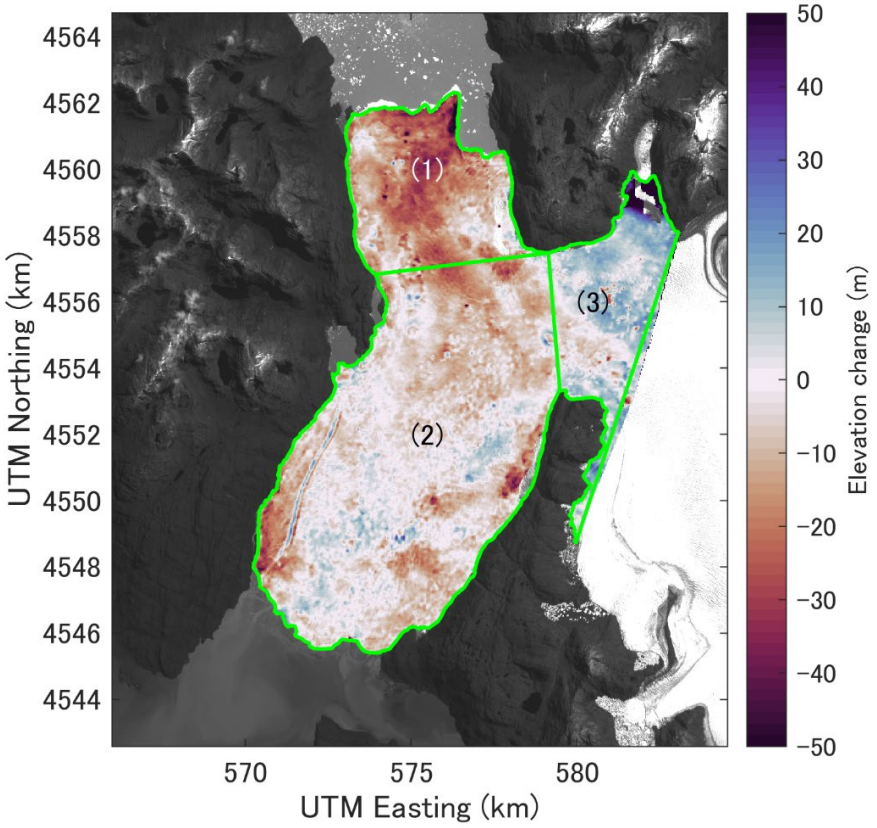

Figure 5.12. Surface elevation change of terminus region of Glaciar Pío XI, between 15/16 August 2019 and 2 March 2021.

5.4. Summary

In this chapter, I reported outburst of Lago Greve in Patagonia, the fourth largest glacial lakes in the world. Satellite data showed rapid drainage of the lake from April to July 2020, resulting in decrease in the lake area by 14.5 ± 0.02 km^2 and drop in the water level by 18.3 ± 1.2 m. Water volume released from the lake was 3.7 ± 0.2 km^3 (3.7 ± 0.2 Gt), which is one of the greatest among ever reported glacial lake outburst events. Satellite images and DEMs indicated that the outburst was triggered by the collapse of a bump near the lake outlet and subsequent change in the flow path of the outlet stream. The event affected the gravity field, which was observable by the GRACE mascon solution.

After the drainage event, characteristics changes are observed at the northern terminus of Glaciar Pío XI. First, the terminus showed rapid retreat (−300 m) and thinning after the drainage event. Glacier velocity of the northern terminus dropped by 60% after the drainage event within two weeks after the onset, subsequent slowdown was resulted in 92% reduction in the velocity relative to the velocity before the drainage event. Further, the seasonal change in velocity of the terminus observed before the event was not confirmed from the timeseries of the velocity. Furthermore, the spatial distribution of glacier velocity indicated changes in the primary flow direction from towards the northern terminus to towards the southern terminus.

Chapter 6
Discussion

6.1. Ice-front advance at the southern terminus in 2000–2018

6.1.1. Influence of sediment deposition

A close investigation of the satellite images revealed the emergence of sedimentary mound above ocean surface near the ice-front of the southern terminus since 2011 (Figure 6.1). Sediment deposition near the southern front was reported in previous studies. In 1992, during a period of advance, proglacial delta near the margin was pushed by the ice-front forming sediment wedges above sea level (Warren and Rivera, 1994). Only small calving occurred at the central 1500 m of the terminus, and the rest of the ice-front was in contact with sediments. Bathymetry of Eyre Fjord surveyed in 2003–2008 shows relatively flat and shallow (20–60 m) sea floor near the glacier front (Dowdeswell and Vásquez, 2013). Near the present ice-front position, a ~30 m-high depositional ridge was formed by sediment-laden water discharge from the eastern glacier margin. Satellite image from 2018 indicates that the ice-front position is affected by the sea-floor ridge (Figure 6.1b). These observations confirm that sediment deposition is as a key process in the frontal dynamics of Glaciar Pío XI.

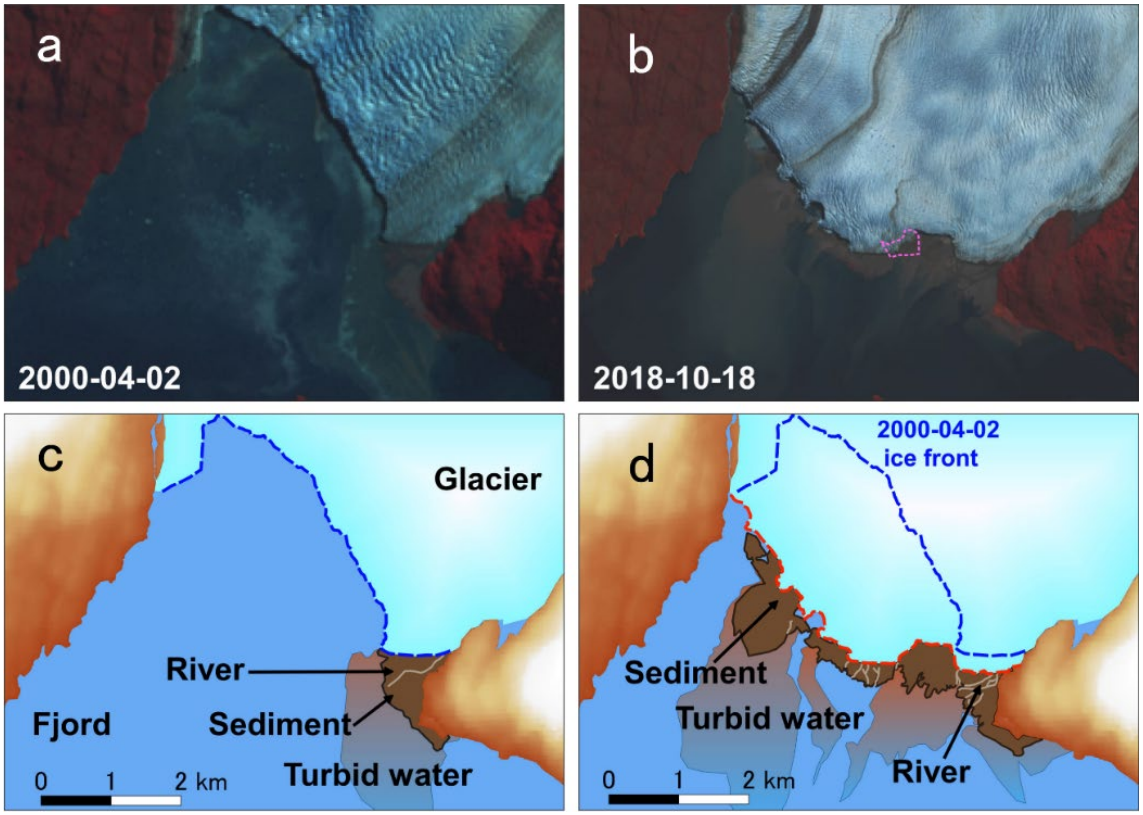

Figure 6.1. Satellite image and schematic diagram showing the southern terminus. The boundaries between sedimentary mound and fjord water in (c) and (d) were illustrated based on the Normalized Difference Water Index (NDWI) (McFeeters, 1996). NDWI < 0.3 was taken as a condition to distinguish sediment from water. The threshold was determined by visual inspection of the sedimentary delta observed on the image on 2 April 2000. This threshold is within a range reported in previous studies (e.g., McFeeters, 2013). The dashed line near the ice-front in (b) shows the location of the sea-floor ridge observed in the bathymetry presented by Dowdeswell and Vásquez (2013).

The formation of the sedimentary mounds implies its significant impact on the frontal ablation processes and glacier dynamics. The separation of the ice-front from fjord water results in reduction in ablation due to submarine melting. The glacier front is protected from fjord circulation and stabilized by the sediment deposition, so that subaqueous melting and calving flux decreases. Satellite images show frequent calving from the heavily crevassed ice-front before 2011, whereas no iceberg was observed in the fjord after the emergence of the sedimentary mound (Figures 6.1a and b, 4.6). Further, ice

flow is expected to slow down because back pressure from the sediments increases after the ice overrode the shoal. This hypothesis is supported by ice speed data (Chapter 4) and previous studies of glacier velocities. In addition, Minowa et al. (2021) reported the rapid reduction of frontal ablation at the terminus in 2000–2010.

The reduction in the frontal ablation, a compressive flow regime due to deceleration and ice overriding a moraine are all favorable conditions for ice-front advance, thickening and surface uplift. Therefore, we assume that the recent advance and thickening of Glaciar Pío XI is greatly affected by sediment deposition in front of the southern terminus, a similar situation as reported at Taku Glacier in Alaska (Motyka and Echelmeyer, 2003; Kuriger et al., 2006; Motyka et al., 2006; Truffer et al., 2009). Presumably, sediment deposition played a critical role also in the long-term fluctuations of Glaciar Pío XI as demonstrated by numerical modeling of tidewater glacier frontal variations (Brinkerhoff et al., 2017).

Bathymetry surveyed in 2003–2008 showed that the fjord was shallower than 50 m near the southern terminus (Dowdeswell and Vásquez, 2013). Most likely, the glacier dynamics and frontal ablation were already affected by the shoal before the sedimentary mound emerged above the ocean surface in 2011. The mound formed near the glacier front was not a stable feature. Satellite images indicate occasional disappearance or reduction in the area of the sedimentary mound in a relatively cold season, e.g., August 2017, May 2019 and July 2020 (Figure 6.3). A likely interpretation of the seasonal evolution is a balance between sediment discharge from the glacier and its removal by fjord circulation. The extent of the sediment deposits reduced when sediment laden meltwater discharge decreased in winter.

During the recent advance trend, a 1-year-long retreat phase was observed from April 2016 to April 2017, in which the ice-front retreated by 180 m. Satellite images indicate the massive retreat was occurred a region where the ice-front was not contact to

the sedimental mound (e.g., western side of the terminus). Further, large retreats were observed even at a region where sediment mound was located near the terminus (yellow arrows in Figure 6.2). At these regions, certain distances were existing between ice-front and the mound, which situation permits the ocean water to melt ice and the ice-front to cause calving. As a consequence of the imbalance of ice there, the region showed relatively large retreat. However, frontal ablation due to the opening between the glacier and mound is not sufficient to cause large retreat. In contrast to the retreat phase, ice-front covered by mound kept stable during the same period (magenta arrow in Figure 6.2). These contrasts emphasize the significance of sediment deposition to the migration of ice-front position even in short time period.

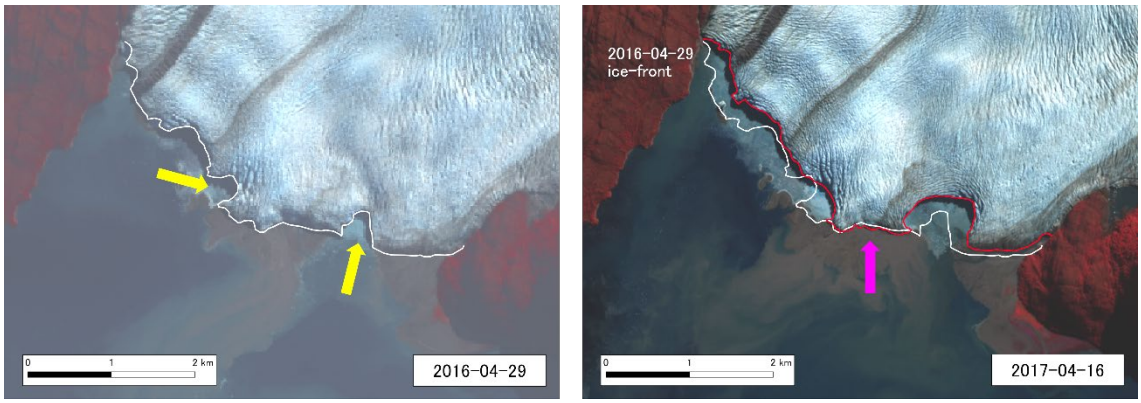

Figure 6.2 Sediment deposition and glacier terminus change in a short time scale.

6.1.2. Climate effect on the advance

Previous studies reported an increasing trend in precipitation over the last few decades in Patagonia (Schaefer et al., 2015), and a correlation was suggested between the spatial pattern of snow fall increase and the locations of relatively stable glaciers (Bravo et al., 2019). To investigate a possible influence of climatic trend on the observed glacier change, we analyzed ERA-5 reanalysis data (Hersbach and Dee, 2016). ERA-5 reanalysis data is the successor of ERA-Interim, which has been widely applied for climate analysis and modeling. Previous studies reported an improvement in the performance of the ERA-5 air temperature and precipitation datasets (Albergel et al., 2018; Tetzner et al., 2019). Air temperature and precipitation from grid cells covering the glacier (49.0–49.5°S, 73.5–74.0°W) were averaged for this purpose. Summer mean temperature (December–February) showed a slight warming trend during 1979–2019 at a rate of + 0.09°C decade^{-1} (p = 0.34). This trend is due to a significant temperature increase after 2000 (+0.50°C decade^{-1} in 2000–2019, p = 0.02) (Figure 6.3a). Annual mean air temperature also showed a similar positive trend during the same period (0.59 °C decade^{-1}, p < 0.01).
Therefore, the advancing trend of Glaciar Pío XI since 2000 cannot be explained by the temperature change.

Annual precipitation increased after 2000 (+0.36 m a^{-1} decade^{-1} in 2000–2019, p = 0.09) in contrast to a slightly negative trend in the previous period (−0.15 m a^{-1} decade^{-1} in 1979–2000, p = 0.39) (Figure 6.3b). Snow accumulation in the relatively large accumulation area has been pointed out as a key process driving the extraordinary behavior of Glaciar Pío XI (Rivera et al., 1997b; Rivera and Casassa, 1999; Rivera, 2018). The gradual increase in precipitation after 2000, which is consistent with previous studies (Schaefer et al., 2015; Bravo et al., 2019), implies greater accumulation in the high elevation area. However, the precipitation trend is not a likely reason of the rapid change near the glacier front since 2000. Influence of increased accumulation propagates down-glacier in a longer time scale, which is not able to explain the extraordinary rapid thickening near the southern front followed by pervasive thickening in the upper reaches.

It is also clear that frontal variations since 1980 show correlation neither with temperature nor with precipitation (Figure 6.3c). It should be noted that snow accumulation in the upper reaches of Glaciar Pío XI is large and variable (Schwikowski et al., 2013), which is difficult to reproduce by reanalysis data. Precipitation and snow accumulation in Patagonia are complex processes as demonstrated by a recent study on moisture transport to the region (Sauter, 2020). Considering the large magnitude of the recent glacier change, however, a noticeable indication is expected in the climate data if the change was driven by surface mass balance. Therefore, we assume the reduction in the frontal ablation and ice speed as the primary control of the glacier change in 2000, whereas snow accumulation in the relatively large accumulation area affects the longer-term advancing trend of Glaciar Pío XI.

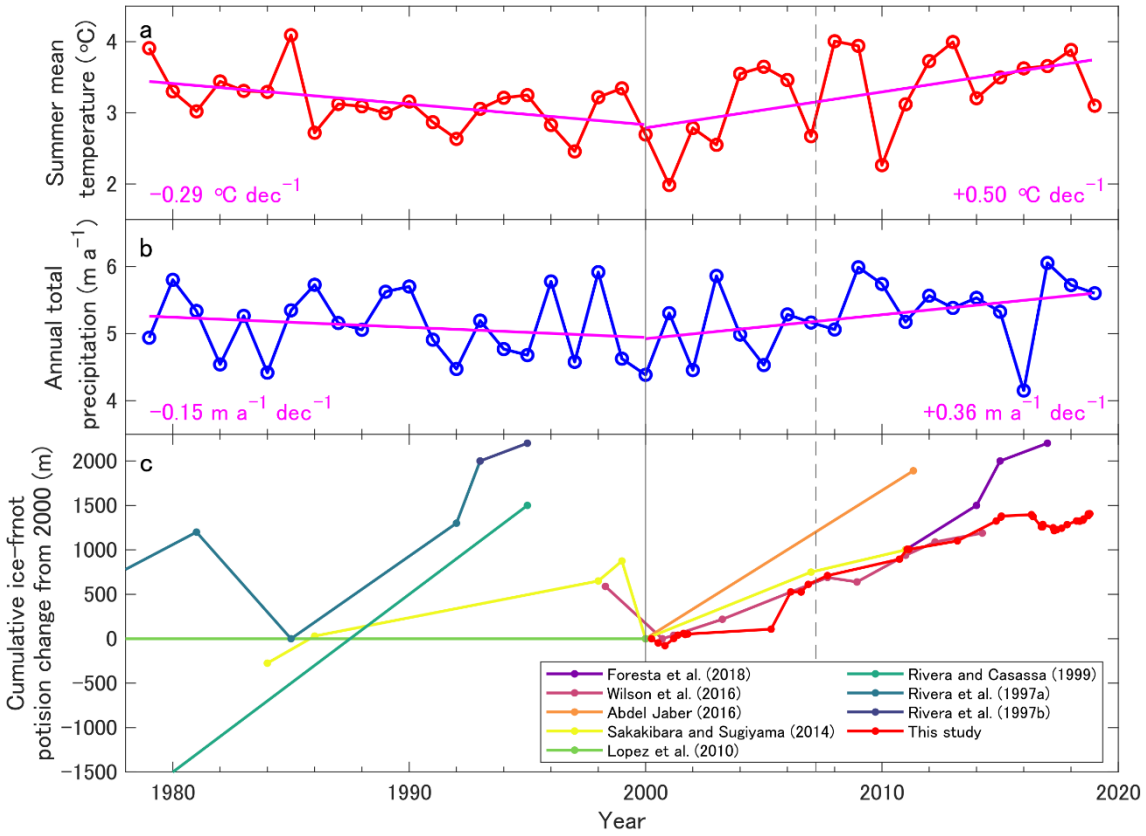

Figure 6.3. Climate conditions derived by ERA5 reanalysis data and ice front position change of the southern terminus. Summer mean temperature (a) and annual precipitation, and ice-front position changes derived by previous studies are shown.

6.1.3. Spatiotemporal variations in the elevation change

The glacier thickened over the entire region of the ablation area (Figure 4.3c), and advancing trends were observed at the outlet glaciers and ice margins as well (Figures 4.2). Although the generally thickening and advancing trends are consistent over the study area, the magnitude of the changes was spatially inhomogeneous. Here, we analyze the spatial variations in the surface elevation change to understand the process driving the glacier advance and thickening revealed in this study.

The rate of the elevation change generally increased toward the lower elevation area (Figure 6.4). Mean elevation changes below and above 400 m a.s.l. were 3.8 ± 0.3 and 0.3 ± 0.2 m a^{-1} during Period 1 (Figure 6.4a) and 3.3 ± 0.4 and 1.9 ± 0.3 m a^{-1} during Period 2 (Figure 6.4b). Elevation increased in the upper reaches particularly in the later period, which is inconsistent with the hypothesis of down-glacier mass transfer due to surge before 2000. During Period 1, extraordinary rapid uplift was observed near the southern front and Sub2 front (Figures 4.3b and 6.4a). The mean rates in these regions reached 20 m a^{-1}, resulting in >100 m ice surface uplift over the seven-year period. Changes were more uniformly distributed during Period 2 (Figures 4.3c and 6.4b). Acceleration in the uplift rates is evident over the entire elevation range, except for the southern terminus, Sub2 and Sub4 ice tongue regions (Figure 4.3d). Notable uplift was observed at the northern terminus and Sub3 ice tongue, as well as over the main trunk of the glacier (Figure 6.4b). Although the rates were smaller than during Period 1, the southern terminus, Sub2 and Sub4 ice tongues still showed positive elevation change during Period 2.

The rapid uplift near the southern terminus during Period 1 can be explained by the sediment deposition described in the previous subsection. We assume that the elevation increase at a rate greater than 10 m a^{-1} was due to vertical straining associated with longitudinally compressive ice flow. The elevation change was possibly enhanced by thickening of the subglacial sediment layer. Near the southern and northern termini,

water depth was significantly shallower in Eyre Fjord (~20 m) than in Lago Greve (~150 m) (Warren and Rivera, 1994; Dowdeswell and Vásquez, 2013). The southern terminus was influenced more by sediment deposition because of the shallow depth of the fjord. We speculate that the extraordinary rapid uplift at Sub2 ice tongue during Period 1 was a result of similar sediment deposition. The northern terminus showed a clear phase shift from slight thickening (0.4 ± 0.7 m a^{-1}) and retreat (–23 m a^{-1}) during Period 1 to more rapid thickening (3.8 ± 0.7 m a^{-1}) and advance (84 m a^{-1}) during Period 2.

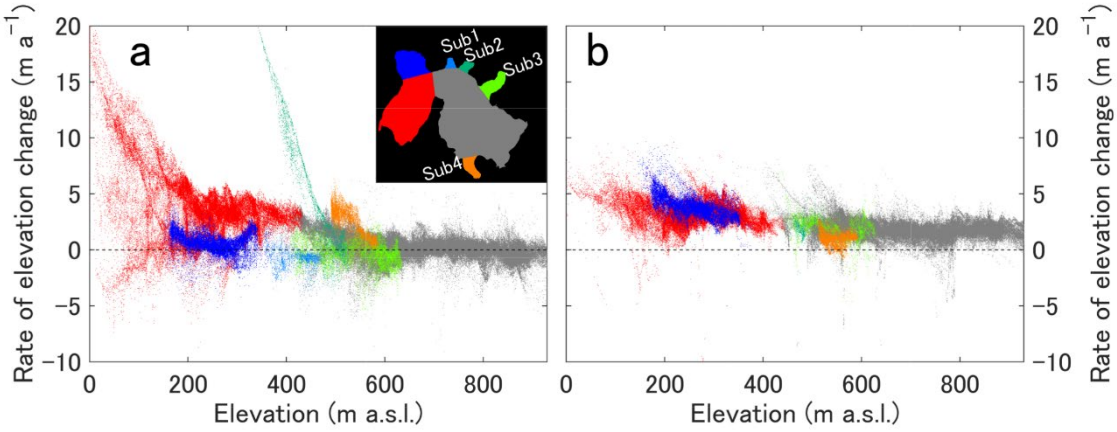

Figure 6.4. Scatter plot showing elevation change rate in different locations in (a)2000–2007 and (b)2007–2017/18.

6.1.4. Implications for long-term advance of Glaciar Pío XI

Glaciar Pío XI advanced by >10 km since 1945, and the mechanism of the glacier advance has been discussed by previous studies. Foregoing discussion demonstrated that sediment deposition played a significant role for the advance in the period of 2000–2018. Considering the sedimentary mound emerged above fjord sea surface in 2011 and the depth of the fjord near the southern terminus is reported to be 20–50 m in 2003–2008, the sedimentary mound had been formed before 2011, and affected the frontal ablation as discussed above (Section 6.1.1). The climate record suggested that the increase in precipitation in the study region as a possible driver of the longer-scale glacier change.

The southern terminus was in surge phase in 1997–2000 (Wilson et al., 2016), in which velocity as >2000 m a^{-1}. Furthermore, another possible surge phase was suggested before 1981 (Wilson et al., 2016). During these periods, the subglacial sediment transport was expected to be massive, because faster flowing ice erodes subglacial bedform more rapid (Herman et al., 2015). The fjord was shallow presumably because of the large sediment transport due to the past surge activities, and the topological settings could have been permitted the sediment to accumulate enough to affect glacier dynamics. Furthermore, sediment transport increases as a non-linear function of basal sliding speed (Brinkerhoff et al., 2017; Delaney and Adhikari, 2020). Definitive mechanism is still unknown because sediment deposition is affected by its accumulation and removal rates as well as the basal topography of the fjord. Moreover, the southern terminus decelerated during this period, affecting the ice flow regime in the upper reaches. After 2010, the northern terminus and the main trunk of the glacier began thickening as a consequence of the ice dynamics change propagated up-glacier from the terminus region. The behavior of Glaciar Pío XI is exceptional in the SPI, thus it cannot be explained by the effect of the regional climate and the sediment deposition is assumed as the key process of the glacier advance.

Sedimentary mound covered ~80% of the ice-front margin of the southern terminus in October 2018, the sediment area gradually expanded afterwards. The southern terminus had advanced after the formation of the sediment mound. In February 2020, the mound expanded to cover all along the ice-front (Figure 6.5a). Thereafter, even after the coverage reached almost all the ice-front, the terminus continued to advance by November 2021 (Figure 6.5b). This behavior implies that Glaciar Pío XI is in the slow advancing phase of tidewater glacier cycle (Amundson, 2016). Sediment deposition is considered as the key process of the advancing phase of the tidewater glacier cycle (Brinkerhoff et al., 2017; Zechmann et al., 2020). During the advance of Taku Glacier in Alaska since 1950s, the sediment covered the glacier terminus and restricted calving (Kuriger et al., 2006; Motyka et al., 2006). Assuming that Glaciar Pío XI is in the advancing phase of tidewater glacier cycle, the advance will continue until the glacier reaches a new steady state.

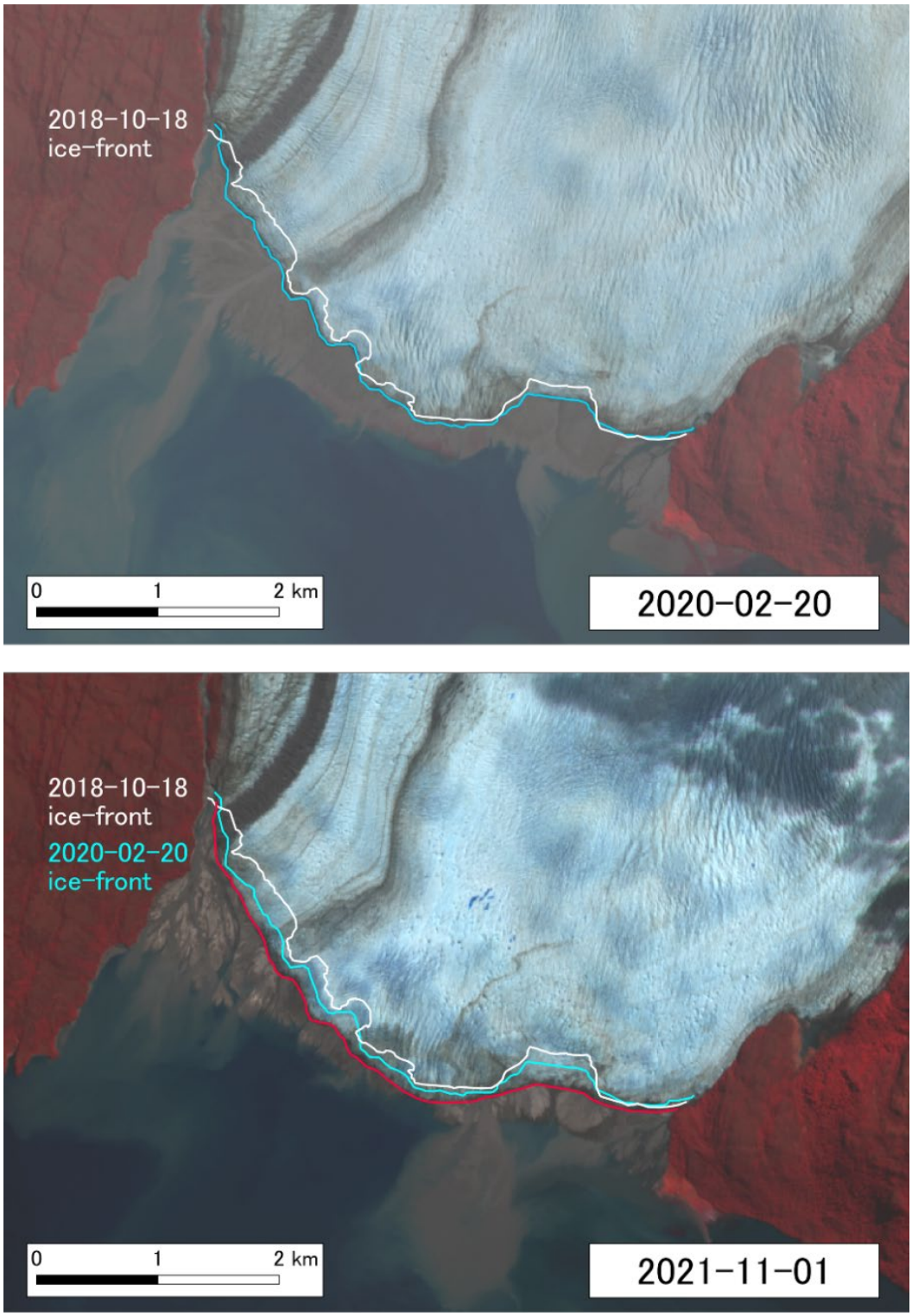

Figure 6.5. Ice-front advance after covered by sedimentary mound.

6.2. Changes in glacier flow direction

Ice speed data show acceleration of the northern terminus during 2000–2016, while the southern terminus decelerated during the same period (Figure 6.1). These observations indicated that the primary flow path at the bifurcating area switched from the south to the north. We attribute the thickening in the northern terminus during Period 2 to the increase in ice flux into the region. We also hypothesize that the deceleration in the southern terminus region affected the flow regime in the upper reaches and caused the thickening in the main trunk of the glacier during Period 2. Longitudinal flow regime became less extensive (i.e., vertical strain rate became less compressive) in the region, which resulted in accumulation of ice after 2010. Such a change in the flow regime is clearly observable in Figure 6.1e (>10 km from the front) as well as those reported by Wilson et al. (2016) and Abdel Jaber et al. (2019).

The primary flow path "switching" was also observed before and after the drainage event of Lago Greve (Chapter 5). In this case, the northern terminus decelerated by 60% after the onset of the drainage event and the primary flow direction changed to the southern terminus. Although the flow direction switched in 2020 to the other way of the observation in 2000–2016, these changes in the flow regime were driven by a common mechanism. Here, the change in flow direction is discussed based on the glacier deceleration of the northern terminus after the drainage event.

6.2.1. Deceleration of the northern terminus in 2020

Glacier surface velocity is a sum of the basal slip, internal deformation of ice, and deformation of till. At the terminus region of calving glacier in Patagonia, most of glacier speed is explained by basal slip (Sugiyama et al., 2011; Mouginot et al., 2015). Basal speed u_b is commonly formulated by

$$u_b = k \frac{{\tau_b}^p}{(P_i - P_w)^q} \tag{6.1}$$

where τ_b, P_i, P_w are basal shear stress, overburden pressure of ice at the base, and basal

water pressure, respectively. k, p, q are parameters. Here, τ_b, P_i and P_w are given by

$$\tau_b = f' \rho_i g H \sin \alpha \tag{6.2}$$

$$P_i = \rho_i g H \tag{6.3}$$

$$P_w = \rho_w g H_w \tag{6.4}$$

where f', ρ_i, ρ_w, g, H, H_w, and α are a correction factor to the driving stress, density of ice, density of water, gravitational acceleration, thickness of ice, hydraulic head of the bed, and surface slope of the glacier (Cuffey and Paterson, 2010). Among the variables controlling the basal speed, all except H_w hardly change in a short timescale (e.g., within a month). Therefore, the deceleration observed at the northern terminus after the onset of the drainage event can be assumed due to a drop in the hydraulic head of the base.

During the drainage event, lake level of Lago Greve dropped by 18.3 ± 1.2 m (Chapter 5), which is equivalent to a change in water pressure of −0.18 MPa. The mean thickness of the northern terminus along the central flow line was estimated to be 524 m and 390 m, by Millan et al. (2022) and Farinotti et al. (2019), respectively. Assuming the change in hydraulic head of the bed to be the same amount of the pressure reduction due to the lake level change, the change in subglacial water pressure is equivalent to 3–15% of the ice overburden pressure. The 3–15% of the water pressure reduction should significantly affect the glacier velocity and might be enough to cause rapid speed decrease there. Indeed, a 4–6% change in hydraulic head caused 37% change of glacier speed under a situation close to overburden pressure (95% as mean of the study period) in Patagonia (Sugiyama et al., 2011). Therefore, subglacial hydraulic head decreased after the drainage event had a potential to have caused the glacier deceleration.

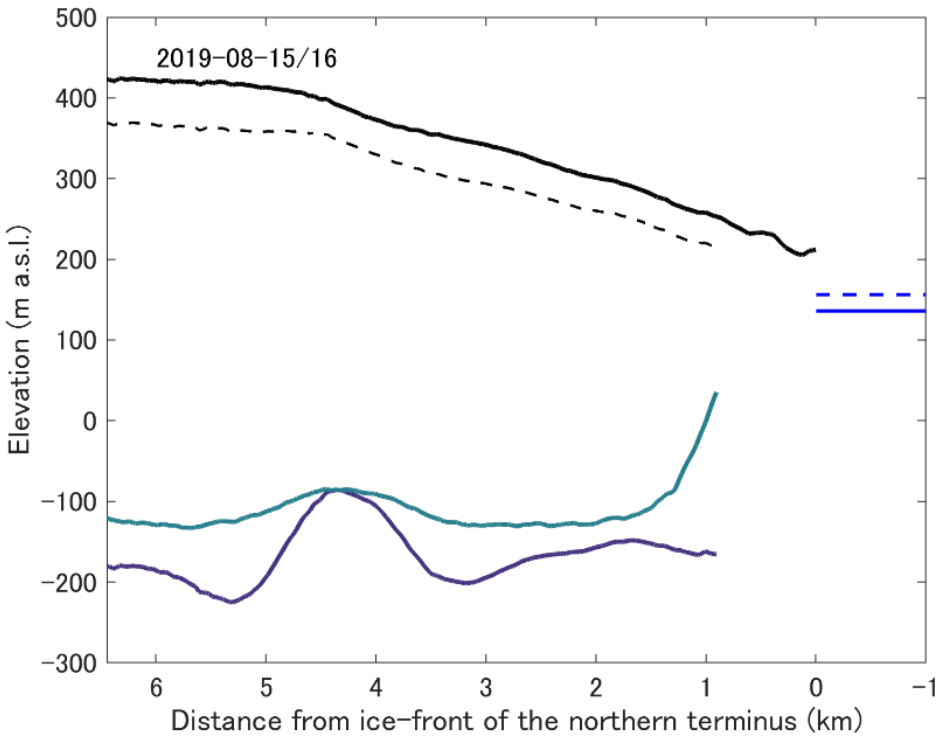

Figure 6.6 Glacier elevation and subglacial topography along the center line of the northern terminus. Black solid line indicates glacier surface elevation on 15–16 August 2019. Blue dashed and solid lines indicate water level of Lago Greve before and after the drainage event in 2020, respectively. Green and purple lines indicate subglacial elevation by Farinotti et al. (2019) and Millan et al. (2022), respectively. Black dashed line indicates overburden pressure level inferred from surface elevation and subglacial elevation by Millan et al. (2022).

Very large velocity variations observed before the drainage event evinces that the glacier dynamics was sensitive to small perturbations in basal water pressure. The northern terminus before the event showed a seasonal change with large amplitude of >500 m a^{-1} (Figure 5.8). For example, the difference between the fastest and slowest velocities in 2019 was 2170 ± 60 m a^{-1}. Such a large amplitude strongly suggests that the basal water pressure was close to the ice overburden pressure, thus changes in pressure caused significant basal speed variations.

Surface elevation change in 2019–2021 showed rapid thinning at the northern terminus (16.3 ± 0.4 m in 1.6 years, Figure 5.12). The velocity of the entire of the northern terminus decreased and the flow direction changed from toward the northern terminus to toward the southern terminus after the event. Therefore, I assumed the thinning to the decrease in ice flux into a region between the bifurcating area and the ice-front of the northern terminus. Further, glacier thinning induces decrease in the overburden pressure of ice, hence, the glacier flow after the thinning become accelerated even the same hydraulic head situation. Indeed, from August 2020 to August 2021, the northern terminus showed gradual speed up (46 ± 61 m a^{-1} to 523 ± 66 m a^{-1}, Figure 5.8 and 5.9). The change in hydraulic head due to the thinning (16.3 ± 0.4 m) was not enough to lead flotation if the change in hydraulic head was equal to the change in lake level, and therefore, the mechanism of the acceleration remains unclear. Nevertheless, thinning after the drainage event might be larger than observed value because the period of surface elevation change measurement included the period before the onset of the drainage event. Therefore, I attributed the thinning to changes in glacier velocity and ice flux.

Although the changes in flow direction was to the other directions in case 2000–2016 and 2020, both “switching” were probably caused by a common mechanism. A common characteristic is glacier flow reduction in response to the events occurred in the terminus regions. In the case in 2000–2016, glacier flow at the southern terminus was suppressed by sediment deposition in front of the terminus. The flow switching had been gradually occurred over 16 years, probably due to gradual sediment accumulation on the fjord floor. On the other hand, in the case in 2020, glacier flow at the northern terminus decreased by reduction in subglacial water pressure triggered by water level drop of Lago Greve, in which the elapsed time was ~4 months. The flow switching was quite rapid (within 5 months), which we attribute to a change in response to abrupt water level drop. These characteristics imply that change in the flow regime at terminus regions affected the other terminus in a timescale determined by the triggering event.

6.3. The mechanism of drainage event of Lago Greve

Based on these analyses of the satellite images and DEMs, we interpret the mechanism of the outburst as below. Between 9 and 19 April 2020, the bump at the top of the waterfall collapsed (Figure 5.4), so that the stream changed its flow direction to north across the bump location. Because of the change in the flow direction, water began eroding the northern bank of the stream. As the erosion proceeded upstream and the valley deepens, the stream gradually shifted to the north and the water surface dropped. Most likely, the erosion was accelerated by progressive increase in the discharge from the lake. Elevation change near the bump clearly showed formation of a deep V-shaped valley after the event, suggesting erosion by the stream water. (Figure 6.7). In addition, slight uplift after the event was observed in the lower reaches (Profiles 7–11 in Figure 6.7), suggesting deposition of rock debris from the collapse of the bump. We conclude that the collapse of the bump triggered the change in the flow path of the stream, which resulted in the erosion of the valley and the drainage of lakewater.

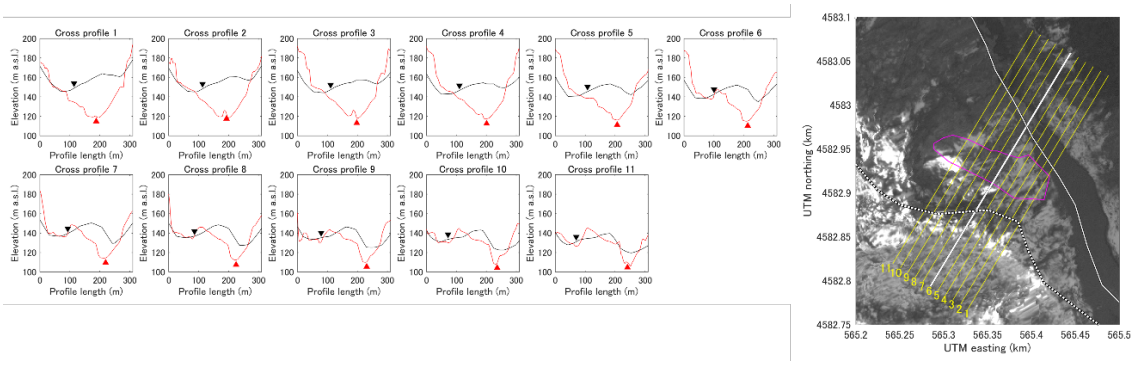

Figure 6.7. Terrain surface elevations along cross profiles across the bump. Elevation along yellow lines in the map). The profiles are set every 10 m from the cross profile of Figure 5.4i (=Profile 6). Triangles in each panel indicate the location of the outlet stream before and after the event.

We speculate that the stream eroded unconsolidated glacial deposits left by the advance of Glaciar Occidental during the Little Ice Age (LIA). The front position of the glacier was approximately at the lake outlet in the ~1870s (Meier et al., 2018; Davies and Glasser, 2012) (dotted line in Figure 5.4a), and the region around the outlet was covered with a moraine formed in front of the glacier (Davies et al., 2020) (gray line in Figure 5.4a). Therefore, it is likely that the region was mantled with glacial deposits as well as sediments carried by lakewater.

The satellite images implied that the event was triggered by the collapse of the bump. However, we do not have information to identify the cause of the collapse. Since flowline of the stream showed no change from April 2000 to 8 April 2020, the process of the collapse was relatively rapid. Given the long distance from the glaciers (> 20 km), the impulse of a wave induced by calving is not a likely trigger. Waves due to landslide or rockfall into the lake are not likely as well, because no trace of such an event was found along the lake shore near the outlet. We also exclude an influence of intensive snow/ice melt because the onset of the event was in April. A relatively small earthquake (magnitude 5.2) was recorded on 5 April 2020 at a depth of 13.6 km and a distance of ~200 km from the lake outlet (west of Cochrane, Chile) (USGS, https://earthquake.usgs.gov/earthquakes/eventpage/us10007exm/origin/detail, last access: 5 December 2021). Nevertheless, this earthquake was at least four days before the onset of the outburst, and probably too weak to destroy the bump. Because there is no weather station around the lake, I employed the ERA5 reanalysis dataset (Hershach and Dee, 2016), and data at grid cells covering the lake (48.9–49.1°S, 73.7–74.1°W) were averaged to show conditions in the study area (Figure 6.8). However, no significant events were found in the weather conditions in the ERA5 reanalysis dataset (Hersbach and Dee, 2016) (Figure 6.8). A field survey is required to investigate the triggering mechanism details further.

Presumably, the collapse of the bump was not directly related to recent warming climate. However, assuming the bump was composed of morainic materials deposited about 1870, the collapse occurred ~150 years after the retreat of Glacier Occidental. Harrison et al. (2018) proposed that GLOF occurs more frequently in the near future as a lagging response to warming climate. The studied event can be regarded as such a delayed response to the changing climate.

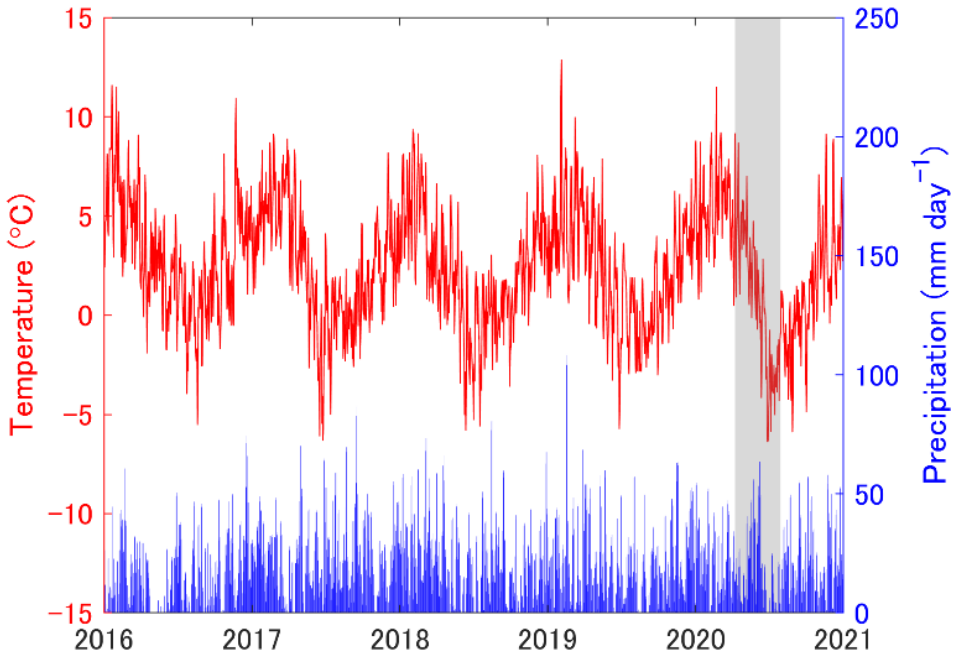

Figure 6.8. Weather condition in the study region. Time series of temperature and precipitation at 48.9–49.1°S, 73.7–74.1°W obtained from the ERA5 reanalysis dataset. Gray shading indicates the period of the lake drainage.

6.4. The lake outburst as observed by GRACE mascon solution

Timeseries of GRACE captured the signal of mass change due to the drainage event of Lago Greve. The GRACE data suggested a range of mass loss from −0.29 to −0.17 m w.e. for the regions within 200–400 km, which correspond to the water volume of 33.4–58.5 km^3. These estimates are substantially greater than the actual volume of the discharge (3.7 ± 0.2 km^3) quantified from the change in the lake surface elevation. The discrepancy would be due to the poor spatial resolution of the GRACE gravimetry. Such an intrinsic low resolution reflects the satellite altitudes larger than the lake size by more than an order of magnitude. Lago Greve is the fourth largest glacial lake in the world, but it occupies only 0.15% of a typical CSR mascon tile (124×10^2 km^2) (Save et al., 2016). A previous study reported that quantification of water volume changes by GRACE is not suitable even for larger glacial lakes (Bigelow et al., 2020). Thus, we conclude that the satellite gravimetry is able to detect large-scale lake outburst events, but care should be taken for quantification of the water discharge. The importance of GRACE in studying GLOF would be increased if mascon solution is adapted for localized events.

Despite the significance and impacts to around environments and society, studies about large-scale GLOFs are scarce because of the rareness to date. Although the drained water volume at the event of Lago Greve is among the largest in satellite era, the lake level drop of the event was relatively small. If we assume the lake expansion and increase in frequency of GLOFs, larger GLOFs can well happen in coming decades. Indeed, formation and expansion trends of glacial lake will perhaps be continued in the world following the warming climate (Shugar et al., 2020). Additionally, warming climate induce thawing of permafrost (Lewkowicz and Way, 2019) and increasing in glacier runoff (Kondo et al., 2021), both of which may trigger landslides and collapse of moraine-dams. Further, glacier-dam become weakening in warming climate due to the glacier thinning. These changes by warming climate possibly increase the frequency and magnitude of large-scale GLOFs. Therefore, even if a GLOF is occurred at remote location and not induced human-related hazards, monitoring the large glacial lakes and further understanding of the mechanisms of large-scale GLOFs are needed for accurate evaluation of the risk in the future mountainous societies.

Chapter 7
Conclusion

7.1. Evolution of Glaciar Pío XI

Changes in the ice-front position and surface elevation of Glaciar Pio XI in 2000–2018 were quantified by analyzing satellite images and DEMs. Changes in ice-front positions of nine termini were quantified, including the southern and northern termini, as well as subsidiary terminus and ice margins calving into lakes located upper regions of the ablation area. Four ice-fronts including the southern and northern terminus had advanced, whereas the other five ice-fronts had been stable during the study period. Maximum advance of 1400 m was observed at the southern terminus, the largest terminus. Surface elevation over the entire ablation area showed increase by 37.3 ± 0.4 m as mean during 2000–2018, and the rate of the increase accelerated by 135 ± 10% from Period 1 (2000–2007) to Period 2 (2007–2017/18). The spatial distribution of the elevation change rate was different between Period 1 and Period 2, elevation change was only slightly positive except for extraordinary thickening (~20 m a^{-1}) observed near the southern terminus during the Period 1 and one of the outlet glacier fronts, whereas significant thickening (~ 2.7 m a^{-1}) occurred over the entire ablation area during Period 2.

Satellite imagery showed an emergence of sedimentary mounds in front of the southern terminus and covered 80% of the ice frontal margin, suggesting that reduction in frontal ablation and increasingly compressive flow regime are the main drivers of the recent rapid thickening and advance. Based on a climate reanalysis dataset, air temperature showed increasing trend over the glacier since 2000. Further, precipitation data showed no evidence of snow fall increase, which may explain the recent rapid advance and thickening. Therefore, we assume the reduction in the frontal ablation and ice speed as the primary control of the glacier change in 2000, whereas snow

accumulation in the relatively large accumulation area affects the longer-term advancing trend of Glaciar Pío XI.

Although the sediment deposition has a significant role in the advance of Pío XI, the contribution of climatic effect to the advance should be evaluated because the relative importance of these factors might determine glacier evolution. Nevertheless, because the uncertainty of climatic variability themselves is large on the western side of the SPI, it is difficult to constrain the contribution of climate variability to the long-term glacier evolution. Even for temperature and precipitation data, we had to rely on reanalysis datasets which are not validated from in-situ data on western side of the SPI. Lack of surface mass balance measurement is also a significant problem. Therefore, for quantitative evaluation and comparison of the climatic and non-climatic effects to evolution of glaciers, intensive researches in the field focusing climatic and non-climatic variables are needed.

7.2. Glacier changes after the drainage of the proglacial lake

Satellite data analysis was performed at Lago Greve and the terminus regions of Glaciar Pío XI, in order to investigate the effect of the lake level change on the glacier evolution.

A 3.7-Gt of water release was found from the measurement of lake area and water level. Observation of lake outlet topography by satellite images and DEMs revealed that abrupt collapse of a bump located near the outlet and subsequent stream-bed erosion were the mechanism of the drainage event. The event was also detected by the gravity field observed by the GRACE/GRACE-FO mascon solution. The GRACE data largely overestimate the volume of water release because its spatial resolution is not sufficiently fine for the GLOF event.

After the drainage event, the northern terminus of Glaciar Pío XI rapidly retreated by 300 m and thinned by 16.3 ± 0.4 m, which was a drastic change from the long-term trend. Glacier velocity of the northern terminus rapidly decreased by 60% after the onset of the drainage event. Thereafter, the glacier showed deceleration until the end of the drainage event. Finally, the velocity reached only 8% of the velocity before the drainage event. This deceleration caused change of the primary flow direction down-glacier from the bifurcating area, from towards the northern terminus before the event to towards the southern terminus after the event. This change in glacier flow regime was attributed to the change in subglacial water pressure caused by the change in lake level. Moreover, the glacier flow switching affected the ice-flux into the termini, which resulted in the rapid thinning of the northern terminus. These observations showed that the lake level change affected the dynamics of the glacier flowing into the lake and the evolution afterwards by affecting the glacier flow regime within a relatively short time scales of several years.

7.3. Future perspectives

In this thesis, I presented a series of study related non-climatic effect to glacier evolution. The suggested mechanisms are based on the interpretations of the satellite observations. However, our knowledge is not sufficient to constrain the mechanism of the changes in the glacier dynamics.

To evaluate the mechanisms of the observed glacier evolution proposed in this thesis, numerical models based on the glacier mechanics are required. Nevertheless, subglacial topography, lake-bed geometry and also depth of Lago Greve, are all missing pieces due to the difficulty of filed observation. To evaluate the influence of sediment deposition to frontal ablation, rate of sediment transport, accumulation, removal by the ocean, and mobility to the glacier pushing should be constrained. Subglacial sediment layer thickness and subglacial water pressure also should be constrained for evaluating the effect of sedimentation on glacier dynamics. Because most glaciers are retreating in recent warming climate, comparison of these factors to other advancing glaciers (e.g., Taku Glacier in Alaska) based on the aspect of glacier dynamics and sedimentation could be valuable insights for understanding calving glacier dynamics, which cannot be seen with monitoring of retreating glaciers alone.

Based on the observation of glacier dynamics before and after the drainage event of Lago Greve, I proposed a change in the subglacial water pressure as a mechanism of changes in the glacier dynamics after the lake level change. GLOFs are expected to occur more frequently in near future because of ongoing warming climate, and the GLOFs could affect dynamics of the glacier flowing the lake. Limited to GLOFs, lake level could be changed affected by the meltwater input, change in strength of a dam, and other factors. Glacier dynamics change in response to the lake level change should be added to numerical models of glacier evolution. Nevertheless, the contribution of the lake level change to the glacier dynamics change is unclear. More investigations are recommended

to expand our knowledge about glacier-lake interaction and GLOF-glacier interaction.

Both sediment deposition and lake level change in front of a glacier are not considered in future projection of global glacier volume change (Hock et al., 2019). On the contrary, frontal ablation of calving glacier is parameterized in models with relatively simple schemes (Hock et al., 2019). Although grasping all of non-climatic forcing is difficult, non-climatic forcing which has large importance to glacier behavior should be investigated carefully because accurate future projection of global glacier mass is critically important. To prioritize among them, evaluation of contribution of various non-climatic forcing should be encouraged.

Based on the results, non-climatic forcings directly affect dynamics of Glaciar Pío XI. However, quantitative comparison between climatic forcing and non-climatic forcing is difficult because of the lack of climatic effect on the western side of the SPI. Therefore, long-term monitoring of both of weather conditions and glacier variations are strongly recommended. Particularly, measurements of surface mass balance and weather conditions (air temperature and precipitation) are urgently needed, and the validation and evaluation of weather variables by field data are also strongly recommended on Glaciar Pío XI and other glaciers in western side of the SPI.

Acknowledgements

The Ph. D. work was guided by Professor Shin Sugiyama (Hokkaido University), Chair of the Ph.D. committee and a supervisor of the author. He supported my research works for the last 5 years since Master's program of the graduate school. I would like to express my gratitude to him for helpful discussion during the work as well as offering abundant opportunities of field observations and novel ideas.

Proessor Ralf Greve (Hokkaido University), Professor Tsutomu Watanabe (Hokkaido University), Professor Koji Fujita (Nagoya University), and Dr. Masahiro Minowa (Hokkaido University), members of the Ph.D. comittee, provided constructive and insightful comments for the study.

Dr. Masahiro Minowa provided me opportunities of field work and frequent discussions, and generous guide during field activities. Professor emeritus Kosuke Heki (Hokkaido University) helped the satellite gravimetry analysis and provided ample opportunity of discussions on space geodesy. Professsor Takanobu Sawagaki (Hosei University) provided basic knowledges about photogrammety and its analysis. Professor Chiyuki Narama (Niigata University) provided constructive comments about glacial lakes and its outburst phenomenon. Dr. Yoshinori Iizuka (Hokkaido University) helped and guided me through comments from general glaciology. Dr. Shun Tsutaki (National Institute of Polar Research) provided valuable comments and discussions on glacier dynamics. Dr. Daiki Sakakibara guided me how to handle and analyze satellite images.

I would like to thank Mr. Yefan Wang and Mr. Ken Kondo, colleagues of the Glacier and Ice Sheet Research Group, Institute of Low Temperature Science, Hokkaido University. Their enthusiastic and intellectual curiosity, and day-to-day discussions with them always motivated my work. I would like to thank all the members of the Glacier and

Ice Sheet Research Group, Institute of Low Temperature Science, Hokkaido University for their kind support.

Finally, I would like to express appreciation for supports from my supporters, parents, sisters, and Yui Kouchiyama. Their comprehension to my research kindly supported my research activities.

This reseach was funded by the the Japan Society for the Promotion of Science through a Grant-in-Aid for Scientific Research 16H05734 (2016–2019) and 20H00186 (2020–2025), and by JST SPRING Grant Number JPMJSP2119 (2021–2022).

References

Abdel Jaber, W., H. Rott, D. Floricioiu, J. Wuite, and N. Miranda (2019). Heterogeneous spatial and temporal pattern of surface elevation change and mass balance of the Patagonian ice fields between 2000 and 2016, *The Cryosphere*, **13**, 2511–2535, Doi: 10.5194/tc-13-2511-2019

Abdel Jaber, W. (2016), Derivation of mass balance and surface velocity of glaciers by means of high resolution synthetic aperture radar: application to the Patagonian Icefields and Antarctica, Dissertation, Technische Universität München, available at: http://elib.dlr.de/109075/ (last access: 14 April 2020)

Albergel, C, E. Dutra, S. Munier, J.C. Calvet, J. Munoz-Sabatere, P. de Rosnay and G. Balsamo (2018). ERA-5 and ERA-Interim driven ISBA land surface model simulations: which one performs better?, *Hydrology and Earth System Sciences*, 22, 3515–3532, Doi:10.5194/hess-22-3515-2018.

Amundson, J.M. (2016). A mass-flux perspective of the tidewater glacier cycle, *Journal of Glaciology*, **62**(12), 82–93, Doi: 10.1017/jog.2016.14

de Angelis (2014). Hypsometry and sensitivity of the mass balance to changes in equilibrium-line altitude: the case of the Southern Patagonia Icefield, *Journal of Glaciology*, **60**(219), 14–28, Doi: 10.3189/2014JoG13J127.

Aniya, M., H. Sato, R. Naruse, P. Skvarca and G. Casassa (1997). Recent variations in the Southern Patagonia Icefield, South America, *Arctic and Alpine Research*, **29**(1), 1–12

Aniya, M., Dussaillant, A., O'arcaza, G., & Kuinghttons, J., Barcaza, G., and Bravo, S. (2020). GLOFs of Laguna de los Témpanos, glacier-dammed side lake of Glaciar Steffen, Hielo Patagónico Norte, Chile, since 1974. *Bulletin of Glaciological Research*, **38**, 13–24, Doi: 10.5331/bgr.20R01.

Arendt, A., K. Echelmeyer, W. Harrison, C. Lingle, S. Zirnheld, V. Valentine, B. Ritchie and M. Druckenmiller (2006). Updated estimated of glacier volume changes in the western Chugach Mountains, Alaska, and a comparison of regional extrapolation methods, Journal of Geophysical Research, 111, F03019, Doi:10.1029/2005JF000436.

Bigelow, D.G., G.E. Floers, C.G. Schoof, L.D.B. Mingo, E.M. Young and B.G. Connal (2020). The role of englacial hydrology in the filling and drainage of an ice-dammed lake, Kaskawulsh Glacier, Yukon, Canada. Journal of Geophysical Research: Earth Surface, 125, e2019JF005110, Doi: 10.1029/2019JF005110.

Bolch, T., T. Pieczonka and D. I. Benn (2011). Multi-decadal mass loss of glaciers in the Everest area (Nepal Himalaya) derived from stereo imagery, *The Cryosphere*, **5**, 349–358, Doi: 10.5194/tc-5-349-2011.

Braun, M.H., P. Malz, C. Sommer, D. Farías-Barahona, T. Sauter, G. Casasssa, A. Soruco, P. Skvarca and T. C. Seehaus (2019). Constraining glacier elevation and mass changes in South America. *Nature Climate Change*, **9**, 130–136, Doi: 10.1038/s41558-018-0375-7.

Bravo, C., D. Bozkurt, Á. Gonzalez-Reyes, D. J. Quincey, A. N. Ross, D. Farías-Barahona and M. Rojas (2019). Assessing Snow Accumulation Patterns and Changes on the Patagonian Icefields, Frontiers in Earth Science, **7**(1), 30, Doi: 10.3389/fenvs.2019.00030

Brinkerhoff, D., M. Truffer and A. Aschwanden (2017). Sediment transport drives tidewater glacier periodicity, *Nature Communications*, **8**, 90, Doi: 10.1038/s41467-017-00095-5

Brun, F., E. Berthier, P. Wagnon, A. Kääb and D. Treichler (2017), A spatially resolved estimate of High Mountain Asia glacier mass balances from 2000 to 2016. *Nature Geoscience*, **10**, 668–673, Doi: 10.1038/ngeo2999.

Carabajai, C.C. and J-.P. Boy (2021). Lake and reservoir volume variations in South America from radar altimetry, ICESat laser altimetry, and GRACE time-variable gravity. Advances in Space Research, **68**(2), 652–271. Doi: 10.1016/j.asr.2020.04.022.

Carrivick, J. L., & Tweed, F. S. Proglacial lakes: character, behaviour and geological importance (2013). Quaternary Science Reviews, **78**, 34–52, Doi: 10.1016/j.quascirev.2013.07.028.

Carrivick, J. L., B. J. Davies, W. H. M. James, D. J. Quincey and N. F. Glasser (2016). Distributed ice thickness and glacier volume in southern South America, *Global and Planetary Change*, **146**, 122–132, Doi: 10.1016/j.gloplacha.2016.09.010.

Carrivick, J.L., and F.S. Tweed (2016). A global assessment of the societal impacts of glacier outburst floods. *Global and Planetary Change*. **144**, 1–16. Doi: 10.1016/j.gloplacha.2016.07.001.

Carrivick J. L., F. S. Tweed, J. L. Sutherland, and J. Mallalieu (2020). Toward numerical modeling of interactions between ice-marginal proglacial lakes and glaciers,. *Frontiers in Earth Science*, ***8***:577068, Doi: 10.3389/feart.2020.577068.

Chen, J. L., C.R. Wilson, B.D. Tapley, D.D. Blankenship, and E.R. Ivins, (2007). Patagonia Icefield melting observed by Gravity Recovery and Climate Experiment (GRACE). *Geophysical Research Letters*, **34**, L22501. Doi:

10.1029/2007GL031871.

Cuffery, K. and W.S.B. Paterson (2010). The Physics of Glaciers, 4th ed., *Elsevier*, Burlinton, Mass.

Davies, B., and Glasser, N. (2012). Accelerating shrinkage of Patagonian glaciers from the Little Ice Age (~AD 1870) to 2011. *Journal of Glaciology*, **58**(212), 1063–1084, Doi: 10.3189/2012JoG12J026.z

Davies, B.J., C.M. Darvill, H. Lovell, J.M. Bendle, J.A. Dowdeswell, D. Fabel, J-.L. GarcÍa, A. Geiger, N.F. Glasser, D.M. Gheorghiu, S. Harrison, A.S. Hein, M.R. Kaplan, J.R.V. Martin, M. Mendelova, A. Palmer, M. Pelto, A. Rodés, E.A. Sagredo, R.K. Smedley, H.L. Smellie, and V.R. Thorndycraft (2020). The evolution of the Patagonian Ice Sheet from 35 ka to the present day (PATICE), *Earth-Science Reviews*, **204**, 103–152, Doi: 10.1016/j.earscirev.2020.103152

Dowdeswell, J. A., and M. Vásquez (2013). Submarine landforms in the fjords of southern Chile: implications for glacimarine processes and sedimentation in a mild glacier-influenced environment, *Quaternary Science Reviews*, **64**, 1–19, Doi: 10.1016/j.quascirev.2012.12.003.

Dussaillant, A., G. Benito, W. Buytaert, P. Carling, C. Meier, and F. Espinoza (2010). Repeated glacial-lake outburst floods in Patagonia: an increasing hazard?. *Natural Hazards*, **54**, 469–481, Doi: 10.1007/s11069-009-9479-8.

Dussaillant, I., E. Berthier, F. Brun, M. Masaiokas, R. Hugonnet, V. Favier, A. Rabatel P. Pitte and L. Ruiz (2019). Two decades of glacier mass loss along the Andes, *Nature Geoscience*, **12**, 802–808, Doi: 10.1038/s41561-019-0432-5.

Dussaillant, I., E. Berthier, and F. Brun (2018). Geodetic Mass Balance of the Northern Patagonian Icefield from 2000 to 2012 Using Two Independent Methods,. *Frontiers in Earth Science*, **6**:8. Doi: 10.3389/feart.2018.00008.

Dryakk M.C. and E.M. Enderlin (2020). Analysis of Antarctic Peninsula glacier frontal ablation rates with respect to iceberg melt-inferred variability in ocean conditions, *Journal of Glaciology*, **66**(257), 457–470, Doi: 10.1017/jog.2020.21.

Earth Resources Observation and Science (EROS) Center (2017). Shuttle Radar Topography Mission (SRTM) 1 Arc-Second Global [Data set]. *U.S. Geological Survey*, Doi: 10.5066/F7PR7TFT.

Emmer, A. and A. Cochachin (2013). The causes and mechanisms of moraine-dammed lake failures in the Cordillera Blanca, North American Cordillera, and Himalayas,. *AUC Geographica*, **48**(2), 5–13, Doi: 10.14712/23361980.2014.23.

Emmer, A., J.L. Wood, S.J. Cook, S. Harrison, R. Wilson, A. Diaz-Moreno, J.M. Reynolds, J.C. Torres, C. Yarleque, M. Mergili, H.W. Jara, G. Bennett, A. Caballero, N.F.

Glasser, E. Melgarejo, C. Riveros, S. Shannon, E. Turpo, T. Tinoco, L. Torres, D. Garay, H. Villafane, H. Garrido, C. Martinez, N. Apaza, J. Araujo and C. Poma (2022), 160 glacial lake outburst floods (GLOFs) across the Tropical Andes since the Little Ice Age. *Global and Planetary Change*, **208**, 103722, Doi: 10.1016/j.gloplacha.2021.103722.

Enderlin, E.M., S. O'Neel, T.C. Bartholomaus and I. Joughin (2018). Evolving Environmental and Geometric Controls on Columbia Glacier's Continued Retreat, *Journal of Geophysical Research: Earth Surface*, **123**(7), 1528–1545, Doi: 10.1029/2017JF004541

Farinotti, D., M. Huss, M., J.J. Fürst, J. Landmann, H. Machguth, F. Maussion and A. Pandit (2019). A consensus estimate for the ice thickness distribution of all glaciers on Earth. *Nature Geoscience*, **12**, 168–173, Doi: 10.1038/s41561-019-0300-3.

Field, H.R, W.H. Armstrong, and M. Huss. Gulf of Alaska ice-marginal lake area change over the Landsat record and potential physical controls, (2021). *The Cryosphere*, 15, 3255–3278. Doi:10.5194/tc-15-3255-2021.

Foresta, L., N. Gourmelen, F. Weissgerber, P. Nienow, J. Williams, A. Shepherd, M. Drinkwater and S. Plummer, (2018). Heterogeneous and rapid ice loss over the Patagonian Ice Fields revealed by CryoSat-2 swath radar altimetry, *Remote Sensing of Environment*, **211**, 441–455, Doi: 10.1016/j.rse.2018.03.041.

Fried, M.J., G.A. Catania, T.C. Bartholomaus, D. Duncan, M. Davis, L.A. Stearns, J. Nash, E. Shroyer and D. Sutherland (2015). Distributed subglacial discharge drives significant submarine melt at a Greenland tidewater glacier, *Geophysical Research Letters*, **42**,21 9328–9336. Doi: 10.1002/2015GL065806.

Gardelle, J., E. Berthier, Y. Arnaud, A. Kääb (2013), Region-wide glacier mass balances over the PamirKarakoram-Himalaya during 1999-2011, *The Cryosphere*, **7**, 1263–1286, Doi: 10.5194/tc-7-1263-2013.

Gardner, A. S., M. A. Fahnestock, and T. A. Scambos (2019) [update to time of data download]: ITS_LIVE Regional Glacier and Ice Sheet Surface Velocities. Data archived at National Snow and Ice Data Center; doi:10.5067/6II6VW8LLWJ7.

Glasser, N.F., K.N. Jansson, G.A.T. Duller, J. Singarayer, M. Holloway, and S. Harrison, (2016). Glacial lake drainage in Patagonia (13-8 kyr) and response of the adjacent Pacific Ocean. *Scientific Reports*, **6**:21064, Doi: 10.1038/srep21064.

Gudmundsson, M.T., H. Björnsson, and F. Pálsson (1995). Changes in jökulhlaup sizes in Grímsvotn, Vatnajökull, Iceland, 1934–91, deduced from in-situ measurements of subglacial lake volume, *Journal of Glaciology*, **41**(138), 263–272. Doi:10.3189/S0022143000016166.

Grinsted, A., C.S. Hvidberg, N. Campos, and D. Dahl-Jensen (2017), Periodic outburst floods from an ice-dammed lake in East Greenland (2017). *Scientific Reports*, **7**:9966. Doi: 10.1038/s41598-017-07960-9.

Hanshaw, M.N. and B. Bookhagen (2014). Glacial areas, lake areas, and snow lines from 1975 to 2012: status of the Cordillera Vilcanota, including the Quelccaya Ice Cap, northern central Andes, Peru, *The Cryosphere*, **8**, 359–376, Doi: 10.5194/tc-8-359-2014.

Harrison, S., J.S. Kargel, C. Huggel, J. Reynolds, D.H. Shugar, R.A. Betts, A. Emmer, N. Glasser, U.K. Haritashya, J. Klimes, L. Reinhardt, Y. Schaub, A. Wiltshire, D. Regmi and V. Vilímek, (2018). Climate change and the global pattern of moraine-dammed glacial lake outburst floods, *The Cryosphere*, **12**, 1195–1209, Doi: 10.5194/tc-12-1195-2018.

Heinsheimer, G.J., Zur Hydrologie und Glaziologie del Lago Argentino und Ventisquero Moreno III, (1958). *Zeitschrift für Gletscherkunde and Glazialgeologie*, **4**, 61–72.

Hersbach, H. and D. Dee (2016), ERA reanalysis is in production, ECMWF Newsl., 147, 7. Available at: https://www.ecmwf.int/en/newsletter/147/news/era5-reanalysis-production.

Hock, R., A. Bliss, B. Marzeion, R.H. Giesen, Y. Hirabayashi, M. Huss, V. Radic, and A.B.A. Slangen (2019). GlacierMIP – A model intercomparison of global-scale glacier mass-balance models and projections, *Journal of Glaciology*, **65**(251), 453–467, Doi: 10.1017/jog.2019.22.

How, P., D. I. Benn, N.R.J. Hulton, B. Hubbard, A. Luckman, H. Sevestre, W.J.J. van Pelt, K. Lindbäck, J. Kohler and W. Boot (2017). Rapidly changing subglacial hydrological pathways at a tidewater glacier revealed through simultaneous observations of water pressure, supraglacial lakes, meltwater plumes and surface velocities, *The Cryosphere*, **11**, 2691–2710, Doi: 10.5194/tc-11-2691-2017.

Hubbard, B., Heald, A., J.M., Quincey, D., Richardson, S.D., Luyo, M.Z., Portilla, N.S. and Hambrey, M.J., (2005). Impact of a rock avalanche on a moraine-dammed proglacial lake: Laguna Safuna Alta, Cordillera Blanca, Peru, *Earth Surface Processes and Landforms*, **30**(10), 1251–1264, Doi: 10.1002/esp.1198.

Hugonnet, R., R. McNabb, E. Berthier, B. Menounos, C. Nuth, L. Girod, D. Farinotti, M. Huss, I. Dussaillant, F. Brun and A. Kääb (2021). Accelerated global glacier mass loss in the early twenty-first century. *Nature*, **592**, 726–731. Doi: 10.1038/s41586-021-03436-z.

IPCC, (2019), IPCC Special Report on the Ocean and Cryosphere in a Changing Climate [H.-O. Pörtner, D.C. Roberts, V. Masson-Delmotte, P. Zhai, M. Tignor, E.

Poloczanska, K. Mintenbeck, A. Alegría, M. Nicolai, A. Okem, J. Petzold, B. Rama, N.M. Weyer (eds.)].

Jiang, L., K. Nielsen, O.B. Andersen, and P. Bauer-Gottwein (2017). Monitoring recent lake level variations on the Tibetan Plateau using CryoSat-2 SARIn mode data, (2017). *Journal of Hydrology*, **544**, 109–124. Doi:10.1016/j.jhydrol.2016.11.024.

Jasinski, M. F., J. D. Stoll, D. Hancock, J. Robbins, J. Nattala, J. Morison, B. M. Jones, M. E. Ondrusek, T. M. Pavelsky, C. Parrish, and the ICESat-2 Science Team. (2019). ATLAS/ICESat-2 L3A Inland Water Surface Height, Version 2. Boulder, Colorado USA. NASA National Snow and Ice Data Center Distributed Active Archive Center., Doi: 10.5067/ATLAS/ATL13.002.

Joughin, I., I.M. Howat, M. Fahnestock, B. Smith, W. Krabill, R.B. Alley, H. Stern and M. Truffer (2008). *Journal of Geophysical Research*, **113**, F04006, Doi:10.1029/2008JF001023.

Joughin, I., B.E. Smith and I. Howat (2018). Greenland Ice Mapping Project: ice flow velocity variation at sub-monthly to decadal timescales, *The Cryosphere*, **12**, 2211–2227, Doi :10.5194/tc-12-2211-2018.

Khazendar, A., I.G. Fenty, D. Carroll, A. Gardner, C.M. Lee, I. Fukumori, O. Wang, H. Zhang, H. Seroussi, D. Moller, B.P.Y. Noël, M. R. van den Broeke, S. Dinardo and J. Willis (2019). Interruption of two decades of Jakobshavn Isbrae acceleration and thinning as regional ocean cools, *Nature Geoscience*, **12**, 277–278, Doi: 10.1038/s41561-019-0329-3.

King, M.D., I. Howat, S. Jeong, M.J. Noh, B. Wouters, B. Noël and M.R. van den Broeke (2018). Seasonal to decadal variability in ice discharge from the Greenland Ice Sheet, *The Cryosphere*, **12**, 3813–3825, Doi: 10.5194/tc-12-3813-2018.

King, O., Bhattacharya, A., Bhambri, and Bolch, T. (2019). Glacial lakes exacerbate Himalayan glacier mass loss. *Scientific Reports,* **9**, 18145, Doi: 10.1038/s41598-019-53733-x.

Köhler, A., M. Pętlicki, P.-M. Lefeuvre, G. Buscaino, C. Nuth and C. Weidle (2019). Contribution of calving to frontal ablation quantified from seismic and hydroacoustic observations calibrated with lidar volume measurements, *The Cryosphere*, **13**, 3117–3137, Doi: 10.5194/tc-13-3117-2019.

Kondo, K., S. Sugiyama, D. Sakakibara and S. Fukumoto (2021). Flood events caused by discharge from Qaanaaq Glacier, northwestern Greenland, *Journal of Glaciology*, **67**(263), 500–510, Doi: 10.1017/jog.2021.3

Kruiger, E. M., M. Truffer, R. J. Motyka and A. K. Bucki (2006), Episodic reactivation of large-scale push moraines in front of the advancing Taku Glacier, Alaska, Journal of Geophysical Research, **111**, F01009, Doi: 10.1029/2005JF000385.

Lenzano, M.G., E. Lannutti, C. Toth, L. Lenzano, A.L. Vecchio, D. Falaschi, and A. Vich, Analyzing the oscillations of the Perito Moreno Glacier, using time-lapse image sequences, (2018). *Cold Regions Science and Technology*, **146**, 155–166, Doi: 10.1016/j.coldregions.2017.11.015.

Lewkowicz, A.G. & R.G. Way (2019). Extremes of summer climate trigger thousands of thermokarst landslides in a High Arctic environment, *Nature Communications*, **10**, 1329, Doi: 10.1038/s41467-019-09314-7.

Li, J., J. Chen, S. Ni, L. Tang, and X Hu (2019). Long-term and inter-annual mass changes of Patagonia Ice Field from GRACE. *Geodesy and Geodynamics*, **10**(2), 100–109. Doi: 10.1016/j.geog.2018.06.001.

Lopez, P., P. Chevallier, V. Favier, B. Pouyaud, F. Ordenes and J. Oerlemans (2010), A regional view of fluctuations in glacier length in southern South America, *Global and Planetary Change* **71**(1–2), 85–108, Doi: 10.1016/j.gloplacha.2009.12.009.

Mallalieu, J., J.L. Carrivick, D.J. Quincey and C.L. Raby (2021). Ice-marginal lakes associated with enhanced recession of the Greenland Ice Sheet, *Global and Planetary Change*, **202**, 103503. Doi: 10.1016/j.gloplacha.2021.103503.

Malz, P., W. Meier, G. Casassa, R. Jaña, P. Skvarca and M. Braun (2018), Elevation and Mass Changes of the Southern Patagonia Icefield Derived from TanDEM-X and SRTM Data, *Remote Sensing*, **10**(188), 1–17, Doi: 10.3390/rs10020188.

Mayo, L.R. (1989). Advance of Hubbard Glacier and 1986 outburst of Russell Fiold, Alaska, U.S.A., *Annals of Glaciology*, **13**, 189–194.

McFadden, E.M., I.M. Howat, I. Joughin, B.E. Smith and Y. Ahn (2011). Changes in the dynamics of marine terminating outlet glaciersin west Greenland (2000–2009), *Journal of Geophysical Research*, **116**, F02022, Doi: 10.1029/2010JF001757.

McFeeters, S.K. (1996), The use of the Normalized Difference Water Index (NDWI) in the delineation of open water features, *International Journal of Remote Sensing*, **17**(7), 1425–1432, Doi: 10.1080/01431169608948714.

McFeeters, S.K. (2013), Using the Normalized Difference Water Index (NDWI) within a Geographic Information System to Detect Swimming Pools for Mosquito Abatement: A Practical Approach, *Remote Sensing*, **5**, 3544–3561, Doi: 10.3390/rs5073544.

McNabb, R.W. and R. Hock (2014). Alaska tidewater glacier terminus positions, 1948–2012. *Journal of Geophysical Research: Earth Surface*, **119**, 153–167, Doi: 10.1002/2013JF002915.

McNabb, R.W., R. Hock and M. Huss (2015). Variations in Alaska tidewater glacier frontal ablation, 1985–2013, *Journal of Geophysical Research: Earth Surface*, **120**,

120–136, Doi: 10.1002/2014JF003276.

Meerhoff, E., L.R. Castro, F.J. Tapia, and I. Pérez-Santos (2019). Hydrographic and Biological Impacts of a Glacial Lake Outburst Flood (GLOF) in a Patagonian Fjord, *Estuaries and Coasts*, **42**, 132–143, Doi: 10.1007/s12237-018-0449-9.

Meier, M.F. and A. Post (1987). Fast tidewater glaciers. *Journal of Geophysical Research: Solid Earth*, **92**, 9051–9058.

Meier, W.J-H., J. Grießinger, P. Hochreuther, and M.H. Braun (2018). An Updated Multi-Temporal Glacier Inventory for the Patagonian Andes With Changes Between the Little Ice Age and 2016. *Frontiers in Earth Science*, **6**, 62. Doi:10.3389/feart.2018.00062.

Millan, R., E. Rignot, A. Rivera, V. Martineau, J. Mouginot, R. Zamora, J. Uribe, G. Lenzano, B. De Fleurian, X. Li, Y. Gim and D. Kirchner (2019). Ice Thickness and Bed Elevation of the Northern and Southern Patagonian Icefields, *Geophysical Research Letters*, **46**, 6626–6635, Doi: 10.1029/2019GL082485.

Millan, R. J. Mouginot, A. Rabatel and M. Morlighem (2022). Ice velocity and thickness of the world's glaciers, *Nature Geoscience*, **15**, 124–129, Doi: 10.1038/s41561-021-00885-z.

Minowa, M., S. Sugiyama, D. Sakakibara and P. Skvarca (2017). Seasonal variations in the ice–front position controlled by frontal ablation at Glaciar Perito Moreno, Southern Patagonia Icefield. *Frontiers in Earth Science*, **5**:1, Doi:10.3389/feart.2017.00001.

Minowa, M., E.A. Podolskiy, S. Sugiyama, D. Sakakibara and P. Skvarca (2018), Glacier calving observed with time-lapse imagery and tsunami waves at Glaciar Perito Moreno, Patagonia, *Journal of Glaciology*, **64**(245), 362–376, Doi:10.1017/jog.2018.28.

Minowa, M. E.A. Podolskiy, G. Jouvet, Y. Weidmann, D. Sakakibara, S. Tsutaki, R. Genco and S. Sugiyama (2019a). Calving flux estimation from tsunami waves, *Earth and Planetary Science Letters*, **515**, 283–290, Doi: 10.1016/j.epsl.2019.03.023.

Minowa, M., M. Schaefer, P. Skvarca, S. Matoba and G. Gacitúa (2019b). Glaciological traverse across the Southern Patagonian Icefield, *Bulletin of Glaciological Research*, **37**, 47–56, Doi: 10.5331/bgr.19R03.

Minowa, M., Schaefer, M., Sugiyama, S., Sakakibara, D., and Skvarca, P. (2021). Frontal ablation and mass loss of the Patagonian icefields., *Earth and Planetary Science Letters*, **561**, 116811, Doi: 10.1016/j.epsl.2021.116811.

Moon and Joughin (2008). Changes in ice front position on Greenland's outlet glaciers from 1992 to 2007, Journal of Geophysical Research, **113**, Doi:

10.1029/2007JF000927.

Morlighem, M., C. N. Williams, E. Rignot, L. An, J. E. Arndt, J. L. Bamber, G. Catania, N. Chauché, J. A. Dowdeswell, B. Dorschel, I. Fenty, K. Hogan, I. Howat, A. Hubbard, M. Jakobsson, T.M. Jordan, K.K. Kjeldsen, R. Millan, L. Mayer, J. Mouginot, B.P.Y. Noël, C. O'Cofaigh, S. Palmer, S. Rysgaard, H. Seroussi, M.J. Siegert, P. Slabon, F. Straneo, M.R. van den Broeke, W. Weinrebe, M. Wood, and K.B. Zinglersen (2017). BedMachine v3: Complete bed topography and ocean bathymetry mapping of Greenland from multibeam echo sounding combined with mass conservation. *Geophysical Research Letters*, **44**, 11051–11061. Doi: 10.1002/2017GL074954

Morlighem, M., E. Rignot, T. Binder, D. Blankenship, R.Drews, G. Eagles, O. Eisen, F. Ferraccioli, R. Forsberg, P. Fretwell, V. Goel, J.S. Greenbaum, H. Gudmundsson, J. Guo, V. Helm, C. Hofstede, I. Howat, A. Humbert, W. Jokat, N. B. Karlsson, W. S. Lee, K. Matsuoka, R. Millan, J. Mouginot, J. Paden, F. Pattyn, J. Roberts, S. Rosier, A. Ruppel, H. Seroussi, E.C. Smith, D. Steinhage, B. Sun, M. R. van den Broeke, T.D. van Ommen, M. van Wessem and D.A. Young (2020). Deep glacial troughs and stabilizing ridges unveiled beneath the margins of the Antarctic ice sheet. *Nature Geoscience*, **13**, 132–137. Doi: 10.1038/s41561-019-0510-8.

Motyka, R.J. and J.E. Begét (1996). Taku Glacier, southeast Alaska, U.S.A.,: Late Holocene history of a tidewater glacier. *Antarctic and Alpine Research*, **28**(1), 42–51.

Motyka, R.J. and K. A. Echelmeyer (2003). Taku Glacier (Alaska, U.S.A.) on the move again: active deformation of proglacial sediments, *Journal of Glaciology*, **49**(164), 50–58, Doi: 10.3189/172756503781830962.

Motyka, R.J., M. Truffer, E.M. Kuriger and A.K. Bucki (2006). Rapid erosion of soft sediments by tidewater glacier advance: Taku Glacier, Alaska, USA, *Geophysical Research Letters*, **33**, L24504, Doi: 10.1029/2006GL028467.

Motyka, R.J., M. Truffer, M. Fahnestock, J. Mortensen, S. Rysgaard and I. Howat (2011). Submarine melting of the 1985 Jakobshavn Isbræ floating tongue and the triggering of the current retreat, *Journal of Geophysical Research: Earth Surface*, **116**(F1), Doi: 10.1029/2009JF001632

Mouginot, J. and E. Rignot (2015). Ice motion of the Patagonian Icefields of South America: 1984–2014, *Geophysical Research Letters*, **42**, 1441–1449, Doi: 10.1002/2014GL062661.

Muto M. and M. Furuya (2013). Surface velocities and ice-front positions of eight major glaciers in the Southern Patagonian Ice Field, South America, from 2002 to 2011,

Remote Sensing of Environment, **139**, 50–59, Doi: 10.1016/j.rse.2013.07.034.

Neupene, R., H. Chen, and C. Cao (2019). Review of moraine dam failure mechanism. Geomatics, *Natural Hazards and Risk*, **10**(1), 1948–1966. Doi: 10.1080/19475705.2019.1652210.

Nie, Y., Y. Shen, Q. Liu, L. Liu, S. Liu, Y. Zhang, and C. Song, (2017). A regional-scale assessment of Himalayan glacial lake changes using satellite observations from 1990 to 2015. *Remote Sensing of Environment*, **189**, 1–13. Doi:10.1016/j.rse.2016.11.008.

Nolan, M., R.J. Motyka, K. Echelmeyer and D.C. Trabant (1995). Ice-thickness measurements of Taku Glacier, Alaska, U.S.A., and their relevance to its recent behavior, *Journal of Glaciology*, **41**(139), 541–553.

Nuth, C., G. Moholdt, J. Kohler, J. O. Hagen, and A. Kääb (2010), Svalbard glacier elevation changes and contribution to sea level rise, *Journal of Geophysical Research*, **115**, F01008, Doi: 10.1029/2008JF001223.

Nuth, C. and A. Kääb (2011), Co-registration and bias corrections of satellite elevation data sets for quantifying glacier thickness change, *The Cryosphere*, **5**, 271–290, Doi: 10.5194/tc-5-271-2011.

Pasquini, A.I., and P.J. Deptris (2011). Southern Patagonia's Perito Moreno Glacier, Lake Argentino, and Santa Cruz River hydrological system: An overview, Journal of Hydrology, 405, 48–56, Doi: 10.1016/j.jhydrol.2011.05.009,

Paul, F., T. Tolch, K. Briggs, A. Kääb, M. McMillan, R. McNabb, T. Nagler, C. Nuth, P. Rastner, T. Strozzi and J. Wuite (2017) Error sources and guidelines for quality assessment of glacier area, elevation change, and velocity products derived from satellite data in the Glaciers_cci project, *Remote Sensing of Environment*, **203**, 256–275, Doi: 10.1016/j.rse.2017.08.038.

Pereira, A., C. Cornero, A.C.O.C. Matos, M.C. Pacino, and D. Blitzkow (2021). Detection of total water mass changes in the Patagonian glaciers area by satellite gravimetry. *Geofísica Internacional*, **60**(2), 161–174. Doi: 10.22201/igeof.00167169p.2021.60.2.2086.

Podrasky, D., M. Truffer, M. Lüthi and M. Fahnestock (2014). Quantifying velocity response to ocean tides and calving near the terminus of Jakobshavn Isbræ, Greenland, *Journal of Glaciology*, **60**(222), 609–621, Doi: 10.3189/2014JoG13J130.

Podolskiy, E. A., S. Sugiyama, M. Funk, F. Walter, R. Genco, S. Tsutaki, M. Minowa and M. Ripepe (2016). Tide-modulated ice flow variations drive seismicity near the calving front of Bowdoin Glacier, Greenland. *Geophysical Research Letters*, **43**,

2036–2044. doi:10.1002/2016GL067743.

Post, A (1975). Preliminary Hydrography and Historic Terminal Changes of Columbia Glacier, Alaska. Technical Report, United States Geological Survey. http://pubs.er.usgs.gov/publication/ha559.

RGI Consortium (2017): Randolph Glacier Inventory – A Dataset of Global Glacier Outlines: Version 6.0: Technical Report, Global Land Ice Measurements from Space, Doi: 10.7265/N5-RGI-60.

Rignot, E., A. Rivera, and G. Casassa (2003). Contribution of the Patagonia Icefields of South America to sea level rise, *Science*, **302**, 434–437, Doi: 10.1126/science.1087393, 2003.

Rignot, E., I. Fenty, Y. Xu, C. Cai and C. Kemp (2015). Undercutting of marine-terminating glaciers in West Greenland, *Geophysical Research Letters*, **42**, 5909–5917, Doi: 10.1002/2015GL064236.

Rivera, A. (1992). El Glaciar Pio XI: Avances y retrocesos, El impacto sobre su entorno durante el presente siglo, *Revista Geográfica de Chile Terra Australis*, **36**, 33–62.

Rivera, A., J.C. Aravena and G. Casassa (1997a). Recent fluctuations of Glaciar Pio XI, Patagonia: Discussion of a glacial surge hypothesis, *Mount. Res. Dev.*, **17**(4), 309–322, Doi: 10.2307/3674021.

Rivera, A., H. Lange, J.C. Aravena and G. Casassa (1997b), The 20th-century advance of Glaciar Pio XI, Chilean Patagonia, *Annals of Glaciology*, **24**, 66–71, Doi: 10.3189/S0260305500011952.

Rivera, A. and G. Casassa (1999), Volume changes on Pio XI glacier, Patagonia: 1975–1995, *Global and Planetary Change*, **22**, 1–4.

Rivera, A. (2018), Glaciar Pío XI: La excepción a la tendencia de desglaciación en Patagonia Pio XI glacier: The exception to the deglaciation trend in Patagonia, *Revista Geográfica de Chile Terra Australis*, **54**, 1–12.

Sakakibara, D. and S. Sugiyama (2014). Ice-front variations and speed changes of calving glaciers in the Southern Patagonia Icefield from 1984 to 2011, *Journal of Geophysical Research: Earth Surface*, **119**, 2541–2554, Doi: 10.1002/2014JF003148.

Sauter, T. (2020). Revisiting extreme precipitation amounts over southern South America and implications for the Patagonian Icefields, *Hydrology and Earth System Sciences*, **24**, 2003–2016. Doi: 10.5194/hess-24-2003-2020.

Sasgen, I., H. Konrad, V. Helm and K. Grosfeld, (2019). High-Resolution Mass Trends of the Antarctic Ice Sheet through a Spectral Combination of Satellite Gravimetry and Radar Altimetry Observations. *Remote Sensing*, **11**, 144,

Doi:10.3390/rs11020144.

Save, H., S. Bettadpur, & B. D. Tapley (2016). High resolution CSR GRACE RL05 mascons, *Journal of Geophysical Research: Solid Earth*, **121**, 7547–7569. Doi:10.1002/2016JB013007.

Schaefer, M., H. Machguth, M. Falvey, G. Casassa, and E. Rignot (2015). Quantifying mass balance processes on the Southern Patagonia Icefield, *The Cryosphere*, **9**, 25–35, Doi: 10.5194/tc-9-25-2015.

Schwikowski, M., M. Schläppi, P. Santibañez, A. Rivera, and G. Casassa (2013). Net accumulation rates derived from ice core stable isotope records of Pío XI glacier, Southern Patagonia Icefield, *The Cryosphere*, **7**, 1635–1644, Doi: 10.5194/tc-7-1635-2013.

Shugar, D.H., A. Burr, U.K. Haritashya, J.S. Kargel, C. S. Watson, M.C. Kennedy, R.A.R. Bevington, R.A. Betts, S. Harrison and K. Strattman (2020). Rapid worldwide growth of glacial lakes since 1990. *Nature Climate Change*, **10**, 939–945. Doi: 10.1038/s41558-020-0855-4.

Slater, D.A., P.W. Nienow, D.N. Glodberg, T.R. Cowton and A.J. Sole (2017). A model for tidewater glacier undercutting by submarine melting, *Geophysical Research Letters*, **44**(5), 2360–2368, Doi: 10.1002/2016GL072374

Sommaruga, R., When glaciers and ice sheets melt: consequences for planktonic organisms (2015). *Journal of Plankton Research*, **37**(3), 509–518, Doi: 10.1093/plankt/fbv027.

Stuefer, M., Rott, H., & Skvarca, P., (2007). Glaciar Perito Moreno, Patagonia: Climate sensitivities and glacier characteristics preceding the 2003/04 and 2005/06 damming events. *Journal of Glaciology*, **53**(180), 3–16. Doi: 10.3189/172756507781833848.

Sugiyama, S., A. Bauder, M. Huss, P. Riesen, and M. Funk (2008). Triggering and drainage mechanisms of the 2004 glacier-dammed lake outburst in Gornergletscher, Switzerland. *Journal of Geophysical Research*, **113**, F04019, Doi: 10.1029/2007JF000920.

Sugiyama, S, D. Sakakibara, S. Tsutaki, M. Maruyama and T. Sawagaki (2015). Glacier dynamics near the calving front of Bowdoin Glacier, northwestern Greenland. *Journal of Glaciology*, **61**(226), 223–232, Doi: 10.3189/2015JoG14J127.

Sugiyama, S., M. Minowa, D. Sakakibara, P. Skvarca, T. Sawagaki, Y. Ohashi, N. Naito, and K. Chikita (2016). Thermal structure of proglacial lakes in Patagonia, *Journal of Geophysical Research: Earth Surface*, **121**, 2270–2286. Doi: 10.1002/2016JF004084.

Sugiyama, S., M. Minowa and M. Schaefer (2019). Underwater ice terrace observed at the front of Glaciar Grey, a freshwater calving glacier in Patagonia. *Geophysical Research Letters*, **46**. Doi: 10.1029/2018GL081441.

Sugiyama, S., M. Minowa, Y. Fukamachi, S. Hata, Y. Yamamoto, T. Sauter, C. Schneider, and M. Schaefer (2021). Subglacial discharge controls seasonal variations in the thermal structure of a glacial lake in Patagonia. *Nature Communications*, **12**, 6301, Doi:10.1038/s41467-021-26578-0.

Sutherland, D.A., R.H. Jackson, C. Kienholz, J.M. Amundson, W.P. Dryer, D. Duncan, E. F. Eidam, R.J. Motyka and J.D. Nash (2019). Direct observations of submarine melt and subsurface geometry at a tidewater glacier, *Science*, **365**, 6451, 369–374, Doi: 10.1126/science.aax3528.

Tetzner, D, E. Thomas and C. Allen (2019). A Validation of ERA5 Reanalysis Data in the Southern Antarctic Peninsula—Ellsworth Land Region, and Its Implications for Ice Core Studies, *Geosciences*, **9**(7), 289, Doi: 10.3390/geosciences9070289.

Thomas, R.H., W. Abdalati, E. Frederock, W.B. Lrabill, S. Manizade, and K. Steffen (2003). Investigation of surface melting and dynamic thinning of Jakobshavn Isbræ, Greenland, *Journal of Glaciology*, **49**(165), 231–239, Doi: 10.3189/172756503781830764

Tiberti, R., F. Buscaglia, C. Callieri, M. Rogora, G. Tatari, and R. Sommaruga (2020). Food Web Complexity of High Mountain Lakes is Largely Affected by Glacial Retreat, *Ecosystems*, **23**, 1093–1106, Doi: 10.1007/s10021-019-00457-8.

Truffer, M., R.J. Motyka, M. Hekkers, I.M. Howat and M.A. King (2009). Terminus dynamics at an advancing glacier: Taku Glacier, Alaska, *Journal of Glaciology*, **55**, 1052–1060, Doi: 10.3189/002214309790794887.

Truffer, M., and R. J. Motyka (2016). Where glaciers meet water: Subaqueous melt and its relevance to glaciers in various settings, *Reviews of Geophysics*, **54**, 220– 239. Doi: 10.1002/2015RG000494

Tsutaki, S., K. Fujita, T. Nuimura, A. Sakai, S. Sugiyama, J. Komori and P. Tshering (2019). Contrasting thinning patterns between lake- and land-terminating glaciers in the Bhutanese Himalaya. *The Cryosphere*, **13**, 2733–2750. Doi:10.5194/tc-13-2733-2019.

Vallot, D., J. Åström, T. Zwinger, R. Pettersson, A. Everett, D. I. Benn, A. Luckman, W. J.J. van Pelt, F. Nick and J. Kohler (2018). Effects of undercutting and sliding on calving: a global approach applied to Kronebreen, Svalbard, *The Cryosphere*, **12**, 609–625, Doi: 10.5194/tc-12-609-2018

van Dongen, E., G. Jouvet, A. Walter, J. Todd, T. Zwinger, I. Asaji, S. Sugiyama, F. Walter and M. Funk (2020). Tides modulate crevasse opening prior to a major calving

event at Bowdoin Glacier, Northwest Greenland, *Journal of Glaciology*, **66**(255), 113-123, Doi: 10.1017/jog.2019.89.

Veh, G., O. Korup and A. Walz (2020). Hazard from Himalayan glacier lake outburst floods. *Proceedings of Natinal Academy of Sciences of United Sates of America*, **117**(2), 907–912. Doi: 10.1073/pnas.1914898117.

Warren, C.R. and A. Rivera (1994). Non-linear climatic response of Calving Glaciers: A case study of Pio XI Glacier, Chilean Patagonia, *Revista Chilena de Historia Natural*, **67**, 385–394

Warren, C. R., A. Rivera and A. Post (1997), Greatest Holocene advance of Glaciar Pio XI, Chilean Patagonia: possible causes, *Annals of Glaciology*, **24**, 11–15, Doi: 10.3189/S026030550001185X.

Watson, C.S., J.S. Kargel, D.H. Shugar, U.K. Haritashya, E. Schiassi and R. Furfaro (2020). Mass Loss From Calving in Himalayan Proglacial Lakes. *Frontiers in Earth Science*, **7**:342. Doi: 10.3389/feart.2019.00342

Westby, M.J., N.F. Glasser, J. Brasington, N.J. Hambrey, D.J. Quincey and J.M. Reynolds (2014). Modelling outburst floods from moraine-dammed glacial lakes. *Earth-Science Review*, **134**, 137–159. Doi: 10.1016/j.earscirev.2014.03.009.

Willis M.J., A. K. Melkonian, M. E. Pritchard and A. Rivera (2012). Ice loss from the Southern Patagonian Ice Field, South America, between 2000 and 2012, *Geophysical Research Letters*, **39**, L17501, Doi: 10.1029/2012GL053136.

Wilson, R., D. Carrión and A. Rivera (2016). Detailed dynamic, geometric and supraglacial moraine data for Glaciar Pio XI, the only surge-type glacier of the Southern Patagonia Icefield, *Annals of Glaciology*, **57**, 119–130, Doi: 10.1017/aog.2016.32.

Wilson, R., N.F. Glasser, J.M. Reynolds, S. Harrison, P.I. Anacona, M. Schaefer and S. Shannon (2018) Glacial lakes of the Central and Patagonian Andes. *Global and Planetary Change*, **162**, 275–291. Doi:10.1016/j.gloplacha.2018.01.004,.

Wood, M., E. Rignot, I. Fenty, D. Menemenlis, R. Millan, M. Morlighem, J. Mouginot & H. Seroussi (2018). Ocean-Induced Melt Triggers Glacier Retreat in Northwest Greenland, *Geophysical Research Letters*, **45**(16), 8334–8342, Doi: 10.1029/2018GL078024

Wood, M., E. Rignot, I. Fenty, L. An, A. Bjørk, M. van den Broeke, C. Cai, E. Kane, D. Menemenlis, R. Millan, M. Morlighem, J. Mouginot, B. Noël, B. Scheuchl, I. Velicogna, ‚J.K. Willis and H. Zhang (2021), Ocean forcing drives glacier retreat in Greenland, *Science Advances*, **7**(1)., eaba7282, Doi: 10.1126/sciadv.aba7282.

Xu, N., H. Zheng, Y. Ma, J. Yang, X. Liu and X. Wang, (2021). Global Estimation and

Assessment of Monthly Lake/Reservoir Water Level Changes Using ICESat-2 ATL13 Products. *Remote Sensing*, **13**(14), 2744, Doi: 10.3390/rs13142744.

Yi, S., C. Song, Q. Wang, L. Wang, K. Heki, and W. Sun (2017). The potential of GRACE gravimetry to detect the heavy rainfall-induced impoundment of a small reservoir in the upper Yellow River. *Water Resource Research*, **53**, Doi:10.1002/2017WR020793.

Zemp, M., M. Huss, E. Thibert, N. Eckert, R. McNabb, J. Huber, M. Barandun, H. Machguth, S.U. Nussbaumer, I. Gärtner-Roer, L. Thomson, F. Paul, F. Maussion, S. Kuturov, and J.G. Cogley (2019). Global glacier mass changes and their contributions to sea-level rise from 1961 to 2016. *Nature*, **568**, 382–386, Doi: 10.1038/s41586-019-1071-0.

Zechmann J.M., M. Truffer, R.J. Motyka, J.M. Amundson and C.F. Larsen (2020). Sediment redistribution beneath the terminus of an advancing glacier, Taku Glacier (T'aakú Kwáan Sít'i), Alaska. *Journal of Glaciology*, **67**(262), 204–218. Doi: 10.1017/jog.2020.101.

Zhang, G., T. Yao, H. Xie, W. Wang and W. Yang (2015). An inventory of glacial lakes in the Third Pole region and their changes in response to global warming, *Global and Planetary Change*, **131**, 148–157, Doi:10.1016/j.gloplacha.2015.05.013.